FEDERAL UNIVERSITY OF SAO CARLOS
CENTER FOR EXACT SCIENCE AND TECHNOLOGY
GRADUATE PROGRAM IN MATERIALS SCIENCE AND ENGINEERING

TiNbCr MULTI-PRINCIPAL ELEMENT ALLOY DEGRADATION BEHAVIOR IN HARSH ENVIRONMENTS

Isabela Dainezi

São Carlos-SP
2024

FEDERAL UNIVERSITY OF SAO CARLOS
CENTER FOR EXACT SCIENCE AND TECHNOLOGY
GRADUATE PROGRAM IN MATERIALS SCIENCE AND ENGINEERING

TiNbCr MULTI-PRINCIPAL ELEMENT ALLOY DEGRADATION BEHAVIOR IN HARSH ENVIRONMENTS

Isabela Dainezi

Thesis presented to the Graduate Program in Materials Science and Engineering as a requirement to obtain the title of PhD IN MATERIALS SCIENCE AND ENGINEERING

Advisor: Dr. Carlos Alberto Della Rovere
Funding agency: CAPES-Process: 88887.500991/2020-00. CAPES PrInt-Process 88887.696560/2022-00.

São Carlos-SP
2024

DEDICATION

This thesis is dedicated to the countless young girls who dream of pursuing a career in science. May their aspirations be fueled by the resilience of the women who, despite facing subjugation, courageously continue to contribute to the world of science.

VITAE

Master in Materials Science and Engineering from the Federal University of Alfenas (2020).

Bachelor in Chemical Engineering from the Federal University of Alfenas (2019).

Interdisciplinary Bachelor in Science and Technology from the Federal University of Alfenas (2017).

UNIVERSIDADE FEDERAL DE SÃO CARLOS

Centro de Ciências Exatas e de Tecnologia
Programa de Pós-Graduação em Ciência e Engenharia de Materiais

Folha de Aprovação

Defesa de Tese de Doutorado da candidata Isabela Dainezi, realizada em 04/03/2024.

Comissão Julgadora:

Prof. Dr. Carlos Alberto Della Rovere (UFSCar)

Prof. Dr. Conrado Ramos Moreira Afonso (UFSCar)

Prof. Dr. Guilherme Zepon (UFSCar)

Prof. Dr. Artur Mariano de Sousa Malafaia (UFSJ)

Profa. Dra. Neide Aparecida Mariano (UNIFAL)

O Relatório de Defesa assinado pelos membros da Comissão Julgadora encontra-se arquivado junto ao Programa de Pós-Graduação em Ciência e Engenharia de Materiais.

ACKNOWLEDGEMENTS

I begin with heartfelt gratitude to God for gifting me with the patience, wisdom, and resilience necessary to complete this study. I also extend my thanks for the remarkable individuals placed in my journey, who played pivotal roles in bringing me to this point.

To my family—my parents, Marta and Pedro, and my brother Thiago—thank you for unwavering belief in my potential to undertake and complete this research. Your confidence, strength, and generous support, especially during my time abroad, made this journey possible. Additionally, I extend my gratitude to Ralph Henrique, Leonardo, and Agatha for brightening my days.

To my American family, my research group evolved beyond mere colleagues; they became my support system. Grace, Preston, Rafa, Matt, Haiming, and Dr. Gleeson, I am deeply grateful for your constant support, friendship, and every single day we spent together.

My Brazilian friends—Tainara, Bruna, Lucas, Gustavo, and Stella—your support has been invaluable from the initial thoughts of pursuing a PhD to the current stage of typing my thesis.

Special thanks to my dear friends Dr. Neide Mariano and her PhD student Spyridion for their unwavering support and knowledge-sharing.

I am sincerely grateful to Dr. Butler for generously sharing the HIPed alloy, knowledge, and his valuable time. I truly appreciate it.

This research was a collaborative effort, involving not only me and my research group but also Daniel Lamont, Esta Abelev, Susheng Tan, Brandon Blasko, Khaing Aye. Your support throughout this period is deeply appreciated.

To Dr. Malafaia and his students Bruno and Mirelly, I express my gratitude for your collaboration on the cyclic oxidation tests and discussions.

Working with Dr. Gleeson at the University of Pittsburgh has been a joy—from our discussions and conferences to workshops, seminars, and the various tests and analyses, including oxidation, sulfidation, SEM, EDS, XRD, and others, as well as the meticulous analysis of my results.

Lastly, I am thankful to my Brazilian advisor Dr. Rovere for supporting my research, Dr. da Silva and MSc. Cláudio Bezerra for their contributions to casting

the as-cast alloy, and the Federal University of São Carlos - UFSCar for providing me with this invaluable opportunity.

This study was financed in part by the Coordenação de Aperfeiçoamento de Pessoal de Nível Superior - Brasil (CAPES) - Finance Code 001.

Work by I. Dainezi was financially supported through CAPES/PrInt - Coordenação de Aperfeiçoamento de Pessoal de Nível Superior/Programa Institucional de Internacionalização process nº 88887.696560/2022-00 and CAPES - Coordenação de Aperfeiçoamento de Pessoal de Nível Superior process n° 88887.500991/2020-00.

ABSTRACT

The new properties exhibited by multi-principal element (MPE) alloys demonstrate promising results that have relevance across various applications, particularly in strategic industries. A challenging aspect in the field of materials for harsh service environments involves designing alloys that are resistant to oxidation and sulfidation at high temperatures, especially those composed of refractory elements. While oxygen is abundant in the atmosphere, sulfur stands out as one of the most common corrosive contaminants in high-temperature industrial settings, including fuel and feedstocks. The primary objective of this study was to develop and characterize the microstructure, as well as investigate the oxidation and sulfidation behavior of the TiNbCr MPE alloy in both as-cast and hot-isostatically pressed (HIPed) conditions in air, oxygen, and a reducing H_2S and H_2 gas mixture at temperatures between 600 and 1100°C, with exposures up to 100 hours. The oxidation and sulfidation behavior of the TiNbCr MPE alloy was compared with that of the commercial Haynes 188. The results indicate that the MPE alloy exhibits significantly superior sulfidation resistance compared to the Haynes 188, exhibiting a parabolic behavior with slow kinetics attributed to the formation of a NbS_2 inner layer facilitated by the addition of Cr. Notably, no formation of liquid products occurred, as observed in the case of Haynes 188. However, the oxidation behavior is linear, characterized by the formation of a non-protective scale, characterized as a stratified porous layer. Furthermore, in oxidation tests, it is observed a drop in the kinetics with an increasing at temperature-testing due to the formation of Cr_2O_3 layers.

Keywords: Multi-principal element alloy; refractory elements; TiNbCr; Niobium; Microstructure; oxidation; sulfidation.

RESUMO

COMPORTAMENTO DE DEGRADAÇÃO DA LIGA DE MÚLTIPLOS ELEMENTOS PRINCIPAIS TiNbCr EM AMBIENTE AGRESIVOS

As novas propriedades exibidas por ligas de múltiplos elementos principais (MEP) demonstram resultados promissores que têm relevância em diversas aplicações, especialmente em indústrias estratégicas. Um aspecto desafiador no campo de materiais para ambientes de serviço severo envolve o projeto de ligas que são resistentes à oxidação e sulfetação em altas temperaturas, especialmente aquelas compostas por elementos refratários. Enquanto o oxigênio é abundante na atmosfera, o enxofre destaca-se como um dos contaminantes corrosivos mais comuns em configurações industriais de alta temperatura, incluindo combustíveis e matérias-primas. O objetivo principal deste estudo foi desenvolver e caracterizar a microestrutura, além de investigar o comportamento de oxidação e sulfetação da liga MEP TiNbCr nas condições de bruta fusão e processada por prensagem isostática a quente (HIP) em ar, oxigênio e em uma mistura gasosa redutora de H_2S e H_2 em temperaturas entre 600 e 1100°C, com exposições de até 100 horas. O comportamento de oxidação e sulfetação da liga MEP TiNbCr foi comparado ao da liga comercial Haynes 188. Os resultados indicam que a liga MEP exibe resistência significativamente superior à sulfetação em comparação com a liga Haynes 188, apresentando um comportamento parabólico com cinética lenta atribuída à formação de uma camada interna de NbS_2 facilitada pela adição de Cr. Notavelmente, não ocorreu formação de produtos líquidos, como observado no caso da Haynes 188. No entanto, o comportamento de oxidação é linear, caracterizado pela formação de uma camada de óxido não protetora, estratificada e porosa. Contudo, em testes de oxidação, observa-se que um aumento da temperatura, a cinética de oxidação é reduzida devido à formação de camadas de Cr_2O_3.

Keywords: Liga de múltiplos elementos principais; Elementos refratários; TiNbCr; Nióbio; microestrutura; oxidação, sulfetação.

PUBLICATIONS

– **DAINEZI, I**.; GLEESON, B.; BUZATTI, B. R.; MALAFAIA, A. M. S.; DELLA ROVERE, C. A. TiNbCr Multi-Principal Element Alloy Oxidation Behavior in Air at 800-1000°C. HIGH TEMPERATURE CORROSION OF MATERIALS, 2024.

– **DAINEZI, I**.; GLEESON, B.; DELLA ROVERE, C. A. NbTiCr Multi-Principal Element Alloy Behavior in Harsh Environments. Presented in: 3 rd World Congress on High Entropy Alloys, 2023, Pittsburgh.

– **DAINEZI, I**.; GLEESON, B.; DELLA ROVERE, C. A. Sulfidation Behavior of NbTiCr Multicomponent Alloy. Presented in: Gordon Research Seminar on High Temperature Corrosion, 2023, New Hampshire.

– **DAINEZI, I**.; GLEESON, B.; DELLA ROVERE, C. A. Sulfidation Behavior of NbTiCr Multicomponent Alloy. Presented in: Gordon Research Conference on High Temperature Corrosion, 2023, New Hampshire.

– **DAINEZI, I**.; GLEESON, B.; DELLA ROVERE, C. A. Electrochemical Corrosion Behavior of a NbTiCr Multi-Principal Element Alloy. Presented in: EXTREME Workshop, 2023, Aachen.

– **DAINEZI, I**.; PASSOS, J. G. C.; DELLA ROVERE, C. A. Characterization of the Microstructure, Microhardness and Electrochemical Corrosion Behavior of a NbTiCr Multicomponent Alloy: A First Step Toward an Orthopedic-Implant Application. Presented in: Materials Science & Technology, 2022, Pittsburgh.

– **DAINEZI, I**.; SILVA, R.; DELLA ROVERE, C. A. Avaliação microestrutural da liga refratária multicomponente NbTiCr. Presented in: 24° Congresso Brasileiro de Engenharia e Ciência dos Materiais, 2022, Águas de Lindóia.

– **DAINEZI, I**.; SILVA, R.; DELLA ROVERE, C. A. Avaliação do comportamento a oxidação da liga refratária multicomponente NbTiCr. Presented in: 24° Congresso Brasileiro de Engenharia e Ciência dos Materiais, 2022, Águas de Lindóia.

x

SUMMARY

TABLES LIST

Page

FIGURES LIST

Pag.

SYMBOLS AND ABBREVIATIONS

A	Initial surface area
a	Constant
Al	Aluminum
a_m	Activity of metal
Ar	Argon
at.	Atomic
atm	Atmosphere
B	Boron
b	Constant
BCC	Body centered cubic phase
CBS	Circular Backscatter Detector
cm	Centimeters
cm^3	Cubic centimeter
Co	Cobalt
$CoNb_2S_4$	Cobalt and niobium sulfide spinel
CoS	Cobalt sulfide
Cr	Chromium
$Cr_{23}C_6$	Chromium carbide
Cr_2O_3	Chromium oxide (Chromia)
Cr_2S_3	Chromium sulfide
Cr_3Nb_3N	Chromium and niobium nitrite spinel
CTE	Coefficient thermal expansion
D	Diffusibility
DEMAEEL	Departamento de Engenharia de Materiais at Engineering school of Lorena
dL	Linear distance variation
dW/dt	Derivative of the mass gain per area in function of time derivative
EBSD	Electron Backscatter Diffraction
EDS	Energy-dispersive spectrometer
Fe	Iron

g	Grams
h	Hours
H_2	Hydrogen gas
H_2S	Hydrogen sulfide
HCP	Hexagonal compact phase
HEA	High entropy alloy
Hf	Hafnium
HIP	Hot-isostatically pressing
HRC	Rockwell C hardness
HV	Vickers microhardness
J	Flux
K	Kelvin
K	Reaction equilibrium constant
k	Rate constant
ke	Logarithmic rate constant
Kgf	kilogram-force
kJ	kilojoule
k_l	Linear rate constant
k_p	Parabolic rate constant
kPa	kilopascal
kV	kilo Volt
Kα	K-alpha spectral line
L0	Linear distance initial
La	Lanthanum
LCE	Laboratório de Caracterização Estrutural
Liq	Liquid phase
Ln	Logarithmic natural
Log	Logarithmic base 10
M	Mobility
m_1	Dry mass measurement
m_2	Wet mass measurement
m_3	Dry wet mass measurement

MEP	Múltiplos elementos principais
Mg	Magnesium
mg	Milligrams
MG	Minas Gerais
min	Minutes
mm	Millimeters
Mn	Manganese
MnO_2	Manganese oxide
Mo	Molybdenum
MoO_3	Molybdenum oxide
MoS_2	Molybdenum sulfide
MPa	Mega pascal
MPE	Multi-principal element
N	Nitrogen
n	Time exponent
n	Number of mols of O_2
N, O	Nitrites and oxides
Na_2CO_3	Sodium carbonate
Nb	Niobium
Nb_2O_3	Niobium oxide
$NbCrO_4$	Niobium and chromium oxide spinel
NbO	Niobium oxide
Nb_2O_5	Niobium oxide
NbS_2	Niobium sulfide
$NbTiO_4$	Niobium and titanium oxide spinel
NFCF	Nanoscale Fabrication and Characterization Facility
Ni	Nickel
Ni_3S_2	Nickel sulfide
O	Oxygen
O_2	Gas oxygen
P	Partial pressure of oxygen to avoid oxidation
PA	Pennsylvania

P_{H2}	Partial pressure of hydrogen
P_{H2S}	Partial pressure of hydrogen sulfide
Pitt	University of Pittsburgh
pm	Picometer
P_{O_2}	Partial pressure of oxygen
P_{S2}	Partial pressure of sulfur
Q	Activation energy
R	Ideal gas constant
R^2	Coefficient of determination
s	Second
S	Sulfur
SE	Secondary electron
SEM	Scanning electron microscope
Si	Silicon
SiC	Silicon carbide
SiO_2	Silicon oxide
SO_2	Sulfur dioxide
SO_3	Sulfur trioxide
SP	São Paulo
T	Temperature
T_1	Room temperature
T_2	Average of the temperature between the beginning, middle and the end of the reaction tube
t	Time
Ta	Tantalum
TGA	Thermogravimetry analyzer
Ti	Titanium
TiN	Titanium nitrite
$TiNb_2O_7$	Titanium and niobium oxide spinel
TiO_2	Titanium oxide (Titania)
TiS	Titanium sulfide
TiS_2	Titanium disulfide

TMA	Thermomechanical Analyzer
u. a	Unit arbitrary
UFSJ	Federal University of São João del-Rei
USP	University of São Paulo
V	Volume of the reaction tube
V	Vanadium
W	Tungsten
WS_2	Tungsten sulfide
wt.	Weight
x	Molar fraction
XRD	X-ray diffraction
Y	Yttrium
Z	Spatial coordinate
Zn	Zinc
Zr	Zirconium
%	Percentage
(Cr, Mn) O	Oxide rich in chromium and manganese
(Nb, Ti) O	Oxide rich in Nb and Ti
(Nb, Ti, Cr) O	Oxide rich in Nb, Ti and Cr
$\bar{V}_m$	Molar volume
ε_{CrNb}	Chemical parameter interaction between Cr and Nb
ρ_{water}	Density of water
$\frac{\partial C}{\partial x}$	Concentration gradient
ΔG	Gibbs energy
ΔW	Mass gain
°C	Celsius degree
µA	Microampere
µm	Micrometers
Å	Angstrom
ΔW	Mass gain
$\Delta G°$	Standard Gibbs energy
θ	Angle of incidence of the x-rays

v	Flow rate of the reaction gas
μ	Chemical potential
ρ	Density

1 INTRODUCTION

Conventional metallic alloy development involves choosing a solvent element and adding small amounts of solutes to enhance specific properties. This approach facilitates large-scale production, recycling, cost-effectiveness, and the combination of alloys. However, technological advancements have spurred the emergence of multi-principal element alloys (MPE) [1-3].

The development of MPE alloys opens new avenues for technological advancement, yet the multidimensional composition space remains largely unexplored. Recent studies indicate a higher number of publications addressing challenges and low performance in the oxidation behavior of MPE alloys compared to commercial alloys indicating no satisfactory performance. Errors in alloying element selection, such as Mo, V, Zr, and Hf, are highlighted, associated with negative effects like "pesting" and volatile oxide formation [4].

High-temperature degradation tests typically occur in oxidizing environments, but in industries like oil and certain space applications with reducing oxygen and sulfur-containing atmospheres, no studies have been conducted. These innovative alloys show potential for replacing superalloys in aerospace applications, with a focus on performance against oxidation and sulfidation at high temperatures.

The superalloy Haynes 188, exhibiting satisfactory behavior in sulfur-containing environments, stands out. However, its testing in sulfidizing conditions forms Ni and Co sulfides, presenting challenges due to eutectic reactions and molten sulfide formation, leading to potential catastrophic sulfidation attacks [5,6].

Considering that most studies on high-temperature degradation behavior are conducted isothermally in an oxidizing environment, a knowledge gap exists. This research aims to address this gap by conducting extensive oxidation studies, including isothermal tests with extended durations, anisothermal oxidation, cyclic oxidation tests, and studies in atmospheres containing sulfur.

In this context, this work is insert. Due to the remarkable potential of the combination of Ti, Nb and Cr, this work is aimed to produce TiNbCr MPE alloy and investigate its degradation behavior in harsh environments: oxidation, sulfidation & oxidation and sulfidations from 600-1100°C by different techniques

and evaluate it in terms of chemical composition, comparing to Haynes 188, and microstructure comparing TiNbCr MPE alloy in condition as-cast and HIPed.

2 LITERATURE REVIEW

2.1 Multi-Principal Element Alloy

Multi-principal element alloys are characterized by not having a system composed of solute and solvent, as conventional alloys, but rather of several elements with high levels, often in equimolar quantities [1, 7-12].

According to Coury et al. [13], this kind of alloy is derived from High Entropy Alloys (HEA) that has two concepts in its development. The first one, is based on the amount of each element which should be smaller than 35 at. % and the second is based on the configurational entropy that should be higher than 1.6R, R is constant of ideal gases [10].

Yeh et al. [14], reported that the main goal of HEA development was to obtain an alloy from concentrated mixture of elements forming a single-phase alloy and it would be possible by the high configurational entropy of the phase BCC or FCC in comparison to other “ordered” phase as in the phase γ’ in Ni superalloys, for example.

However, the development of 5-elements alloys has enabled the formation of microstructures with simpler phases, such as $L1_2$ and B2, which may exhibit lower entropy compared to high-entropy alloys (HEA) containing elements like Al and transition metals such as Fe, Cr, Co, and Ni [15]. Consequently, the initial concept applied in HEA has been discarded [16].

Even with disagreements about the initial development concepts, the number of researchers interested in to develop MPE alloys is increasing, as highlighted by Birbilis et al. [17]. Figure 2.1 shows an increasing number of publications of this kind of alloys and it is leaded by USA and China, due to the remarkable mechanical properties as reported also by Gludovatz et al. [18], Coury et al. [13] and Butler and Colleagues [19]. However, as observed by Birbilis et al. [17] and Gorr et al. [2] to achieve a satisfactory environmental degradation behavior is still a challenge for researchers that develop MPE alloys.

Senkov et al. [3] described that Al, Cr, Ti and Si addition trend to increase the oxidation resistance due to protective oxide scale formation and the V, Mo and W addition may decrease it due to the oxide volatilization. While Ti allows a

low-density alloy development, Cr addition may stabilize intermetallic phase, such as Laves phase in the alloy [20-23].

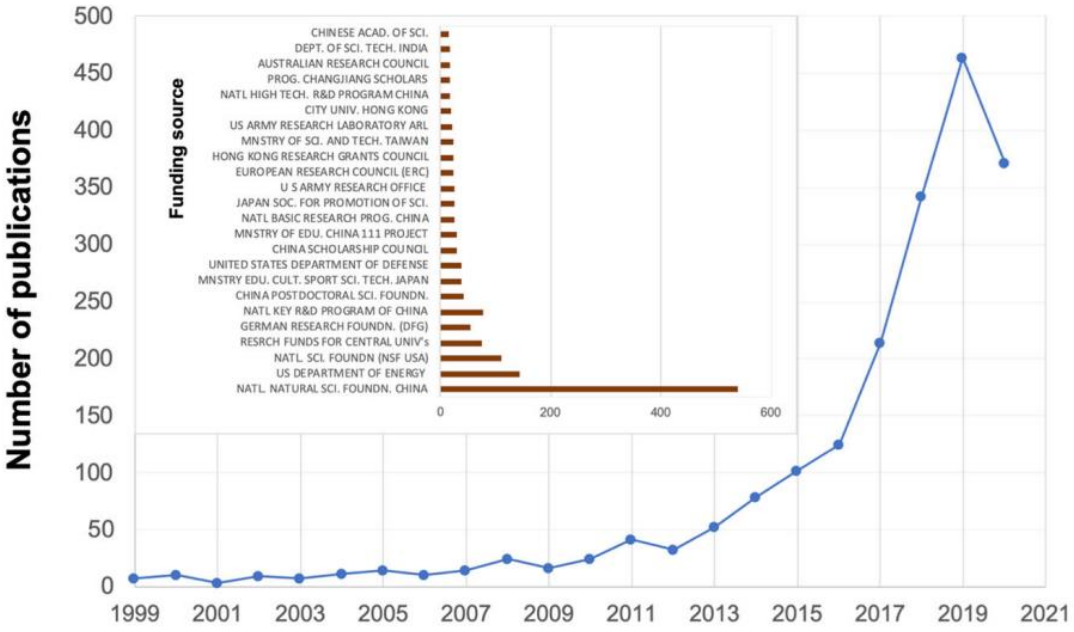

Figure 2.1 - Number of publications about HEA/MPE/CCA alloys for the period of 1999 to August 2020 [17].

Comparing the oxidation behavior of MPE alloys with refractory elements with refractory commercial alloys, Gorr et al. [2] highlighted that the complex oxides formation may reduce the oxidation kinetics, as noted for $NbCrO_4$, $NbTiO_4$ and $TiNb_2O_7$ compared to pure Nb oxides due to the reduction in kinetics formation and lower Gibbs energy [4, 24-26].

Evaluating AlCrMoTiNb and AlCrMoTiW MPE alloys, Gorr et al. [4] reported a moderated mass gain per area for both compositions (10mg/cm^2) and a parabolic behavior for the second composition at 1000 and 1100°C tested in air up to 48h. However, Cao et al. [26] highlighted that the Mo addition on TiNbTa0.5Zr, TiNbTa0.5ZrAl and TiNbTa0.5ZrAlMo0.5 may reduce the oxidation resistance due to the MoO_3 volatilization at high temperatures as reported by Cheng et al. [27] and Li et al. [28]. Similar to Mo studies, Geng et al. [29] and Cao et al. [26] suggested that V and W exhibits the same behavior due to the deleterious and volatile oxides formation.

The influence of Hf and Zr addition in oxidation behavior was investigated by Sheikh et al. [30] with the MPE alloy Hf0.5Nb0.5Ta0.5Ti1.5Zr from 600 to 1000°C in air up to 50h. The researchers observed that the alloy exhibited the pesting phenomena due to the non-formation of a protective oxide scale and the formation of an internal reaction zone. However, when they removed Hf and Zr, no pesting was observed because Hf and Zr forms a non-protective oxide external scale composed of a complex oxide mixture with a not compatible thermal expansion comparing to the alloy.

Young [31] describes pesting phenomena as an oxidation mechanism common in refractory elements and it is characterized by oxygen diffusion trough the grain boundaries at moderated temperatures, 600-800°C. Consequently, a fast intergranular oxidation is observed and also a fast disintegration of the metal substrate.

Additionally, a comparative between different systems of MPE alloys and element additions are shown in Figure 2.2 and Table 2.1, where it is possible to note that Al, Cr and Ta alloys exhibits smaller mass gain per areas in tests at 1000°C up to 20h in air, followed by alloys with Al and Cr and also Zr and V.

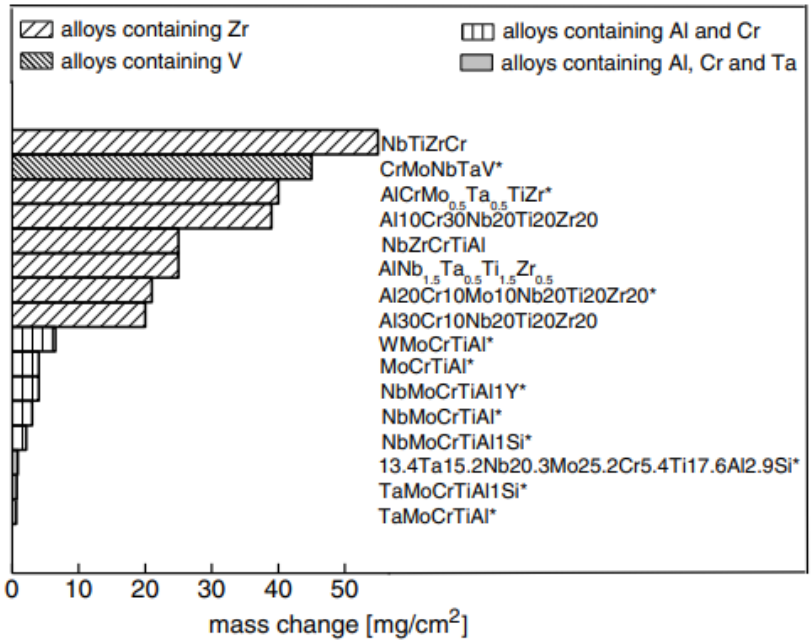

Figure 2.2 - Comparison between different MPE alloy systems in terms of oxidation behavior in air at 1000°C up to 20h [2].

Table 2.1 - Most Elements additions and their consequences in oxidation behavior. Adapted from Gorr et al. [2].

Element	Advantage	Disadvantage
Hf	-	Supports the pesting phenomena by increasing the oxides volume
Mo	-	Oxide volatilization above 795°C
Nb	-	Non-protective oxides formation
Ta	Increases the temperature to for the non-protective Nb_2O_5 and the protective $CrTaO_4$	-
V	-	Oxide volatilization above 678°C
W	-	Oxide volatilization above 1000°C
Zr	-	Oxides with fast growth rate and supports the pesting phenomena by increasing the oxides volume
Ti	Supports the formation of complex oxides with high solubility of different metal cations	-
Al	Forms a protective oxide Al_2O_3 and reduces the oxidation kinetics	-
Cr	Forms protective oxides as Cr_2O_3 and $CrTaO_4$ and may neutralize the presence of Nb_2O_5 by the $NbCrO_4$ formation	-
Si	Reduces the V oxidation, facilities the Al_2O_3 formation and reduces nitridation	-
Y	May improves scale adherence	-

Aimed to develop a MPE alloy with satisfactory behavior in harsh environments and in service at high temperature, for space and aerospace applications, Butler et al. [19] investigated the composition of MPE alloys based on Ta, Nb, Ti, Cr additions. They conducted studies with NbCr, TiNbCr and TaTiNbCr. The researchers characterized these alloys and reported that: (i) the NbCr alloy microstructure is composed of a Laves C15 matrix with BCC precipitates; (ii) the Ti addition to the NbCr alloy inverts the microstructure to a

BCC matrix rich in Nb and Ti with Laves phase precipitates rich in Cr; (iii) the Ta addition increases the BCC phase fraction and retain the Laves phase precipitation, as shown in the thermodynamics calculations in Figure 2.3 did with Pandat Nb2020 databases.

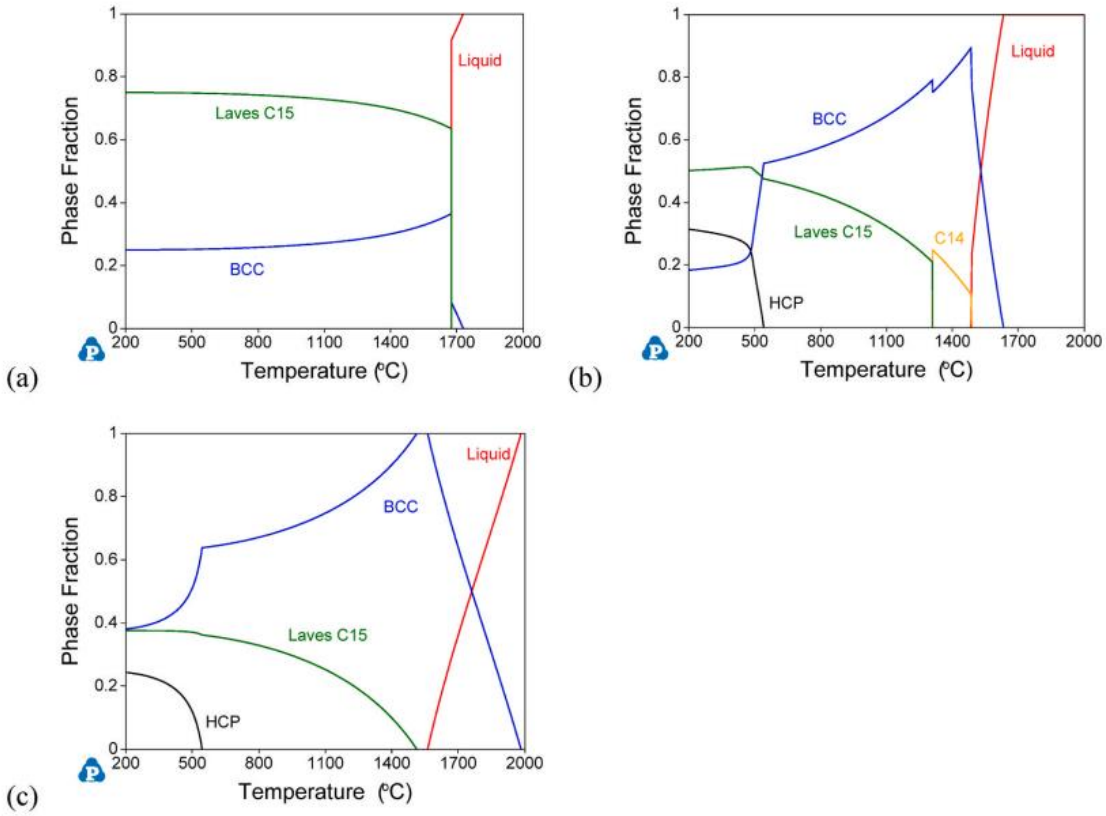

Figure 2.3 - Thermodynamics calculation obtained by Pandat Nb2020 databases for (a) NbCr alloy; (b) TiNbCr alloy and (c) TaTiNbCr alloy [19].

Focused on evaluating the mechanical behavior of NbCr, TiNbCr and TaTiNbCr alloys, Butler and colleagues [19] tested samples under compressive conditions at 25, 1000 and 1200°C. They reported that the binary alloy, NbCr, exhibited the highest value for mechanical resistance at all tested temperatures (1670MPa at 25°C, 1480MPa at 1000°C and 1074MPa at 1200°C), but it did not exhibit a ductile behavior at 25 and 1000°C. On the other hand, the TiNbCr MPE alloy exhibited a quietly decreasing in the resistance at 25°C (1659MPa at 25°C, 218MPa at 1000°C and 60MPa at 1200°C), however its behavior was more ductile. The alloy composed of TaTiNbCr exhibited the smallest values for

mechanical resistance (665MPa at 25°C, 84MPa at 1000°C and 37MPa at 1200°C) but the best ductile in all conditions.

Butler et al. [32] evaluated the oxidation behavior of the same MPE alloys in air at 1200°C up to 24h by isothermal tests. The researchers reported that the oxidation kinetics of NbCr and TiNbCr were similar and almost parabolic during all of testing time, as shown in Figure 2.4. However, the TaTiNbCr alloy exhibited the worst behavior characterized by a parabolic behavior up to 8h, followed by a linear behavior up to 24h, and according to the research group it happened due to the spallation and a complex oxide scale formation with repetitive and non-continuous layers, composed of high defects density as porous and cracks.

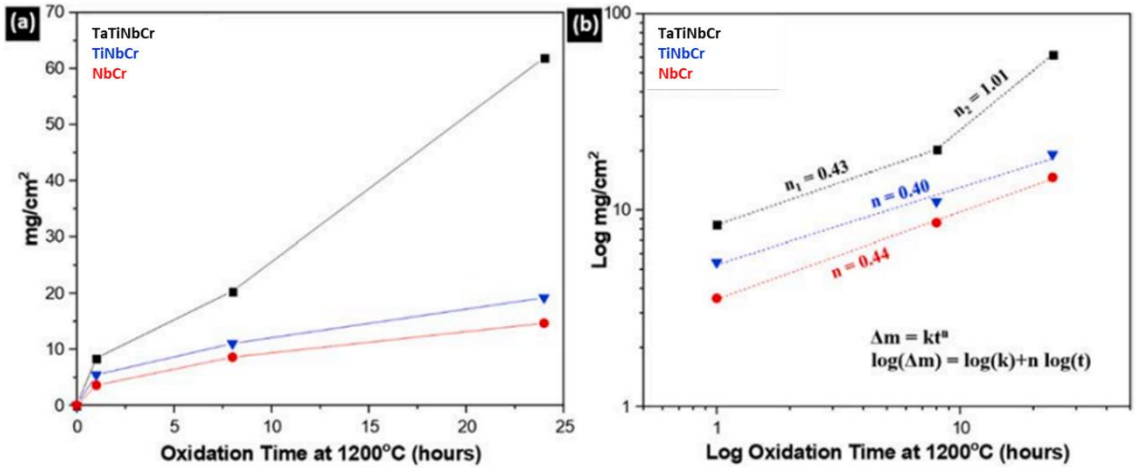

Figure 2.4 - (a) Mass gain per area in function of the oxidation time and (b) its math ajustment based on Wagner's law, for tests in air at 1200°C up to 24h. Adapted from Butler et al. [32].

In this study, the researchers also highlighted that more environment evaluations need to be done, with different temperatures, longer exposure time, early-stages investigation, as the oxidation mechanisms can be changed and they not clear yet, as highlighted by Welch et al. [33]. Recent studies as conducted by Gorr et al. [2], Butler et al. [32] and Welch et al. [33] also highlighted that testing in different environments such as with low partial pressure of oxygen, as sulfidizing, should be done to increase the possibilities of application of MPE alloys.

2.2 Environmental degradation behavior

The environmental degradation behavior plays a crucial role in the selection of materials for applications, such as energy, the chemical industry, oil and gas, and strategic fields. This is particularly true for those operating under special conditions of temperature, pressure, and varying compositions [31].

In this context, studies in harsh environments at different temperatures are conducted based on commercial processes. The degradation resistance of the alloy depends on its protective mechanism. In other words, the resistance to degradation relies on the formation of a protective scale that acts as a barrier to gas/contaminant diffusion [34].

This section aims to discuss oxidation due to the most commercial application works under oxygen presence and sulfidation due to the difference elements behavior in reduced oxygen environment.

2.2.1 Oxidation behavior

Among a lot of oxidation process parameters, Gemelli [35] and Young [31] highlight that the oxidation process is affected by the microstructure and chemical composition of the alloy.

In this context, Gesmundo and Gleeson [36] described the oxidation process in function of two-phase alloys comparing to single-phase alloys in terms of the stable scaling formation. The researchers reported that the slow-growing is more difficult in the case of two-phase alloys, so they needs higher concentration of the reactive element alloying.

Figure 2.5 shows the main oxidation behavior and scaling growth of two-phase alloys according to Gesmundo and Gleeson [36]. The first one, Figure 2.5 (a), is characterized by the two phases oxidizing independently and a nonuniform scale is formed, as reported by Smeggil [37] oxidizing an Eutectic Alloy Ni3AI-Ni3Nb in air at 1155°C, Figure 2.6 (a), and extending for sulfidation behavior, this type also was observed by Mallia and Young [38] studying duplex stainless steel SAF 2205 at 1058°C, 1148°C and 1238°C, Figure 2.6 (b).

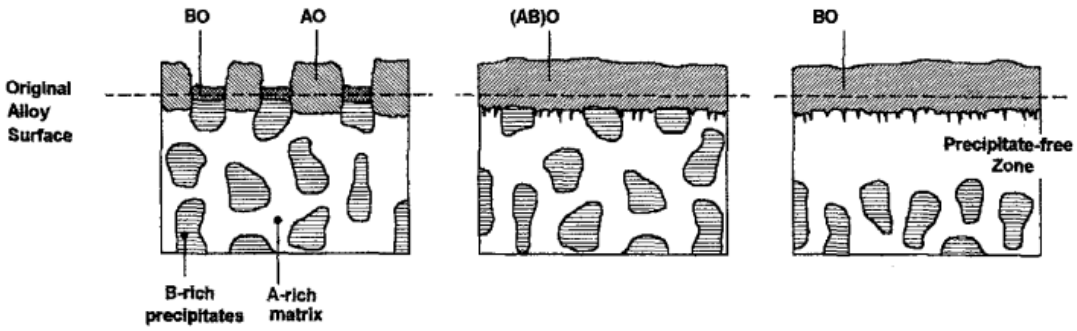

(a) (b) (c)

Figure 2.5 - Examples of the main oxidation behaviors for two-phase alloys. (a) The two phases oxidize independently; (b) The two phases oxidize cooperatively; and (c) The solute-rich second phase acts as a reservoir [36].

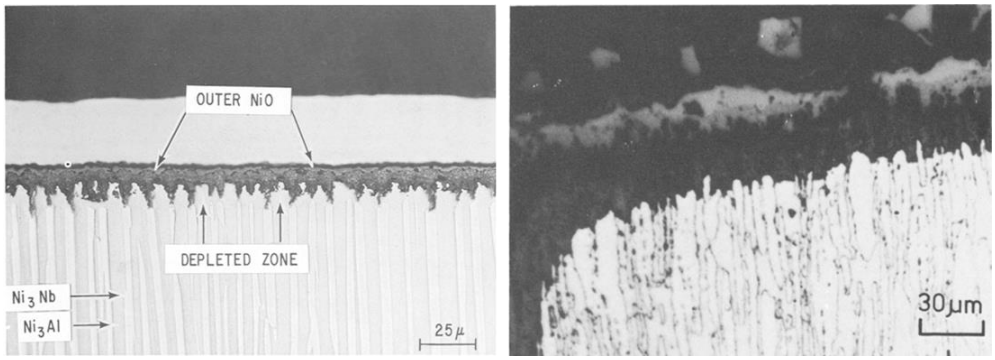

(a) (b)

Figure 2.6 - Example of two-phase alloys scaling-growth process. (a) Eutectic Alloy Ni3Al-Ni3Nb oxidized in air at 1155°C during 10min. (b) Duplex Stainless Steel SAF 2205 sulfidized at 1238°C K with a partial pressure of sulfur equal to $3x10^{-8}$ atm during 12h. Adapted from Smeggil [37] and Mallia and Young [38].

The second mechanism shown in Figure 2.5 (b) is characterized by a uniform scaling formation due to the two phases oxidize cooperatively [36]. This behavior was observed by Barrett and Lowell [39] oxidizing cyclically Ni-Cr-Al alloys at 1100 and 1200°C in air during 500 cycles of 1h each at 1100°C and 200 cycles of 1h each at 1200°C, Figure 2.7 (a), and by Carrasco et al. [40] with the same system, but tested isothermally at 750 and 850°C.

The third type highlighted by Figure 2.5 is characterized by the action of the solute-rich second phase. It acts as an effective solute reservoir for the scale

growth, consequently, an accumulation of solute-rich second-phase particles at the alloy-scale interface occurs due to the metal consumption. This behavior was reported by Espevik and colleagues [41] for Co-Cr-W alloys with 34-40 wt.% Cr and up to 10 wt.% W oxidized in air at 1000 and 1250°C up to 20h, Figure 2.7 (b), and Belen et al. [42] for 25Cr-35Ni cast steels with Al addition oxidized at 1000°C in pure dry oxygen up to 1224h.

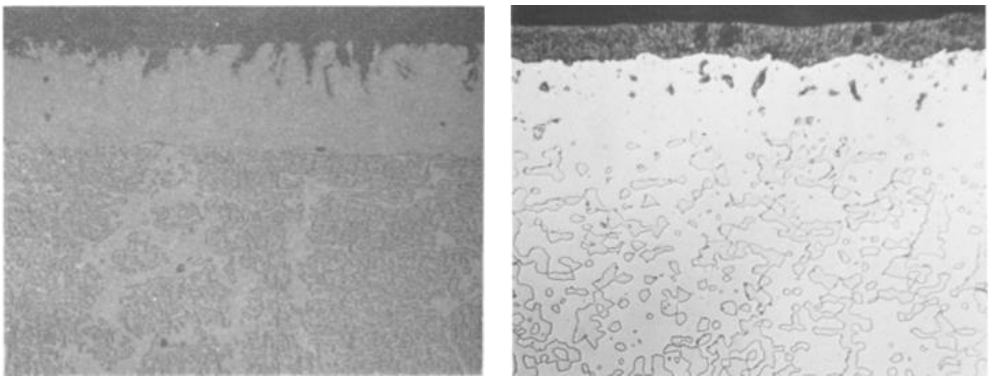

(a) (b)

Figure 2.7 - (a)Ni-9.73Cr17.18Al alloy after cyclic oxidation 500 1-hr cycles at 1100 with a magnification of 250 [39]; (b) Co-Cr-6W alloy oxidized in air at 1200°C during 8h with a magnification of 350 [41].

Additionally, Gesmundo and Gleeson [36] highlighted that two-phase ternary alloys exhibit more complex oxidation process compared to the two-phase binary alloys due to an extra degree of introduced in ternary alloys. As consequence, the diffusion of alloying elements back into the ternary alloy must be considered. This introduces the possibility of diffusion occurring through a two-phase structure, thereby altering the phase constitution of the alloy, potentially increasing the oxidation kinetics. It is important to note, however, that this effect may not be significant in cases where the diffusion rate of the components is exceptionally low.

As highlighted by Gorr et al. [2] for MPE alloys, the oxidation behavior is also determined by the chemical composition. Stringer [43] evaluated the oxidation of Nb crystals in air at from 560 to 925°C up to 300 min and reported

linear kinetics behavior for all conditions. However, different oxidation mechanisms and oxides morphology are reported, as shown in Figure 2.8.

At temperatures lower than 600°C, the process is characterized by the formation Nb_2O_5 and NbO. While the Nb_2O_5 grew as a dense layer, the NbO grew as platelets parallel to the {100} planes in the metal, which produced pores in the Nb_2O_5 layer which act as crack nucleators. With it, the process was considered as anisotropy oxidation because of the formation of NbO structure.

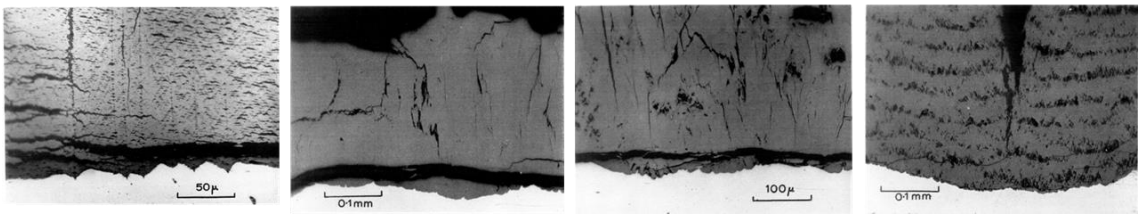

(a) (b) (c) (d)

Figure 2.8 - Cross-section of Nb crystals oxidized in air (a) at 560°C during 260min; (b) at 750°C during 300min; (c) at 825°C during 95min; and (d) at 925°C during 73min. Adapted from Stringer [43].

However, increasing the temperature, the NbO platelets formation disappeared and the anisotropy consequently and a cyclic oxidation mechanism is suggested based on the vacancy supersaturation development. During growth of compact oxide scale rich in Nb_2O_5, a vacancy supersaturation was developed in the vicinity of the oxide/metal interface due to difficulties in transferring metal atoms or oxygen atoms across the interface. When the supersaturation reached a critical value, the vacancies started to precipitate as voids, until the supersaturation had been removed. Growth of compact oxide then recommences, and the cycle repeats, consequently a stratified porous layer morphology is generated [43].

Jiang and colleagues [44] evaluated the influence of Nb addition on Ti-(0-50 at.%) Al alloys' oxidation behavior in air at 1446°C up to 24h. They reported that the kinetics was parabolic up to 20 at.% of Nb addition, when it started to be linear. According to the researchers, up to 15 at.% Nb addition, the Nb exists as a solid solution with TiO_2 and when this component content increases, complex

oxides start to be formed as $TiNb_2O_7$ and, consequently, the kinetics is faster, a linear behavior is described and a stratified porous layer formation is observed, as Stringer [43] for Nb crystals oxidation.

Kofstad et al. [45] investigated the Ti oxidation mechanism from 300 to 1000°C in air up to 5h. The researchers observed that: (i) Ti exhibited a logarithmic behavior up to 300 min testing at 300°C and followed by a cubic behavior. This fact suggested that the oxide scale was dominated by the formation of thin layers parallel to the surface; (ii) a cubic behavior from 300 to 600°C attributed to the oxygen diffusion into the Ti specie; (iii) a parabolic at temperatures higher than 850°C associated to the oxygen diffusion trough the TiO_2 scale, followed by a linear kinetics due to the cracks into the TiO_2 scale because of stresses in the oxide and phase boundary.

Due to its remarkable low density, Ti and Ti-alloys are largely studied by strategic industry. Dai et al. [46] reported that Ti-6Al-4V alloys has the maximum application at 350°C due to the poor high temperature oxidation resistance. At high temperatures, oxygen ingress in the alloy, first, the oxide scale thickness increases with oxygen internal diffusion and, consequently, it generates a decrease in bonding strength between the oxidation film and the alloy leads to a spallation process. Following this, ordered phases and fragile layers begin to form on the alloy surface, resulting in lattice distortion and a reduction in the mechanical properties of the alloy.

Dorcheh and colleagues [47] highlight the extensive interest about Cr addition in alloys applied in oxidizing environments due to its remarkable oxidation resistance, they also reported how extensive is the study about the pure Cr oxidation behavior characterization and Cr-alloys.

The oxidation of Cr or Cr-alloys is characterized by a dense and protective Cr-oxide scale, generally composed of Cr_2O_3, which acts as a barrier between the oxidizing environment and the metal. Consequently, the kinetics is described by a parabolic behavior [48].

Buscail et al. [49], studied Cr oxidation at 800, 900 and 1000°C and highlighted that the oxidation behavior of Cr is different according to the temperature. In all tested temperature not only, a parabolic behavior was

described but also a diffusion-controlled growth mechanism. Mitchell and colleagues [50] reported at 700°C, the growth of the Cr_2O_3 scale is primarily driven by outward chromium diffusion. Caplan and Sprouli [51], through calculations based on the diffusion coefficient of chromium in Cr_2O_3 at 950°C, indicated that the oxide on chromium primarily grows through grain-boundary transport of cations. Additionally, at temperatures exceeding 1000°C, the volatilization of Cr_2O_3 is reported, leading to a subsequent decrease in oxidation resistance [52].

However, Butler et al. [32] compare the oxidation behavior of NbCr and TiNbCr MPE alloys in air at 1200°C up to 24h. Analyzing the oxidized samples cross-sections, Figure 2.9, the researchers noted lower porosity density in the Cr_2O_3 scale formed in the ternary alloy. This fact suggests that the TiO_2 outer layer act as a barrier for Cr_2O_3 volatilization, consequently, the Cr_2O_3 layer is retained during more time.

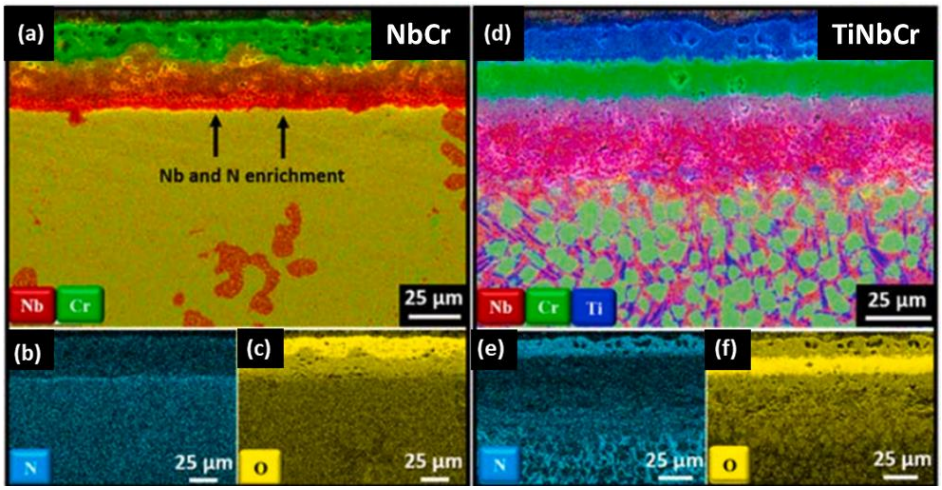

Figure 2.9 - EDS Mapping of (a)-(c) NbCr alloy and (d)-(f) TiNbCr alloy, oxidized at 1200°C in air during 8h. Adapted from Butler et al. [32].

Chyrkin [53] studied the oxidation behavior of Cr-forming Nickel-Base Alloy 625, which is part of Ni-Cr-Mo-Nb system and reported the chemical interaction between Nb and Cr. Samples tested in air at 900-1000°C up to 1000h exhibited Nb concentration, underneath the Cr_2O_3 scale, doubled compared to the Nb initial concentration in the alloy, highlighting the Nb diffusion from the bulk alloy, similar

results were obtained by Malafaia et al. [54] and Nope et al. [55]. Additionally, the precipitation on Nb-rich phase (δ) in vicinity of the interface between the oxide scale and the alloy surface require Nb diffusion from a region of low towards a region of high concentration, in other words, a Nb flux against the concentration gradient in called as uphill diffusion.

The uphill diffusion can be explained by the diffusion theory, as shown in Equation 1, where the flux of k species is J_k and it is a function of the chemical potential gradient. M_k is the mobility of k species, $\bar{V}_m$ is the molar volume, x_k is the molar fraction of k, μ_k the chemical potential of k and Z is a spatial coordinate that in this case it corresponds to the distance from the oxide scale and the alloy interface [56].

Equation 1

$$J_k = -\frac{1}{\bar{V}_m} M_k x_k \frac{\partial \mu_k}{\partial Z}$$

Analyzing the Equation 1 it is noted that if μ_{Nb} increases along the Cr depletion profile from the interface between the oxide scale and the alloy in direction of the bulk alloy, the J_{Nb} is negative and the Nb diffusion will be in a opposite direction of the activity gradient, towards the interface between oxide scale and alloy. Therefore, decreasing the μ_{Nb} with the increasing of Cr concentration, Nb diffuses toward the most Cr-depleted area, which is the interface between oxide scale and the alloy [53, 56].

The interaction between Nb and Cr that results in the Nb uphill diffusion can be explained by the Ficks' law [31], Equation 2, where the flux J is a function of the diffusivity and the gradient of the concentration C in the spatial coordinate x.

Equation 2

$$J = -D \frac{\partial C}{\partial x}$$

Applying the Equation 2 to the Nb and Cr diffusivity, the Equation 3 is resulted, where the Nb flux J_{Nb} is a function of the Nb diffusivity in Nb (D_{NbNb}) and in Cr

(D_{NbCr}) and a function of the Nb concentration gradient ($\frac{\partial C_{Nb}}{\partial x}$) and Cr concentration gradient ($\frac{\partial C_{Cr}}{\partial x}$) along the spatial coordinate x.

Equation 3

$$J_{Nb} = -D_{NbNb}\frac{\partial C_{Nb}}{\partial x} - D_{NbCr}\frac{\partial C_{Cr}}{\partial x}$$

The Nb flux is a positive factor and based on results reported for example by Chyrkin [53], Malafaia et al. [54] and Nope et al. [55], due to the Cr oxidation forming the external scale and the Cr-depletion zone generated in the underneath the interface between the oxide scale and bulk alloy, the Cr concentration gradient multiplied by the diffusivity of Nb in Cr should be positive and, consequently, the term of the gradient of Nb concentration multiplied by the diffusivity of Nb in Nb should be negative, Equation 4, and it is only possible if the chemical parameter interaction between Cr and Nb would be positive (ε_{CrNb}), characterizing a positivity chemical interaction that results in a uphill diffusion of Nb.

Equation 4

$$+\upsilon_e = -(-\upsilon_e) + \upsilon_e$$

$$\varepsilon_{CrNb} > 0$$

2.2.2 Sulfidation behavior

Oil industry has sulfur like the most contaminant with a fraction varying from 1% to 5%, it depends on step of the industry and the area that the oil is extracted. Also, in case of combustion with excess of air of fuel for generating heat in some process, sulfur reacts with oxygen, and it generates SO_2 and SO_3. But some cases, as coal gasification to substitute natural gas or medium- or low-BTU fuel gases, the combustion is taking place under stoichiometric or sub stoichiometric conditions to convert feedstock to process gases like H_2 and hydrocarbons. In this case, sulfur reacts and forms H_2S resulting in a reducing environment with a low oxygen potential [57-60].

In reducing environment, the corrosion reaction is characterized by a competition between oxidation and sulfidation. So, reducing the partial pressure of oxygen, the oxygen activity will be reduced as well and with it, the sulfidation is favored. On the other hand, increasing the partial pressure of oxygen, the oxidation reactions are increased. So, the sulfidation reaction is controlled by partial pressure of both gases, sulfur and oxygen [60, 61].

Generally, sulfides have negative Gibbs energy and the difference between sulfur atomic radius and metal ions is greater than between oxygen and metal ions, therefore, they have lower lattice energies. Consequently, the Gibbs energy of formation of sulfur compounds will be lower than that of oxygen and they will have lower melting temperature. Therefore, liquid products can be formed as well eutectic reaction can occur and both tend to rapidly consume the metal and increase the sulfidation attack [6, 57, 62].

In the examination of the lattice energy disparity between oxides and sulfides, the energy shift when one mole of a crystalline ionic compound is created from its individual ions, initially presumed to be in a gaseous state, serves as an indicator of the adhesive forces that unite ionic solids, with sulfides exhibiting reduced values in comparison [53, 57-64].

The lower lattice energies in sulfides make the point defect creation easier, consequently the higher diffusion rate and growth rate is reported for sulfides than for oxides. But, on the other hand, it generates deviations from stoichiometry that can occur more in sulfides than oxides and the sulfidation products can be less protective than its corresponding oxide, as chromium for example [57, 61-65].

Sulfides scales on common metals grow by the outward diffusion of cations and they lose their full contact with the alloy surface and the gas ingression into the alloy starts to occur, resulting in the formation of a porous inner layer and the gradual deterioration of scale compactness [57].

However, some exceptions are highlighted by Strafford and Datta [66] and Gleeson [59], refractory metals like Nb, Mo, Ta and W undergo a scaling process through the inward diffusion of anions, forming an inner layer with a low density of defects. Consequently, their sulfidation kinetics is lower than their

corresponding oxidation resistance, as shown in Figure 2.10. In other words, the sulfidation resistance of refractory metals is superior to their oxidation resistance.

Among refractory metals, Nb has the lowest sulfidation rate, which is comparable to the oxidation of Cr for analogous conditions, as shown in Figure 2.10. Chen and colleagues [62] studied the influence of Nb addition on Ni sulfidation behavior from 10 to 40 wt.% of Nb and they observed a decreasing in sulfidation rates with increasing niobium concentration until 34 wt.%, because in 40 wt.% a non-continuous NbS_2 layer was formed. They also noted that the location of Nb was the same that before sulfidation tests, so no outward diffusion, suggesting that NbS_2 grows by inward diffusion of sulfur, as observed by the Pt marking that indicated that the layer grows by outward diffusion of Ni.

Similar results were obtained by Gleeson and colleagues [67] when they studied the influence of 10-30 wt.% Nb addition on Co in sulfidation behavior at 600-700°C. The investigated compositions were Co-10Nb, Co-20Nb, Co-25Nb and Co-30Nb that exhibited a two-phase microstructure composed of a solid solution α-Co and intermetallic precipitates of $NbCo_3$. The researchers observed, with short-time sulfidation tests, that the solid solution sulfidized first and formed nodules of CoS. On the other hand, the $NbCo_3$ phase formed a thin protective layer rich in NbS_2. While the nodules grew laterally and coalesced inside of the external scale, the NbS_2 reacted with the CoS to form $CoNb_2S_4$ in a completely or partially way.

As mentioned before and observed in the Figure 2.10, refractory metals exhibit sulfidation rate slower than oxidation [59, 66]. However, comparing the sulfidation behavior of Co-Mo alloys with up to 40 wt.% Mo with the pure Mo sulfidation behavior, Gleeson et al. [58] reported faster kinetics and a semi-protective MoS_2 formation in the alloy than the pure Mo instead of protective as in the pure Mo.

According to the researchers, this fact could be explained by the structure and chemical properties of MoS_2 [58]. This sulfide has a hexagonal crystal structure described by the stacking sequence …SMoS SMoS SMoS… and it is characterized by having strong, covalently bonded S-Mo-S molecular sandwiches welded together by weak Van der Waals forces. Consequently, 3d

metals such as Co, Fe and Ni can intercalated into the Van der Waals gap, as represented by Figure 2.11, where also highlights the charge transfer that happens in this process.

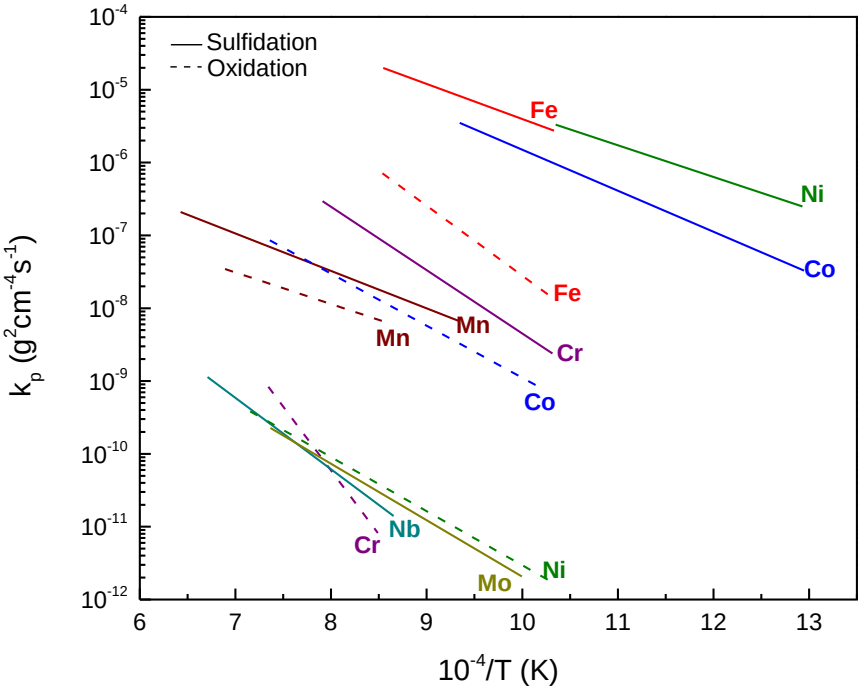

Figure 2.10 - Comparison of parabolic kinetics rate between oxidation and sulfidation. Data from Mrowec [57].

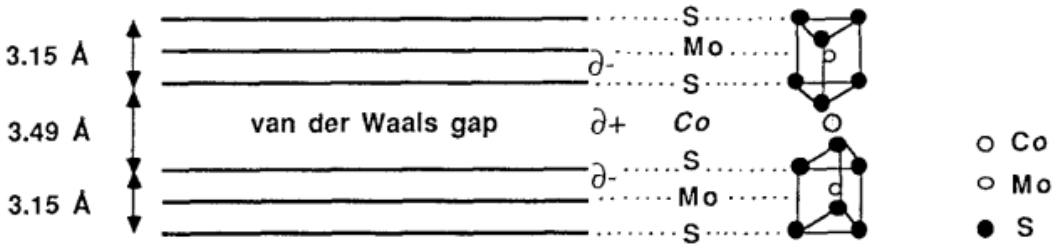

Figure 2.11 - Schematic of the sandwich structure of MoS_2 showing the Van der Waals gap between the loosely bound S-Mo-S [58].

Additionally, the Co^{+2} cations (radius ~0.72Å) intercalation occurs in octahedral holes in the Van der Waals gap, which the radius is ~0.74Å, so the Co^{+2} cations can fit with a minimum of distortion. Consequently, this layer did not

act as a barrier to the outward Co diffusion due to provide a short-circuit diffusion path for the Co^{+2} cations [58].

The influence of Cr addition on the sulfidation behavior of Co-base alloys was reported by Whittle et al. [68] with 1 up 25 wt.% of Cr at 800 and 1000°C in H_2S/H_2 atmosphere with a partial pressure of sulfur equals to 0.02atm. The researchers highlighted a parabolic behavior for all alloys and comparing to pure Co sulfidation, they observed that the rate increased with the Cr concentration up to 10 wt.% at 1000°C and up to 5 wt.% at 800°C. However, after it, they noted that the rate decreased progressively with an increasing in the Cr concentration due to the formation of Cr-rich sulfide.

Studying Co-Cr alloys with 1atm of sulfur vapor at 550 up to 900°C, Biegum et al. [69] reported that the inner layer rich in Cr sulfide suggests being composed of a solid solution of CoS in Cr_2S_3.

Mrowec [6, 65] investigated the effect of adding Cr to Fe-Cr, Co-Cr and Ni-Cr alloys, as shown in Figure 2.12, where is highlighted that alloys with a high Cr content present similar behavior and low additions of Cr, close to 2 at.%, do not play an important role in the behavior and the layers of products formed are single-phase.

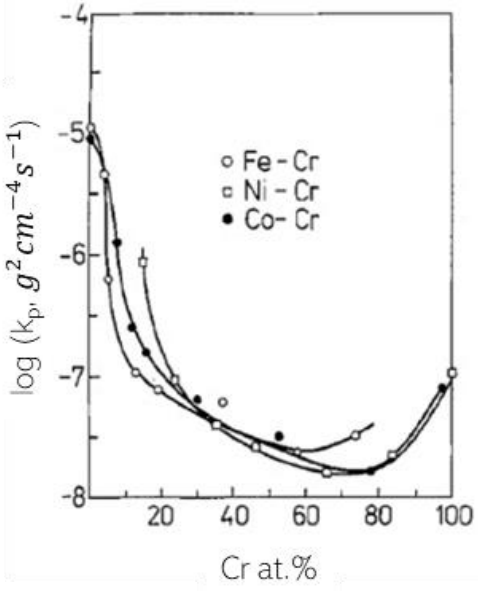

Figure 2.12 - Dependance of sulfidation kinetics with the Cr concentration at 900°C with sulfur pressure equals to 1atm. Adapted from Mrowec [65].

However, increasing the content to approximately 20 at.%, the sulfidation kinetics are reduced due to internal reactions generating a layer of $Fe(Fe_2-xCr_x)S_4$ for the Fe-Cr alloys, chromium sulfide with nickel and cobalt for the other alloys. Therefore, by increasing the Cr content, the product layer generated would be homogeneous in chromium sulfide doped with the base metal and the sulfidation kinetics will be lower than that of pure chromium. Nevertheless, when the Cr in the base metal is highly diffused and reacted, the base metal will suffer greater attack [65].

Additionally, Davin et al. [70]. investigated the influence of Al, Ta, Mo, Nb, W or Y addition in the Co-Cr alloys their sulfidation behavior. They observed that these additions had a greater affinity for S than Cr formed inner sulfide layer. However, Al was the only addition to improve the resistance and they attributed this observation to the small amount of the added elements, as Nb addition was only 3 wt.%.

Gleeson et al. [71] analyzed the influence of the addition of Al, Cr, Mn or Ti in the sulfidation behavior of Co-Mo alloys, in an atomic proportion of 55Co, 20Mo and 25 of the third element, at 600 or 700°C to 900°C in a partial pressure of sulfur equals to 10^{-2} atm. The researchers reported a complex, multilayered scales formation and, generally, composed of an outer layer rich in Co-sulfide, an intermediate layer that contained primarily the ternary element sulfide, and an inner layer which was no homogeneous in phases.

They concluded that Al and Cr additions improved the sulfidation resistance of the Co-Mo alloy, however, Mn addition decreases the resistance. The Ti addition promoted the formation of sulfides, however, due to the high oxygen solubility, Ti oxides were also formed even in a reduced partial pressure of oxygen, so it was impossible to compare the sulfidation kinetics with the other elements addition. The difficulty to isolate the sulfidation process in the Ti is also highlighted by Gorr et al. [2].

Raikar et al. [72] reported the sulfidation behavior of Ti and Ti-6Al-4V alloy up to 950°C during 4h. The researchers analyzed all data and evaluated the behavior based on the metal consumption instead of mass gain per area, due to

the spallation that some condition exhibited. They highlighted a parabolic behavior suggesting that the TiS_2 rich layer was protective.

Mrowec [57] highlights that in sulfidation & oxidation environments, Ti addition trends to form TiO_2 due to the high oxygen solubility and fast kinetics. However, this oxide increases the diffusion of sulfur through the external scale, characterizing no protection against sulfidizing & oxidizing environments.

The superalloy Co-Ni-based Haynes 188 is highlighted in the literature as having a satisfactory behavior in environments containing sulfur, with slower kinetics than other superalloys as Hastelloy X, Incone1671, Incoloy 800, for example [5, 73, 74].

However, Haynes 188 tested in sulfidizing environments forms Ni and Co sulfides which represents a disadvantage in its application, due to the eutectic reaction of $Ni+Ni_3S_2$ at 645°C and the melting point of Ni_3S_2 at 788°C, and a eutectic reaction of Co+CoS at 880°C [5]. As consequence, molten sulfides are formed and it increases the sulfide attack and can cause catastrophic sulfidation attack because they destroy the dense scale so easily [6, 73].

During their studies, Douglass and colleagues [73] noted that the Haynes 188 was the only superalloy that exhibits a quite linear/almost parabolic behavior in sulfidation environments, compared to 310 stainless steel, Hastelloy X, Incone1671, Incoloy 800 and FeCrAlY (GEl541 and MA956) tested at 1600 and 1800°F (~871 and ~982°C, respectively) with 2.7 and 0.8% sulfur.

The researchers reported that the sulfidation process resulted in a thick sulfide scale formation in all of alloys tested and an extensive internal sulfidation zone that suggested that it dominated the process [73].

2.3 High temperatures behavior analysis: kinetics and Thermodynamics

2.3.1 Kinetics

Oxidation and sulfidation processes are, in general, similar, because metal sulfides have the same type of cation defect as metal oxides. Therefore, Wagner's theory can be equally applied to both processes [58].

Generally, oxidation and sulfidation kinetics can be described by linear, logarithmic, or parabolic behavior. In linear kinetics, the layer of reaction product

formed on the surface is porous, presents some discontinuities, spallation, or it is not adherent. Consequently, the gas continues diffusing through the scale and will always be in contact with the metal surface where it is dissociated and ingresses to the alloy, and an internal reaction zone is formed. Therefore, the growth of the layer is controlled by the fast interfacial reactions, and it is independent of its thickness and can be expressed by Equation 5, where ΔW is the mass gain, A is the superficial area initial, k_l is the constant of linear kinetics and t is the time.

Equation 5

$$\left(\frac{\Delta W}{A}\right) = k_l t$$

The logarithmic oxidation/sulfidation kinetics occur in metals that have practically constant thickness over time. The metals oxidize/sulfidize more quickly at the beginning of the process, and after it, the process is almost constant [75]. Furthermore, layers grow according to the logarithmic law described by Equation 6, where ke is the constant of logarithmic kinetics and a and b are constants [61].

Equation 6

$$\left(\frac{\Delta W}{A}\right) = k_e \log(at + b)$$

The parabolic kinetics behavior has the diffusion as the limiting step t because it is the slowest process which the reaction rate decreases over time. After the initial formation of the oxide/sulfide, two sequential steps occur, the first of which can be described by the reactions at the metal/reaction product layer and reaction product/gas layer interfaces, and they control the reaction rate. The second stage is due to the transport of material in the form of ions and electrons through the formed layer [61]. The parabolic behavior is characterized by a protective scale formation which does not allow the gas keep contact with the surface of the metal [61]. The process can be described by Equation 7, where k_p is reaction rate constants of parabolic kinetics.

Equation 7

$$\left(\frac{\Delta W}{A}\right)^2 = k_p t$$

Additionally, the parabolic constant depends on the bond energy of the cations in the formed compound and its structure, in addition to the temperature and partial pressure of oxygen/sulfur in some cases [61]. Therefore, considering a constant pressure, the parabolic constant will vary according to Arrhenius' law, as shown in Equation 8, in which Q is the activation energy, R is the ideal gas constant and T is the temperature.

Equation 8

$$k_p = k_0 exp\left(\frac{-Q}{RT}\right)$$

Often, in oxidation and sulfidation processes at high temperatures, the kinetics are linear or parabolic, however, it depends on the crystalline structure and composition of the layers formed. Furthermore, it is worth highlighting that both processes affect the useful life of the material, as they affect its integrity, and the component may fail catastrophically [31].

Frequently, in the case of MPE alloys, to analyze the kinetics of the process in terms of behavior and to calculate the rate, is done by the linearization of Wagner's law, as shown in Equation 9 and Figure 2.13.

With the fitting highlighted by Equation 9, it is possible to calculate, with the slope, the time exponent n and according to Welch et al. [33] if its value is equals to 1, the kinetics are categorized as linear, primarily influenced by metal-oxide interface reactions. When n equals 0.5, the material exhibits parabolic kinetics, signifying a diffusion-controlled rate involving either the outward diffusion of cations, the inward diffusion of anions, or a combination of both processes. Exponents between 1 and 0.5 suggest mixed-mode behavior, incorporating both diffusion- and interface-controlled mechanisms. Kinetics displaying sub-parabolic behavior below 0.5 indicate diffusion-controlled reactions in conjunction with volatilization effects, such as cubic kinetics where n equals 0.3. Additionally, the oxidation data can be analyzed by a log fitting as shown in Figure 2.4.

Equation 9

$$\ln\left(\frac{\Delta W}{A}\right) = \ln k + n \ln t$$

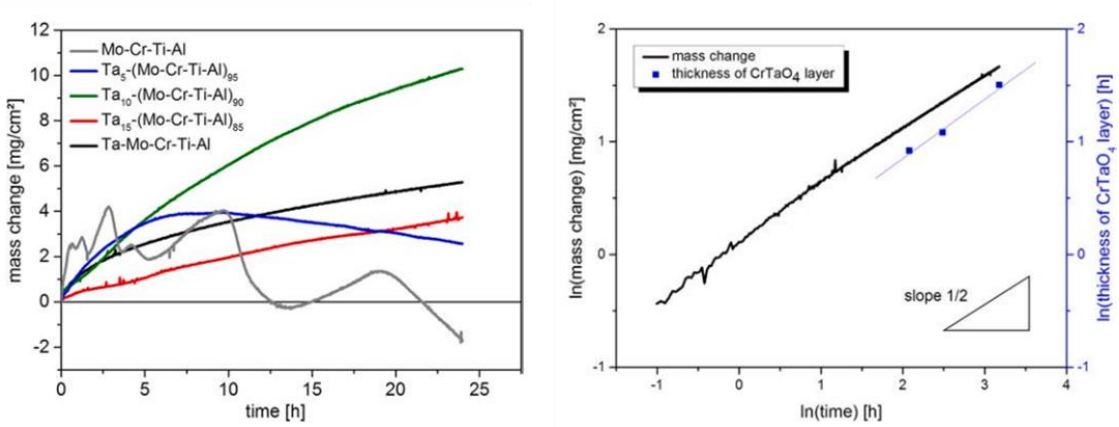

(a) (b)

Figure 2.13 - (a) Mass gain per area in function of time and (b) the analysis fitting for the equiatomic Ta-Mo-Cr-Ti-Al alloy. Adapted from Schellert et al. [76].

2.3.2 Oxidation thermodynamics

At high temperatures, the Gibbs energy variation is more negative and due to the exothermic nature of oxidation reactions in metals, such reactions are favored, and the reaction rate is higher [75].

The tendency of a given metal to react with oxygen and form an oxide can be defined by the Gibbs energy, as shown in Equation 10, in which $\Delta G°$ corresponds to the standard Gibbs energy and K to the reaction equilibrium constant [77].

Equation 10

$$\Delta G = \Delta G^0 + RT \ln K$$

The condition imposed for the spontaneity of a chemical reaction is that its Gibbs energy variation is less than or equal to zero, with chemical equilibrium reaching when this is zero, thus, Equation 11.

Equation 11

$$\Delta G^0 = -RT \ln K$$

Considering the reaction between oxygen and a metal M, in addition to the oxygen activity that corresponds to its partial pressure and this for pure solids is unity, the equilibrium constant can be described by Equation 12.

$$2M + O_2 \rightarrow 2MO$$

Equation 12

$$K = \frac{1}{P_{O_2}}$$

Replacing Equation 12 in Equation 11, the Equation 13 is resulted, which can be graphically represented by the Ellingham diagram, Figure 2.14, that allows the comparison of the thermodynamic stability of the oxides as a function of temperature and the activity of the reactants.

Equation 13

$$\Delta G^0 = RT \ln P_{O_2}$$

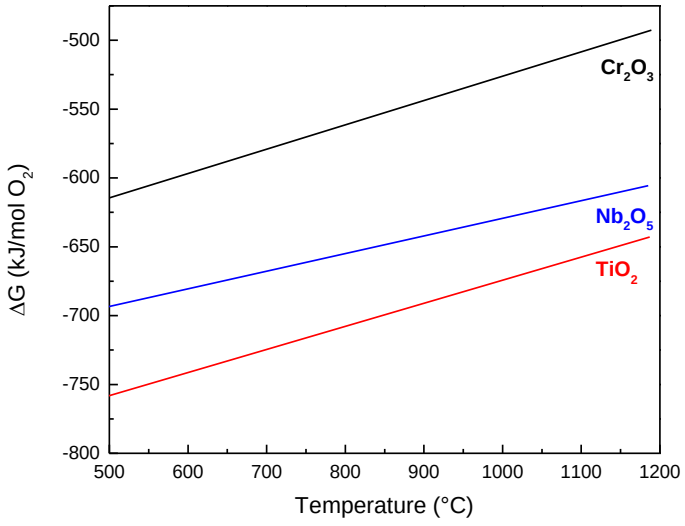

Figure 2.14 - Ellingham diagram for Nb, Ti and Cr main oxides formation. Data from HSC Chemistry Software Databases.

Furthermore, according to Adamian and Almendra [77], depending on the partial pressure of oxygen, some metals can form different layers of oxides with

different compositions, with the oxide richest in metal and with greatest stability being formed in contact with the metal, while less metal-rich and more oxygen-rich is formed in contact with the oxidizing atmosphere.

2.3.3 Sulfidation thermodynamics

Considering the H_2/H_2S gas mixture in equilibrium, Equation 14, the equilibrium constant K can be calculated with Equation 15, in which P_{H2} corresponds to the partial pressure of hydrogen, P_{S2} at the partial pressure of sulfur and P_{H2S} at the partial pressure of hydrogen sulfide [60, 78].

Equation 14

$$H_2S \leftrightarrow H_2 + \frac{1}{2}S_2$$

Equation 15

$$K = \frac{P_{H_2}\sqrt{P_{S_2}}}{P_{H_2S}} = exp\left[\frac{-\Delta G^0}{RT}\right]$$

Thus, considering a metal M, the sulfidation reaction can be expressed by Equation 16 and its Gibbs energy by Equation 17, therefore, the sulfur partial pressure, also called dissociation pressure, can be calculated by Equation 18.

Equation 16

$$xM + \frac{1}{2}yS_2 \rightarrow M_xS_y$$

Equation 17

$$\Delta G° = RTln\left(P_{S_2}\right)^{1/2}$$

Equation 18

$$\left(P_{S_2}\right)^{1/2} = exp\left[\frac{-\Delta G^0}{RT}\right]$$

As the oxidation process, the comparison of the thermodynamic stability of the compounds formed as a function of temperature is possible with the Ellingham [60], Figure 2.15.

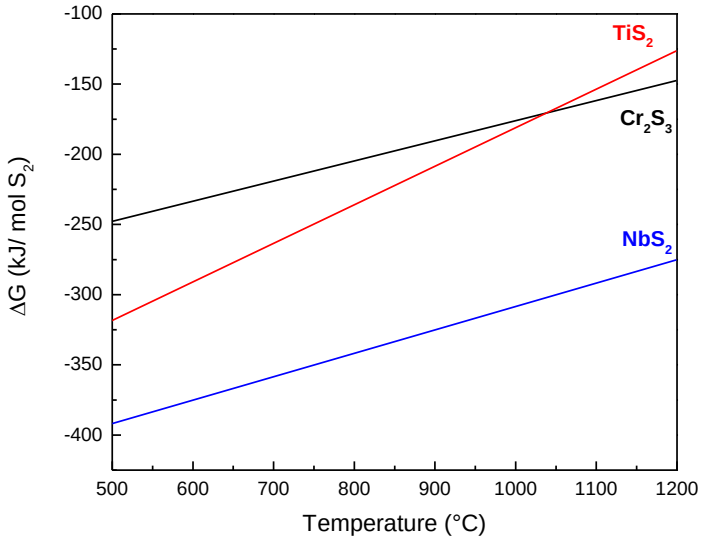

Figure 2.15 - Ellingham diagram for Nb, Ti and Cr main sulfides formation. Data from HSC Chemistry Software Databases.

3 MATERIALS AND METHODOLOGY

3.1 Materials

The studied MPE alloy was TiNbCr in condition as-cast and processed by HIP. The environmental degradation behavior was compared to the commercial Haynes 188, chosen for its noted high performance in sulfur-containing atmospheres.

The composition of TiNbCr MPE alloy in both conditions was determined by EDS analysis in at least three large areas, and the average of them and the deviation are shown in the Table 3.1. These analyses were made by a microscope of the brand ZEISS, model Sigma 500 VP SEM with Oxford Aztec X-EDS and analyze by Oxford Aztec software, the detector was SE, the work distance was 8.5cm, and it was done with 20.00kV High-Voltage and a current of 1.6µA. The microscope is installed in the University of Pittsburgh, at NFCF facilities in Pittsburgh – PA. The nominal composition oh Haynes 188 is shown in the Table 3.2

Table 3.1 - TiNbCr MPE alloy in condition as-cast and HIPed chemical composition based on EDS analysis.

Composition at.%	Cr	Nb	Ti
as-cast TiNbCr	29.6 ± 2.6	31.7 ± 2.3	31.9 ± 1.2
HIPed TiNbCr	33.7 ± 2.1	30.7 ± 1.5	29.8 ± 2.2

Table 3.2 - Haynes 188 Chemical composition in atomic percentage (at.%) [79].

B	C	Co	Cr	Fe	La	Mn	Nb	Ni	Si	Ti	W	O
0.015 max.	0.10	39 Bal.	22	3 max.	0.03	1.25 max	–	22	0.35	–	14	–

3.2 Methodology

3.2.1 TiNbCr MPE alloy

The microstructure prediction of TiNbCr MPE alloy was calculated by Calphad methodology using Thermo-Calc software with TCHEA05 Databases installed in a computer at University of Pittsburgh, in Pittsburgh-PA (Pitt).

The TiNbCr MPE alloy in condition as-cast was molten by vacuum arc melted in a furnace installed in University of São Paulo in Lorena-SP (DEMAREEL-USP), using high purity constituents (99.95%) and a high purity Ti getter was implemented to avoid oxidation. All the alloys were flipped and re-melted several times to ensure chemical uniformity.

The HIPed TiNbCr MPE alloy was molten by vacuum arc melted using high purity constituents (99.95%), re-molten several times and processed by High isostatic pressing (HIP) at 1400°C during 3h using the pressure equals to 207MPa, the heating and the cooling rates were 15°C/min and all of these steps were made in the Air Force Research Laboratory, Materials and Manufacturing Directorate, Wright-Patterson Air Force Base, OH.

3.2.2 TiNbCr MPE alloy: characterization

The microstructure of the TiNbCr MPE alloy in each condition was characterized by scanning electron microscope (SEM), Energy-dispersive spectrometer (EDS), X-ray diffraction (XRD), microhardness measurements, hardness measurements, density calculation and dilatometry test.

Aimed to analyze the morphology, phases and chemical composition by SEM and EDS, samples with 0.5x0.5x0.25 cm were cut, molten in an epoxy resin, and by conventional techniques they were prepared up to polishing with a diamond solution of 0.25µm. The SEM images were taken by a microscope of the brand FEI, model Apreo with EDAX EBSD & Octane Elite EDS Inspect S50, by CBS detector in mode all with 20.00kV High-Voltage and a current of 1.6µA. The EDS were made by a microscope of the brand ZEISS, model Sigma 500 VP SEM with Oxford Aztec X-EDS and analyze by Oxford Aztec software, the detector was SE, the work distance was 8.5cm, and it was done with 20.00kV High-Voltage and a current of 1.6µA. Both microscopes were installed in the University of Pittsburgh, at NFCF facilities in Pittsburgh – PA.

Aimed to identify and quantify the phases of the TiNbCr MPE alloy, X-ray diffraction (XRD) analyses were performed using a 0.5x0.5x0.25 cm samples polished up to 25µm of a diamond solution. A diffractometer Bruker system, installed in the Federal University of São Carlos, at LCE facilities in São Carlos –

SP, was used with Kα radiation from copper, in the range of 2θ from 30º to 90º, with a step of 0.02º during 1h, and analyzed using the software GSAS-II, enabling the identification of the phases.

As the phase composition and difference of defects density impact the mechanical properties, the Rockwell C hardness (HRC) measurements were performed using a Rockwell C hardness tester, of the brand Pantec Panambra, model RASN, and the measurements of Vickers microhardness (HV) were performed using a microhardness tester of the brand Shimadzu, model HMV2, and load of 1 Kgf, for 10 seconds, both are installed in the Federal University of Alfenas, Poços de Caldas – MG (Unifal). Approximately, 10 measurements were taken, and the results showed are the average of it.

Different processing results in different defects density, so to quantify this difference between both conditions of the MPE alloy, the density of the TiNbCr alloy in both conditions were calculated by Archimedes principles, Equation 19. For it, TiNbCr MPE alloy 0.5x0.5x0.25 cm samples of each conditions had the mass measured by an analytical scale dry (m_1), wet (m_2) and dry wet (m_3). For the wet measurement, the samples were in water and vacuum during 48h to allow that the water penetrates all porous, (m_2). After this measurement, the edges were dried, and a new mass was measured (m_3).

Equation 19

$$\rho = \frac{m_1}{(m_3 - m_2)} \rho_{water}$$

The last analysis the alloy characterization was dilatometer tests. They were aimed to evaluate the phase transformation and coefficient thermal expansion (CTE). For it, tests were performed using Netzsch Thermomechanical Analyzer (TMA) 402 F1 vertical dilatometer with a heating/cooling rate of 10°C/min, temperatures from 25 to 1200°C with an isothermal of 5min at 1200°C, in high purity nitrogen gas, installed at University of Pittsburgh, in Pittsburgh-PA (Pitt). The tests were done in triplicate and the only average results were shown. After the tests, samples were characterized by SEM, EDS and XRD.

3.2.3 Oxidation behavior: Anisothermal tests in air

As the TiNbCr MPE alloy was initially designed for supersonic applications, understanding the early stages of oxidation is crucial, particularly for space applications that require materials to exhibit satisfactory behavior within a very short period of application. The early stages of oxidation of the TiNbCr MPE alloy were investigated through anisothermal tests.

For it, samples of TiNbCr MPE in both conditions with 0.5x0.5x0.2 cm were prepared using SiC foil until 1200 mesh, cleaned by ultrasound bath with ethanol and tested in a tube furnace installed at University of Pittsburgh, in Pittsburgh-PA (Pitt). To compare the oxidation behavior of the TiNbCr MPE alloy, Haynes 188 samples were used in condition as-received, as control samples and prepared by the same way that the MPE.

The first step of the anisothermal oxidation test was to know the temperature profile of metal samples in the furnace that would be used for the tests. For it, one sample of Haynes 188 was welded in a thermocouple wire type K and connected to the Omega software to read the temperature. Following this, the durations for keeping the samples in the furnace were defined based on the desired temperatures: 600, 900, and 1100°C. These temperatures encompass the range of interest for this study (600-1100°C). Since only three temperatures are required for this type of characterization, the temperature of 900°C was selected in an attempt to reduce errors arising from the short exposure time.

The furnace was programmed to 1100°C; consequently, samples of each alloy were subjected to defined durations: 18s (600°C), 30s (900°C), and 50s (1100°C). Furthermore, additional tests were conducted at 180s (3min) and 1800s (30min) to enhance the characterization at the highest temperature.

The mass measurement was taken before and after each test, and the area used to calculate the mass gain per area was the initial surface area calculated by the software Image J. This software enables more accurate measurements to be conducted due to the angled shapes in the corners of the samples.

All tested samples were characterized by SEM, EDS with the same equipment and parameters mentioned before; and XRD by diffractometer Bruker

D8 XRD system, installed in the University of Pittsburgh, at NFCF facilities in Pittsburgh – PA, with Kα radiation from copper, in the range of 2θ from 20 to 95.5°, with a step of 0.5º for 2 s/step, and analyzed using the software Search-Match.

3.2.4 Oxidation behavior: Isothermal tests in air

Considering that the alloy is expected to primarily encounter service conditions involving air-containing environments, the oxidation tests were conducted in an air atmosphere.

The isothermal oxidation tests in air were conducted in a tube furnace at 800, 900 and 1000°C during 20, 60 and 100h. For it, TiNbCr MPE alloy in both conditions and Haynes 188 samples with approximately 1x0.5x0.25 cm were cut as shown in Figure 3.1, with a hole of ~2mm of diameter and they were prepared using SiC foil until 1200 mesh and cleaned by ultrasound bath with ethanol.

Figure 3.1 - Oxidation testing sample.

Samples were hanged in a Kanthal wire above an alumina crucible and inserted into the furnace where they were kept during 20, 60 and 100h. The mass measurement was taken before and after each test and the area using to calculate the mass gain per area was the initial superficial area calculated by the software Image J, as in the case of anisothermal tests.

The topography section of each sample was characterized by SEM, EDS and XRD, as described before and to characterize the cross-section, the sample was molten in epoxy resin and polished up to 0.25 µm with a diamond solution, and analyzed by SEM and EDS.

Like anisothermal tests, to compare the TiNbCr MPE alloy behavior, the Haynes 188 was tested under same conditions.

3.2.5 Oxidation behavior: cyclic tests in air

In addition to evaluating the degradation behavior in air, cyclic tests were performed. They were conducted in an automatic furnace of WT Industry with a software to control the furnace movement up and down, installed at Federal University of São João del-Rei São João del-Rei -MG (UFSJ), and just HIPed TiNbCr MPE alloy was tested at 800 and 900°C, involving 100 cycles with each lasting 60 minutes, followed by a 10-minute period at room temperature. Additionally, due to observed spallation at 900°C, a sample was suspended above a crucible to collect as much spallation as possible.

For it, samples were prepared as described in the isothermal tests methodology and the characterization followed the same steps, however conducted at Federal University of São João del-Rei São João del-Rei -MG (UFSJ).

3.2.6 Oxidation behavior: Isothermal tests in oxygen

Since air degradation involves both degradation due to oxygen (oxidation) and nitrogen (nitritation), isothermal tests with only oxygen, in the same proportion as in air, were conducted using TGA analysis. The tests in oxygen were conducted in a Setaram Thermogravimetry (TGA) model SETSYS Evolution installed at University of Pittsburgh, in Pittsburgh - PA (Pitt), at 700, 800, 900 and 1000°C during 100h with a gas mixture composed of Ar and 21% of oxygen, in volume, in a 20mL/min flow.

For it, samples similar to isothermal tests in air were prepared for as-cast and HIPed TiNbCr MPE alloy and Haynes 188. The characterization followed the same steps of those tests.

3.2.7 Sulfidation & Oxidation behavior: Isothermal tests

As highlighted in the literature review, there is a knowledge gap regarding the environmental degradation behavior of MPE alloys, primarily due to limited investigations in air and oxygen environments [2, 17]. Additionally, it is acknowledged that the behavior significantly differs in environments containing

sulfur, and beyond temperatures of 645°C, there are no commercially available alloys.

For it, isothermal sulfidation & oxidation tests H_2S/H_2 gas mixture (5% of H_2 and 1000ppm of H_2S) were conducted in a tube furnace with a set-up schematically shown in Figure 3.2, at 600, 800, 900, 1000 and 1100°C during 20, 60 and 100h.

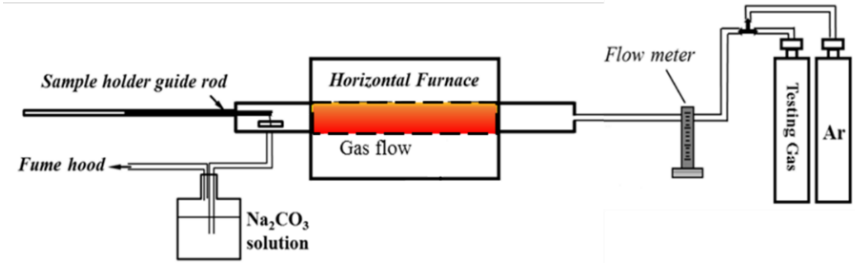

Figure 3.2 - Schematic representation of the furnace set-up used for sulfidation & oxidation and sulfidation tests.

For sulfidation & oxidation tests, samples with 0.5x0.5x0.25 cm were prepared as oxidation tests and were deposited in an alumina crucible in a flat way instead of hanged and the crucible was hanged in an alumina tube. The system was closed, and the High purity Ar cylinder gas was opened to check the leak presence. If no leak were detected, the Ar cylinder was closed and the cylinder with the commercial gas mixture composed of Ar, 5% of H_2 and 1000ppm of H_2S was opened and the flush was controlled by the flow meter. So, the samples were inserted into the furnace until its middle by the magnet holder and the kept there during 20, 60 or 100h. After the test, the samples were moved out to the furnace by the magnet holder, the gas mixture was switched by the Ar flush during 1h and after it the system was opened to remove the samples.

With this methodology, the log of partial pressure of oxygen was estimated in -6 and the partial pressure of sulfur was calculated by HSC Chemistry software installed in a computer at University of Pittsburgh, in Pittsburgh – PA (Pitt), and the log of partial pressure of sulfur was -3. The system pressure was kept in 1 atm.

The characterization followed the same steps of oxidation tests, however due to the energy overlap of Nb and S, for SEM and EDS analysis, 30.00kV High-Voltage was used instead of 20.00kV.

Additionally, a stability diagram with the partial pressure of oxygen and sulfur was calculated by HSC software databases installed in a computer at University of Pittsburgh, Pittsburgh – PA (Pitt). Due to the similarity between the obtained results for each temperature, only at 800°C is shown in the Figure 3.3, where it is possible to note the formation of oxides and sulfides in the surface of the alloy in sulfidation & oxidation tests.

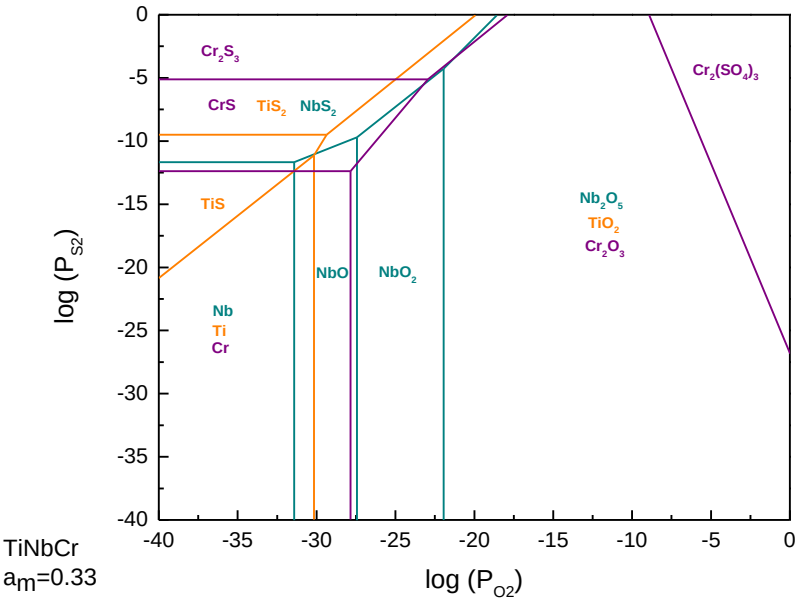

Figure 3.3 - Stability diagram for TiNbCr MPE alloy considering the same activity of each element, at 800°C. Data from HSC Chemistry Software Databases.

3.2.8 Sulfidation behavior: Isothermal tests at 800°C

Focused on isolating the degradation exclusively due to the presence of sulfur, sulfidation tests were performed. Similar to sulfidation & oxidation tests, the sulfidation tests were conducted at 800°C, with the same samples' preparation, apparatus and gas mixture. However, aimed to avoid oxidation process in the TiNbCr MPE alloy, the partial pressure of oxygen was decreased until a log of partial pressure of oxygen approximately equals to -26, which according to the HSC database prediction only sulfides were expected to be formed in the surface, Figure 3.3.

Considering the ideal gas equation (Equation 20) and the temperature is uniform inside of the reaction tube, a model of O_2 mole proportion dilution was developed (Equation 21).

Equation 20

$$PV = nRT\ ,$$

where P is the Partial pressure of oxygen to avoid oxidation, based on the stability diagram it should be smaller than $log_{(P_{O_2})} = -23$, so the value of -26 was selected, V is the volume of the reaction tube (3000mL), n is the number of mols of O_2, R is the ideal gas constant and T is the temperature of tests (800°C).

Equation 21

$$\frac{dn}{dt} = exp\left[\frac{(-vT_2t)}{VT_1}\right],$$

where t is the necessary time to purge the gas mixture before to start the tests, v is the flow rate of the reaction gas (150mL/min), T_1 is the room temperature (25°C) and T_2 is the average temperature between the beginning, middle and the end of the tube.

Following the model shown in Equation 21, the gas mixture should be purged during approximately 7h before to insert the samples. And before it, the Ar in high purity was purged during the doble of the time. So, the methodology followed the steps:

1) Ar Purge: 14h.
2) Gas mixture flush: 7h.
3) Test: holding samples until the middle of the furnace by the magnetic holder and kept then during 20, 60 or 100h.
4) Ar purge: 1h.
5) Open the system, remove samples, and check the mass gain per area (initial area).

Additionally, the characterization followed the same steps of sulfidation & oxidation tests.

4 RESULTS AND DISCUSSION

4.1 Microstructure characterization

The Thermodynamic calculation to predict the microstructure of the TiNbCr MPE Alloy is shown in Figure 4.1, where is possible to highlight that the solidification of the alloy starts with BCC phase at 1615°C and is completed at 1457°C by a eutectic reaction with ~0.20 of remaining liquid, as shown in the Equation 22.

Equation 22

$$Liq \leftrightarrow BCC + Laves\ C14$$

After the solidification, the alloy is composed of a BCC matrix with Laves Phase C14 precipitated. Additionally, during cooling, is observed that decreasing temperature generate decreasing of BCC phase and increasing Laves Phase and an allotropic transformation of Laves Phases occurs at ~1212°C in which the hexagonal Laves C14 is transformed in Cubic Laves C15.

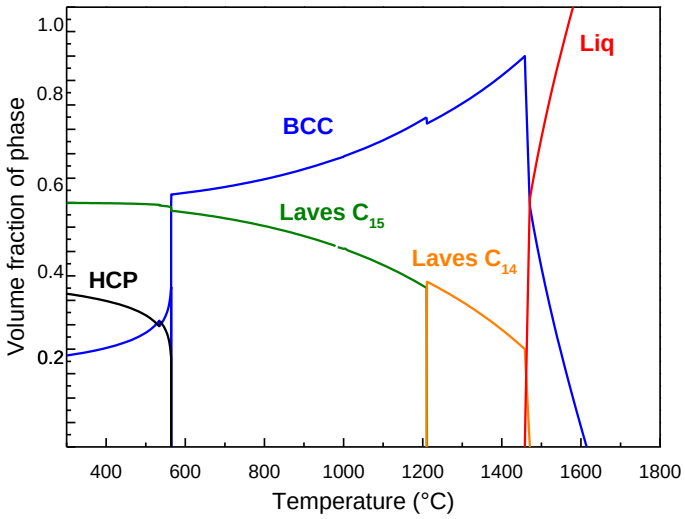

Figure 4.1 - Phase Diagram calculated by Calphad methodology using the Thermo-Calc database HEA05.

During their studies, Butler et al. [19] calculated by Pandat Pandat Nb2020 Database the phase fraction in function of temperature of TiNbCr and NbCr MPE alloys and they observed for the TiNbCr MPE alloy that the solidification should

be done at 1485°C with 0.24 of remaining liquid and the allotropic transformation of Laves phase occurs at 1309°C.

Comparing the microstructure of TiNbCr MPE alloy with NbCr Alloy, Butler et al. [19] noted an inversion in the microstructure. While the binary alloy is composed of a Laves matrix with BCC precipitates—coarse, near-spherical primary particles, and fine lamellar—the addition of Ti allows for an alloy composed of a BCC matrix with Laves phase precipitates. The increase in the volume fraction of BCC is attributed to the decrease in the fraction of the eutectic constituent. This decrease is influenced by the amount of Cr in the alloy and its solubility in the BCC phase, impacting the volume fraction of the Laves phase.

As mentioned earlier, this study evaluates the TiNbCr MPE alloy in both as-cast and HIPed conditions. The density of each condition and the theoretical value is presented in Table 4.1.

Analyzing Table 4.1, it a slightly decreasing in the density after the HIP processing is noted, suggesting that the HIPed condition exhibits more porosity than the as-cast condition. This discrepancy raises the question of whether the processing aimed at reducing the alloy porosity was not effective or if this difference occurred due to the use of a different melting furnace to obtain the alloy. Another hypothesis is that the disparity may be attributed to the difference in phase fraction identified in the XRD analysis (Figure 4.2). The XRD patter of each condition is shown in Figure 4.2 and BCC and Laves Phases fractions were calculated by Rietveld Refinement.

Table 4.1 - TiNbCr MPE alloy density.

	as-cast TiNbCr MPE alloy (g/cm^3)	HIPed TiNbCr MPE alloy (g/cm^3)	Theoretical TiNbCr MPE alloy (g/cm^3)
Density	6.68	6.54	6.70

Figure 4.2 highlights that the Laves Phase fraction for as-cast condition is 0.15 and for HIPed condition is 0.37. Additionally, as-cast exhibited two BCC phases with different lattice parameter, which suggest segregation. However, during the HIP processing, temperature promoted the reduction of the segregation and Laves phase precipitation.

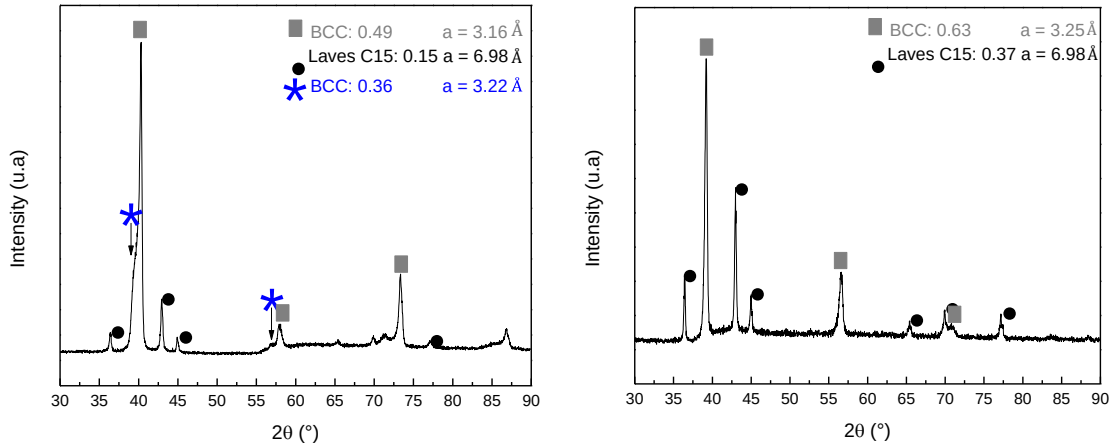

(a) (b)

Figure 4.2 - XRD spectra and Phase fraction of (a) as-cast and (b) HIPed TiNbCr MPE alloy.

The difference in microstructure reflects in the alloy's properties due to the variance in their morphology and crystal complexity. Comparing the BCC matrix with the Laves Phase precipitates, the first has more discordance mobility than the precipitates due to its simpler structure [80, 81]. Therefore, the presence of the Laves Phase reduces the ductility of the alloy, similar to segregation. This characteristic is evident in the results of hardness and microhardness tests, as presented in Table 4.2.

Table 4.2 - Hardness and Microhardness values for as-cast and HIPed TiNbCr MPE alloy.

Alloy condition	Hardness (HRC)	Microhardness (HV)
as-cast	48.92 ± 1.06	477.58 ± 1.21
HIPed	45.37 ± 0.98	460.63 ± 1.17

This observation is supported by the mechanical behavior investigation done by Butler et al. [19] comparing the NbCr and TiNbCr MPE alloy. As mentioned before, the first alloy was composed of a Laves matrix with BCC precipitates and the second the microstructure was the opposite. When the researchers submitted the alloys in compression tests at 25, 1000 and 1200°C, they observed that the binary alloy (NbCr) exhibited higher values of mechanical resistance (1670MPa at 25°C, 1480MPa at 1000°C and 1074MPa at 1200°C),

however no ductile behavior at 25 and 1000°C. On the other hand, the ternary alloy (TiNbCr) exhibited values quietly smaller at 25°C (1659MPa at 25°C, 218MPa at 1000°C and 60MPa at 1200°C) and a ductile behavior.

The SEM and EDS mapping for as-cast and HIPed conditions are shown in Figures 4.3 and 4.4, respectively. Additionally, the EDS results for the points 1-4 are at the Table 4.3.

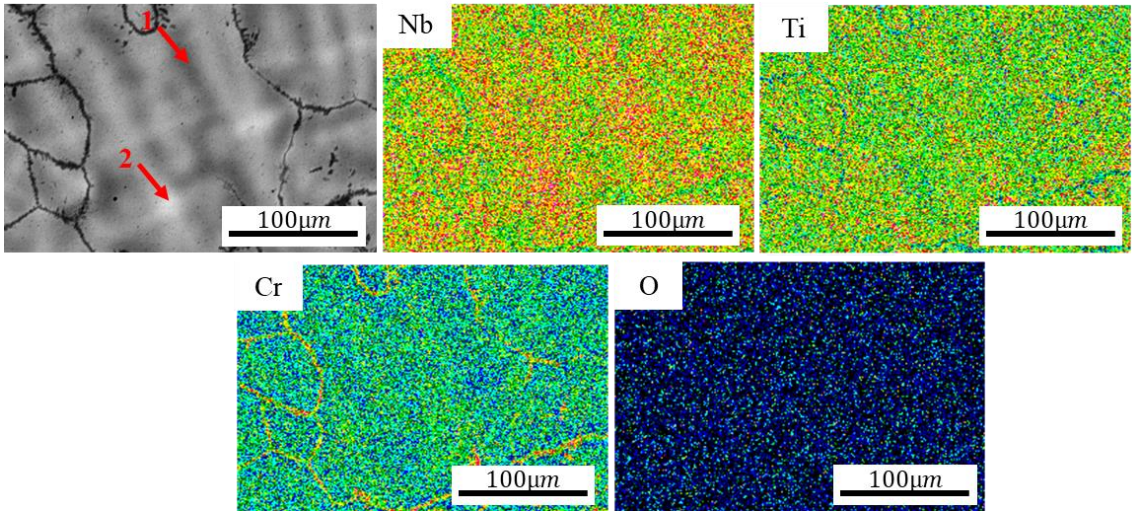

Figure 4.3 - SEM images took by BSE and EDS mapping for as-cast TiNbCr.

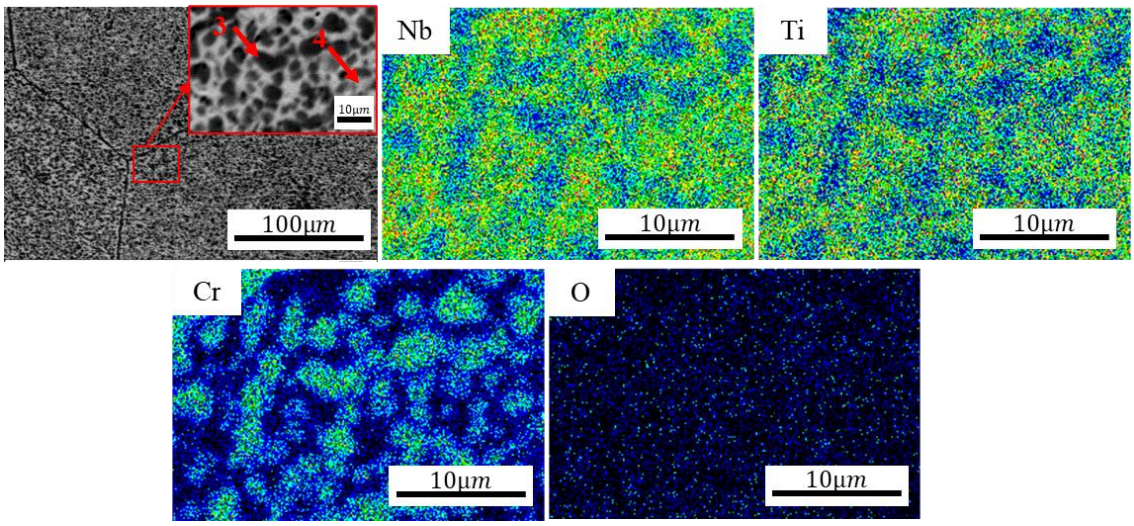

Figure 4.4 - SEM images took by BSE and EDS mapping for HIPed TiNbCr.

Table 4.3 - EDS results of points 1-4 showed in Figure 4.3 and 4.4.

Composition at.%	Cr	Nb	Ti	O
1	31.4 ± 2.1	28.3 ± 1.6	33.3 ± 0.2	6.7 ± 0.3
2	30.5 ± 0.7	32.4 ± 2.1	30.9 ± 1.9	6.3 ± 0.1
3 – Laves Phase	59.7 ± 0.8	21.2 ± 0.2	18.9 ± 0.6	0.2 ± 0.1
4 – BCC matrix	14.7 ± 0.8	35.2 ± 0.4	37.4 ± 0.9	12.7 ± 1.4

Analyzing Figures 4.3 and 4.4 it is noted that there is a difference between the structures of the TiNbCr MPE alloy in both conditions. The as-cast condition displays a dendritic morphology, composed of Nb and Ti-rich BCC dendrites interspersed with fine (Nb,Ti)Cr_2 Laves precipitates along grain boundaries, Figure 4.3. Similar observations were reported by Welch et al. [33] for the TaTiCr MPE system. Conversely, HIP processing resulted in a microstructure characterized by BCC grains with Laves phase precipitates. Welch et al. [33] observed a similar microstructural evolution in TaTiCr MPE system alloys after HIP processing. This transformation occurred in the solid state due to a reduction in chromium solubility during cooling and within the grain boundaries, driven by the eutectic reaction.

During the TiNbCr MPE alloy development, Butler et al. [19] characterized the HIPed alloy, processed under the same conditions that this study, as a BCC matrix with cubic Laves phase (C15) containing {111} <110> twins and, by EBSD analysis, the hexagonal Laves structure (C14) was observed at twins boundaries inside C15 particles. A detailed analysis of the crystallographic orientations of the adjacent C14 and C15 regions allowed the identification of the orientation <101>C15 || <2110>C14. This transformation of Laves phase from C14 to C15 occurs by synchroshear which may result in twinned structure of C15 phase [80, 81], as described by Butler et al. [19].

However, the C14 phase at twin boundaries of C15 phase is a metastable equilibrium, high temperature phase retained after the transformation, as observed by Kim et al. [82] for Zircaloy-4 alloy and Mg-Zn-Y alloy, Butler et al. [19] for TiNbCr and TaTiNbCr MPE alloys and Welch et al. [33] for TaTiCr MPE alloy.

The formation of Laves phase, A_2B, occurs only when the component A is ~1.1-1.3 times smaller than component B. While the atomic radius of Nb and Ti

are 143 and 146pm, respectively, the atomic radius of Cr is 125pm, approximately 1.15 times smaller. So, the Laves phase in TiNbCr MPE Alloy can only form by the reaction of Cr with other elements and the amount of Cr in Laves phase should be around 66.6 at.% [19, 83, 84].

However, according to Table 4.3, Laves phase has around 59.71 at.% of Cr and it suggests that some Cr sites in this phase are vacant or filled with other, larger atomic radius alloying elements [83] as investigated by Butler et al. [19] for TiNbCr and TaTiNbCr MPE alloys.

Aimed to investigate the phase transformations of Laves phase and the HCP, shown in the Figure 4.1, dilatometry tests were performed, and the results are shown in Figure 4.5 and Table 4.4.

Figure 4.5 and Table 4.4 highlight a difference in the phase transformation temperature compared to the Figure 4.1, which may occur due to the kinetics. While the thermodynamic calculation shows the allotropic transformation of Laves Phases at 1212°C, the dilatometry tests show that it occurs around 900°C. And, for the HCP phase is expected this transformation at 564°C (Figure 4.1), however, it occurs around 640°C (Figure 4.5).

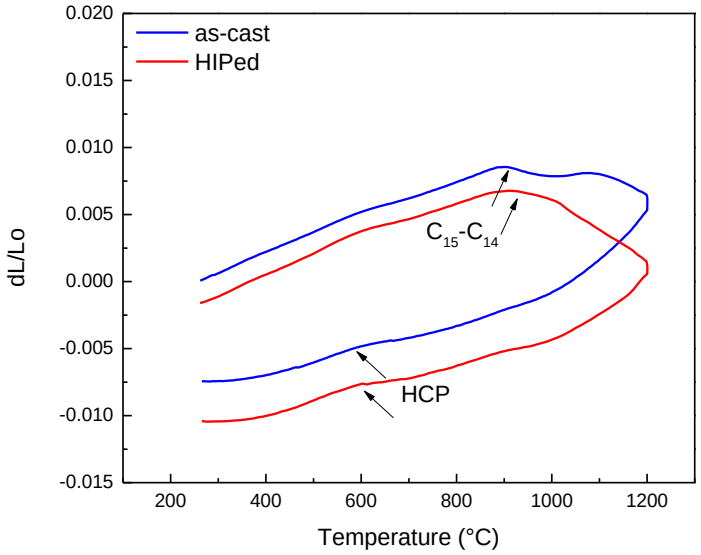

Figure 4.5 - Dilatometry results of as-cast and HIPed TiNbCr MPE alloy at 1200°C in Nitrogen.

Table 4.4 - Average of dilatometry tests of TiNbCr MPE alloy.

Alloy condition	CTE heating (10^{-5})	CTE cooling (10^{-5})	HCP formation (°C)	Transformation C_{15}-C_{14} (°C)
as-cast	0.86 ± 0.06	1.31 ± 0.06	636.01 ± 0.69	914.83 ± 3.01
HIPed	0.87 ± 0.06	1.31 ± 0.07	647.59 ± 0.94	902.62 ± 1.39

Additionally, due to the phase transformation of Laves phase (C15-C14) highlighted in the Figure 4.5 during the heating which generated different microstructure, a difference in the CTE during heating and cooling is highlighted in the Table 4.4.

After the dilatometry tested, the microstructure of each sample was characterized by SEM/EDS and XRD, as shown in Figures 4.6 – 4.8 and Table 4.5. As highlighted in Figure 4.5, TiNbCr MPE alloy in both conditions exhibited the formation of HCP phase during the cooling with a rate equals to 10°C/min and this fact is supported by XRD analysis, Figure 4.8.

According to SEM images and EDS analysis, Figures 4.6 and 4.7 and Table 4.5, the HCP is Ti-rich phase that precipitated around the Laves phase due to the Ti diffusion, and its morphology is thinner in the as-cast MPE alloy than HIPed, following the trend of Laves phase before the dilatometry.

The comparison between EDS analysis, Tables 4.3 and 4.5, suggests that the allotropic transformation of Laves phase decreases the Ti content into the Laves phase and the formation of HCP does not deplete the BCC matrix significantly in Ti, so a decomposition of BCC in BCC and HCP may not occur. Additionally, the occurrence of oxygen is noted due to the oxidation reactions that happen during the dilatometry tests because of the presence of oxygen as impurity in the gas composition.

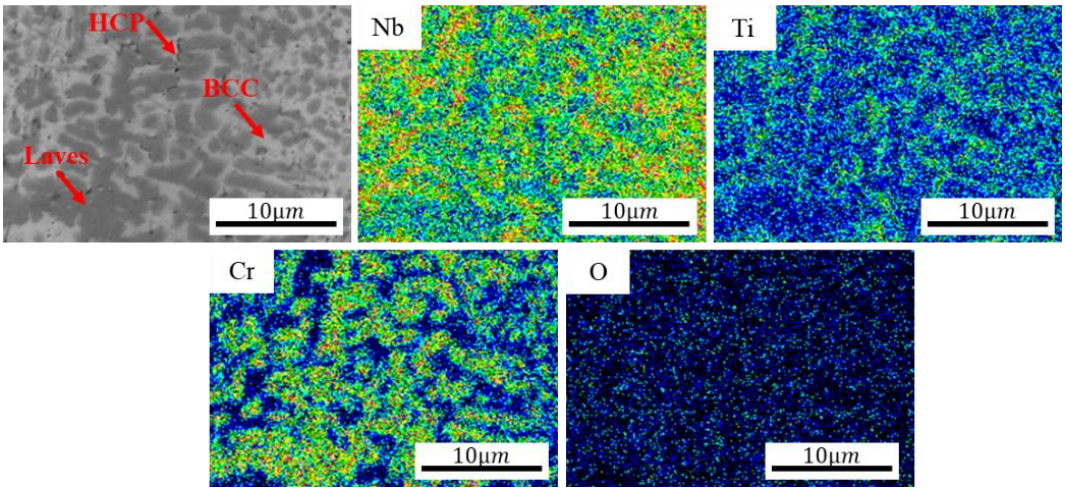

Figure 4.6 - SEM images by BSE and EDS mapping for as-cast TiNbCr after dilatometry test.

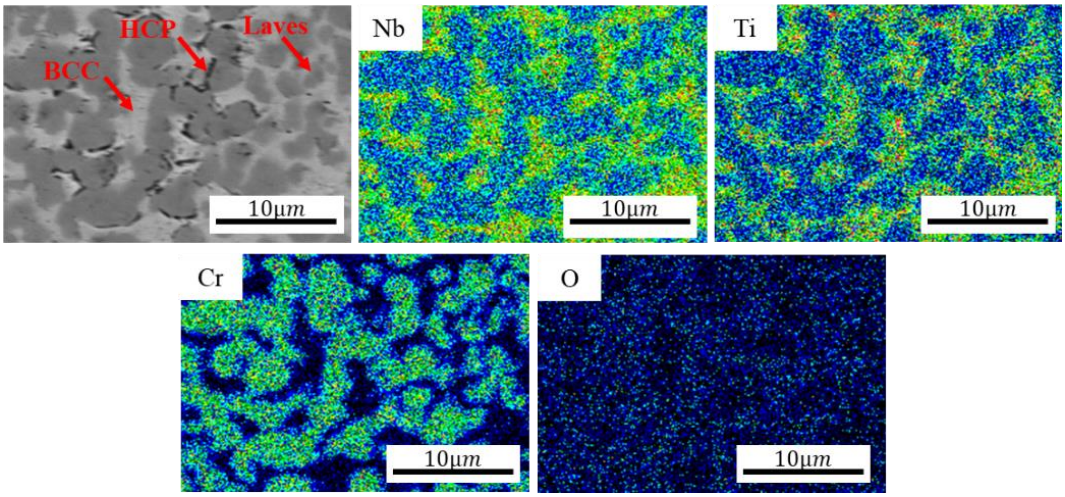

Figure 4.7 - SEM images by BSE and EDS mapping for HIPed TiNbCr after dilatometry test.

Table 4.5 - EDS results of phases shown in the Figures 4.6 and 4.7.

Composition at.%	Cr	Nb	Ti	O
BCC	11.5 ± 0.9	41.9 ± 2.0	34.4 ± 1.9	12.2 ± 1.5
HCP	10.3 ± 1.0	23.4 ± 1.2	50.8 ± 2.3	15.5 ± 0.9
Laves	37.7 ± 2.2	23.4 ± 1.3	28.2 ± 1.6	10.7 ± 1.4

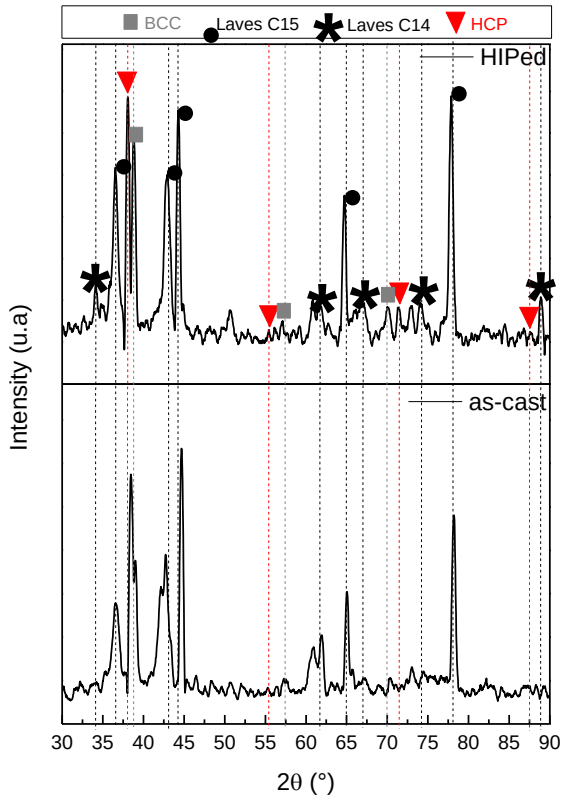

Figure 4.8 - XRD spectra of as-cast and HIPed TiNbCr MPE alloy after dilatometry tests.

4.2 Oxidation Behavior: Early-stages

The early-stage oxidation behavior of the TiNbCr MPE alloy in both conditions was assessed through anisothermal tests in air and compared to Haynes 188. As detailed in the methodology section, the initial step involved determining the duration for the metal samples should be kept inside the furnace based on the temperature. To achieve this, the temperature profile was determined with Haynes 188 and is illustrated in Figure 4.9.

Analyzing the temperature profile, Figure 4.9, it is noted that to achieve 600°C the metal took ~18s, 900°C ~30s and 1100°C ~50s. Aimed to characterize the early-stages of oxidation behavior at 1100°C, samples of each alloy were tested during 180 and 1800s.

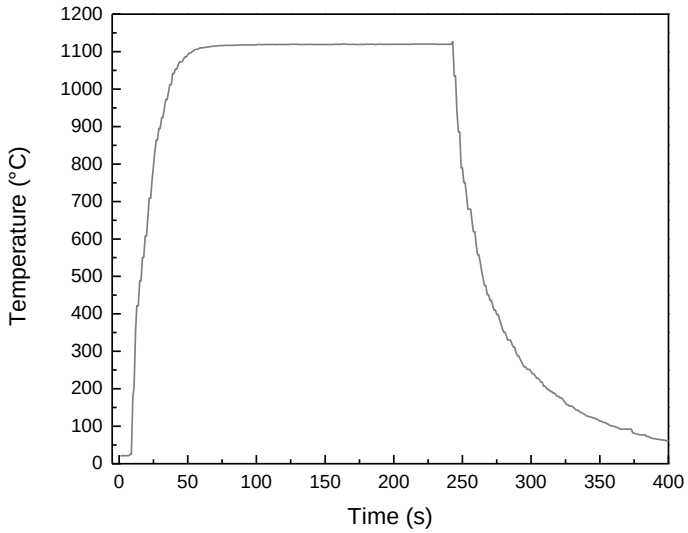

Figure 4.9 - Temperature profile obtained with Haynes 188 in the tube furnace.

The mass gain/area in function of the time that samples were tested is shown in Figure 4.10. Due to the chemical similarity between the MPE alloys, the characterization of oxidized samples was done for condition HIPed because it exhibited higher mass gain and with it the cross-section analysis could be possible by XRD and SEM/EDS, Figures 4.11 and 4.12, and Figures 4.14 and 4.16.

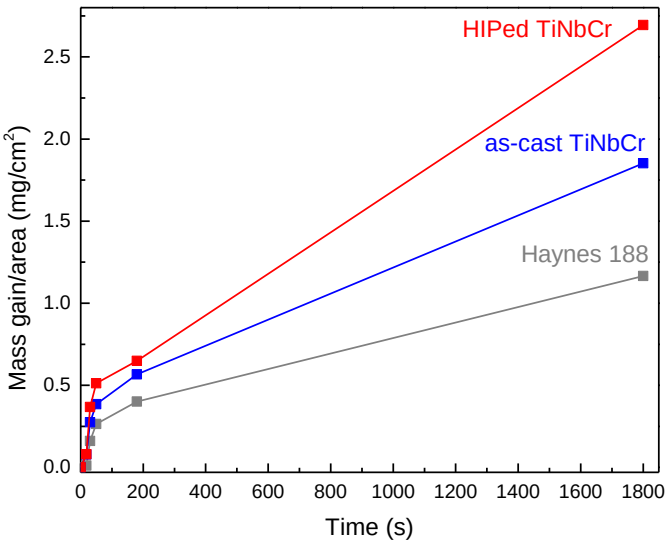

Figure 4.10 - Mass gain per area in function of time of as-cast and HIPed TiNbCr MPE alloy and Haynes 188, tested in air.

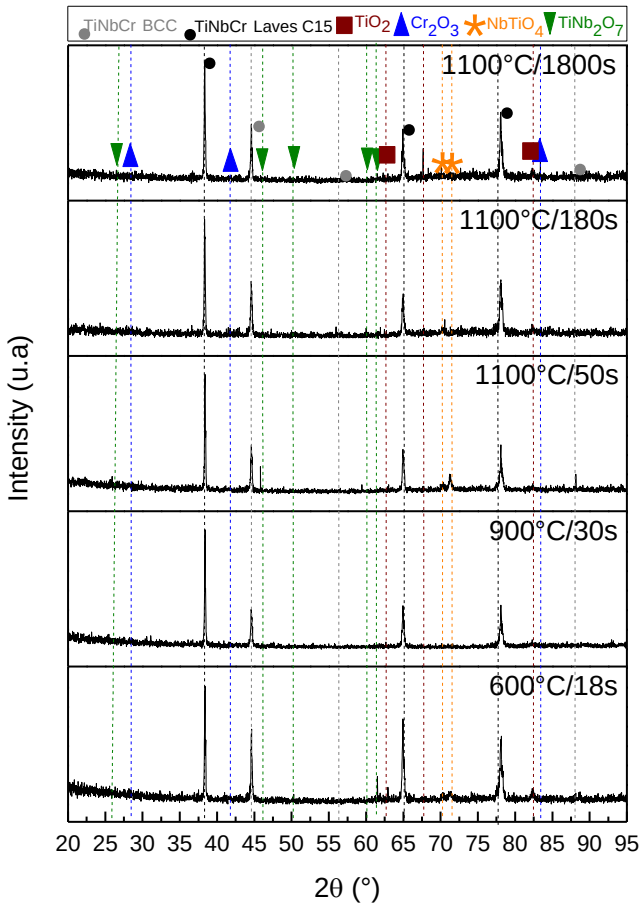

Figure 4.11 - XRD spectra of HIPed TiNbCr MPE alloy tested in air during 18, 30, 50, 180 and 1800s.

Analyzing Figure 4.11, it is possible to highlight that while an increasing time/temperature of the test the Cr_2O_3 become favorable, the complex oxides become not favorable suggested by the reduction of peaks.

According to Jiang et al. [44], the interaction between Nb and Ti in the oxidation behavior is directly related to the Nb fraction in the alloy. While in alloys with less than 15 at.% of Nb presents Nb in a solid solution of TiO_2 causes a reduction in the kinetics rate, the higher fraction generates an increase in it due to the formation of complex oxides, like $NbTiO_4$ and $TiNb_2O_7$ observed by XRD, Figure 4.11.

Complex oxides can be formed by the reaction of simple oxides. Due to the high solubility and fast kinetics, Nb and Ti react with the environment and their oxides react according resulting in $NbTiO_4$ and $TiNb_2O_7$ [4, 32, 85, 86].

Analyzing the cross-sections of the TiNbCr MPE alloy and Haynes 188, Figures 4.12 and 4.13 it is possible to observe that Haynes 188 achieved the supersaturation in the surface faster than TiNbCr MPE alloy because at 50s a thin external scale is developed, and it is adherent and protective due to no internal oxidation. This fact may occur due to the more complex two-phase morphology that the MPE alloy has composed of a BCC matrix with Laves phase precipitates.

However, after achieving supersaturation and forming the external scale, the TiNbCr MPE alloy does not develop a sufficiently protective scale, as indicated by the internal oxidation occurrence. This internal oxidation occurs due to the diffusion of gas through the scale, where a portion is consumed by the scale growth, and the remainder maintains contact with the alloy surface, penetrating the alloy, causing internal oxidation, forming TiO_2 and oxides rich in Nb, Ti and Cr in the phase boundaries and BCC matrix, respectively.

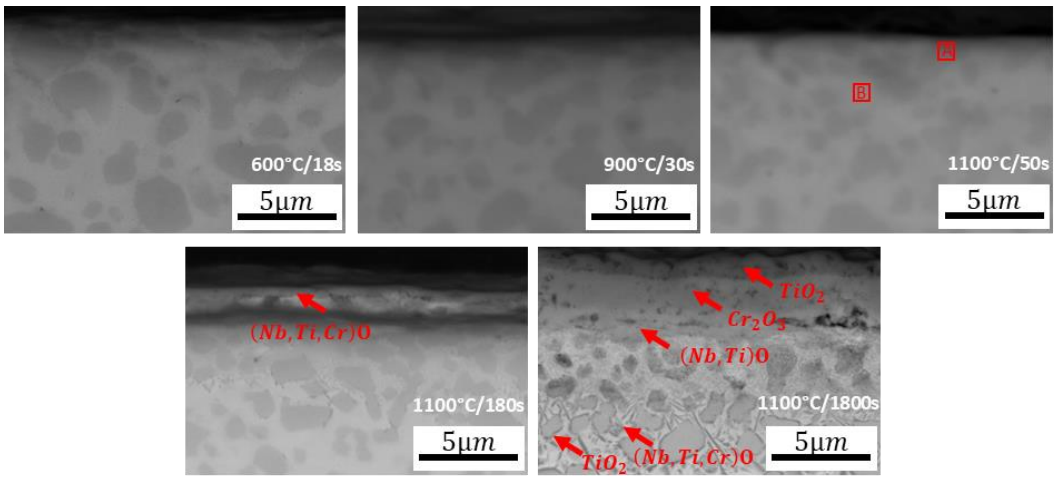

Figure 4.12 - Cross-section of HIPed TiNbCr MPE alloy tested in air obtained by SEM.

Table 4.6 - Chemical composition of areas A and B from Figure 4.12 obtained by EDS.

Composition at.%	Cr	Nb	Ti	N	O
A – Laves	53.1 ± 2.9	17.3 ± 1.4	19.6 ± 1.5	0.0 ± 0.0	10.0 ± 1.1
B – BCC	16.9 ± 1.1	32.8 ± 2.1	37.1 ± 2.1	0.0 ± 0.0	13.3 ± 1.1

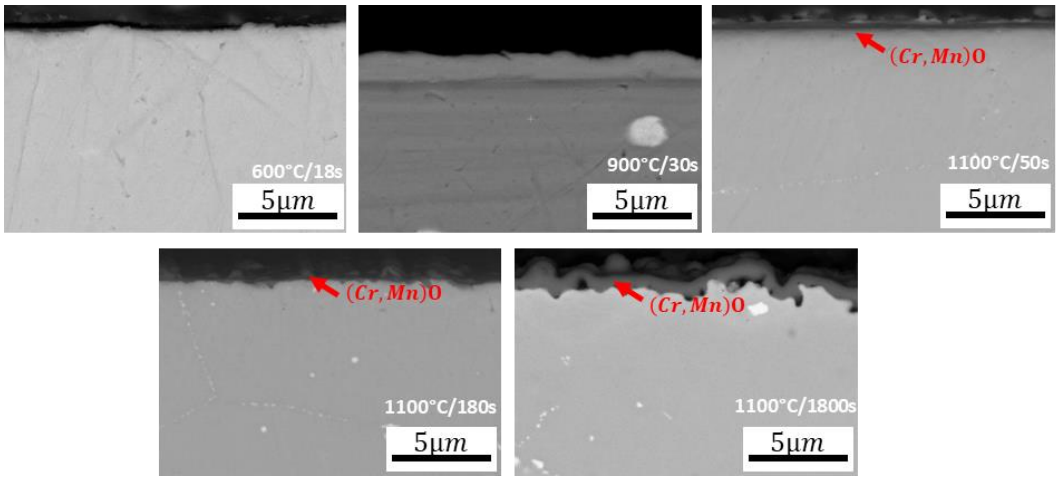

Figure 4.13 - Cross-section of Haynes 188 tested in air obtained by SEM.

The elements distribution after 50s testing is shown in the Figures 4.14 and 4.15 for the HIPed TiNbCr MPE alloy and Haynes 188, respectively. And after 1800s testing in the Figure 4.16 for de HIPed MPE alloy.

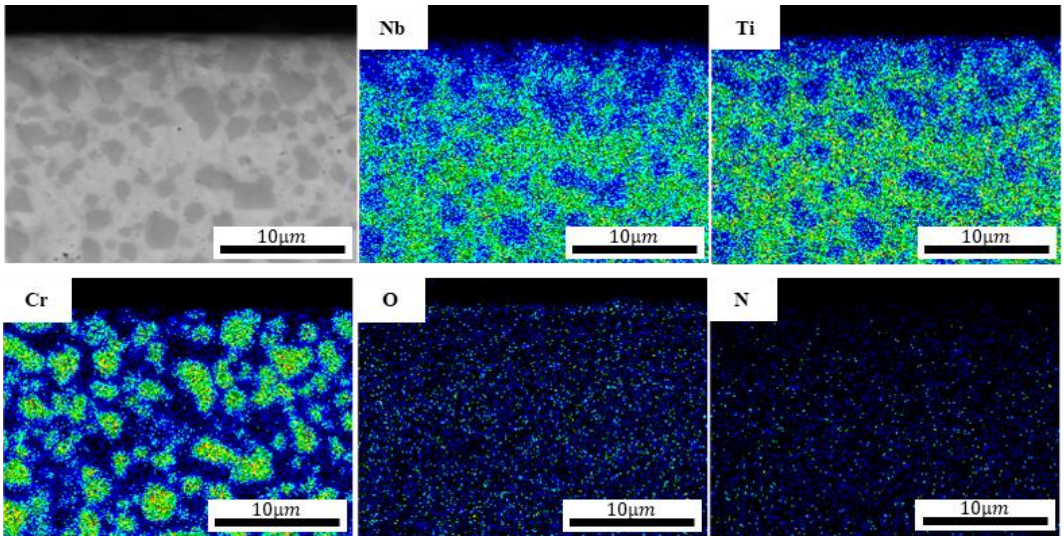

Figure 4.14 - Cross-section EDS mapping of samples tested at 1100°C/50s in air HIPed TiNbCr MPE alloy.

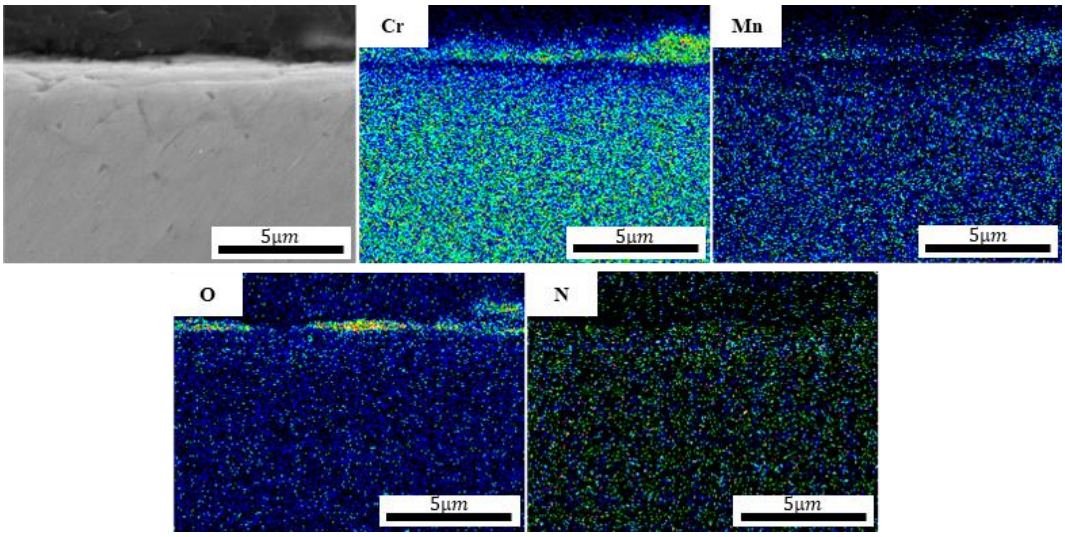

Figure 4.15 - Cross-section EDS mapping (main reacted elements) of samples tested at 1100°C/50s in air Haynes 188.

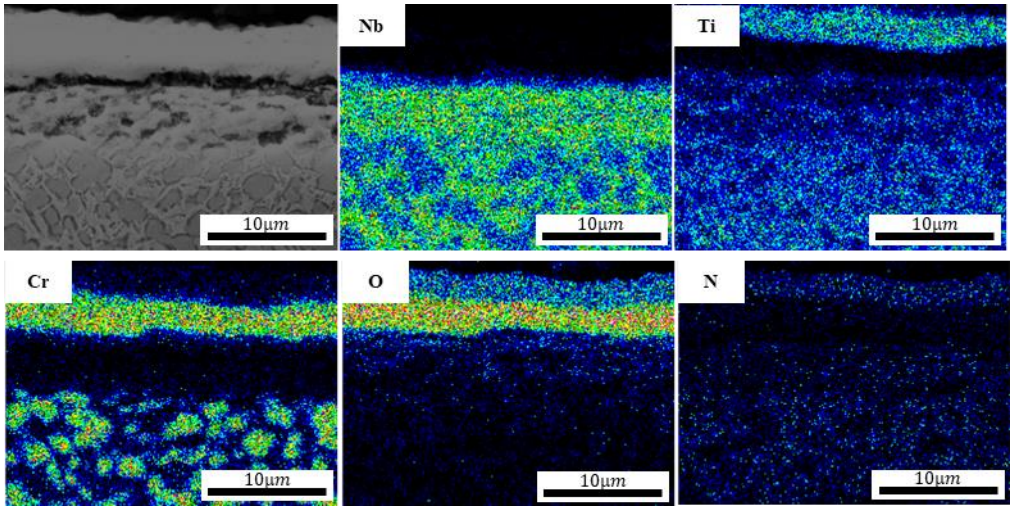

Figure 4.16 - Cross-section EDS mapping of HIPed TiNbCr MPE alloy tested at 1100°C during 1800s.

Due to the higher amount of oxygen into the BCC matrix than Laves Phase in the Table 4.6, it is suggested that BCC oxidizes first than Laves Phase and, due to the less complexity of the structure, the BCC elements diffuses first and form a complex external scale composed of multi-layer of TiO_2, Cr_2O_3 and complex oxides of Nb and Ti, observed at Figures 4.12, 4.14 and 4.16 and supported by Figure 4.11.

Butler et al. [32] evaluated the oxidation behavior of HIPed TiNbCr MPE alloy in air at 1200°C during 24h by isothermal tests and characterized the tested cross-section samples as composed of a complex out layer composed of TiO_2 which may reduce the Cr_2O_3 volatilization and offers some protection and decreases in the kinetics rate, followed by Cr_2O_3 layer and in the sequence a layer rich in Nb and Ti oxides. Additionally, the researchers highlight a formation of internal products, the formation of Cr_3Nb_3N, TiO_2 and small pockets of Nb_2O_3 in the BCC matrix and Cr_3Nb_3N, TiO_2 and Cr_2O_3.

As characterized before, the TiNbCr MPE alloy in both conditions studied presents a microstructure composed of two phases which has a limitation on the diffusion of the alloy components due to the complexity of the structure.

The stable oxide scale formation in two-phases alloys has slow-growing, is more difficult and requires higher concentrations of the more reactive alloying element than the corresponding single-phase alloy [36]. As observed by Dahshan et al. [87] for Co+$Cr_{23}C_6$ alloy oxidized in air at 900-1100°C that allowed them to note, qualitatively, the protective Cr_2O_3 formation was determined by the Cr availability and not activity, based on the equilibrium thermodynamics and Fick's first law.

According to Gesmundo and Gleeson [36], the protective scale formation in two-phase alloys is more difficult if the precipitates do not have a homogeneous distribution, as observed by Figure 4.4 for HIPed condition, and it happens if the precipitates dissolution kinetics are slow or if the kinetics of the matrix phase are high.

Wang et al. [88] highlighted that the ratio of precipitate volume fraction to size must exceed a critical value to have the exclusive formation of the solute-metal oxide on the two phase-alloy, which means that a decrease in the precipitate sizes may help to form a protective solute scale.

Extending this fact to the TiNbCr MPE alloy, which is characterized by the absence of solute, it is possible to analyze for the element Cr and the Cr_2O_3 formation. Laves phase is rich in Cr and as noted by Figures 4.3 and 4.4 and discuss in the section Microstructure characterization, the condition as-cast has this precipitate in smaller sizes distributed in the dendritic structure than the

HIPed. Therefore, the decreasing in the Laves phase precipitated may promote the Cr_2O_3 formation and consequently the smaller mass gain/area in the Figure 4.10.

Figures 4.14 and 4.16 suggest that the two phases presented in the TiNbCr MPE alloy oxidize cooperatively to form a uniform scale due to the constant alloy morphology with no phase dissolution in the areas close the surface along the exposure time and a scale composed of continuous layers in composition, a mechanism described by Gesmundo and Gleeson [36] during their studies about two-phases alloys oxidation mechanism.

Table 4.7 - Key points of anisothermal tests for TiNbCr MPE alloy. highlights the key points observed in anisothermal testing condition as discussed in this section for TiNbCr MPE alloy.

Table 4.7 - Key points of anisothermal tests for TiNbCr MPE alloy.

Testing condition	Air; exposure 18s, 30s, 50s, 180s, 1800s
Identified Oxides	TiO_2, Cr_2O_3, $NbTiO_4$, and $TiNb_2O_7$
Mechanism	Two phases oxide cooperatively
Comparison with Haynes 188	TiNbCr MPE alloy forms a non-protective external scale and takes more time to achieve the supersaturation in the surface

4.3 Oxidation Behavior: tests in air – isothermal and cyclic

The oxidation behavior of TiNbCr MPE alloy in both conditions was evaluated in air by isothermal tests and compared to the Haynes 188, as shown in Figure 4.17. It is important to highlight that the total mass gain considered in these graphs represents the combination effects of oxidation, nitridation, and spallation, as will be discussed on subsequently.

In the Figure 4.17 (a), the TiNbCr MPE alloy demonstrated similar kinetics in both studied conditions, with higher mass gain per area at lower temperatures, suggesting varying scaling mechanisms at different temperatures. Nonetheless, it exhibited consistently higher mass gains overall compared to Haynes 188. In contrast, Haynes 188 consistently exhibited an elevated mass gain per area as

the test temperature increased, Figure 4.17 (a), indicating a consistent scaling process mechanism.

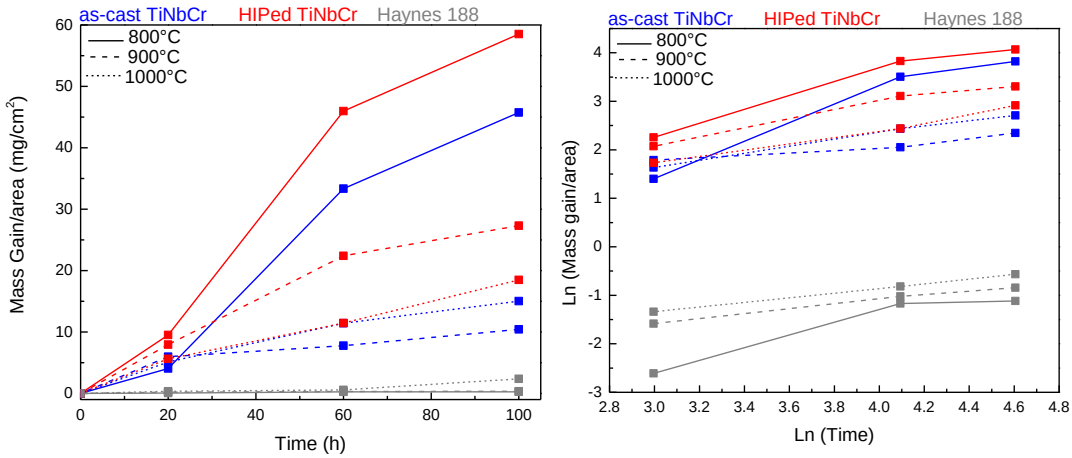

(a) (b)

Figure 16: Figure 4.17 - Mass change per area for TiNbCr MPE alloy and Haynes 188 at 800, 900 and 1000°C during isothermal oxidation in air represented in linear form (a) and ln form (b).

The general growth rate law was used to analyze the kinetics data according to Equation 9, in which ΔW is the mass gain (mg), A is the initial surface area (cm^2), k is the rate constant, t is oxidation time, as shown in the Figure 4.17 (b). The results are shown in Table 4.8, where it is possible to note that the fitting is not satisfactory for Haynes 188 at 800°C because, according to the literature, it is a parabolic behavior, as at 900 and 1000°C [89, 90] and based on n value, it is the mixed-mode behavior which involves diffusion and interface-controlled, as described by Welch et al. [33].

Based on Figure 4.17 (b) and Table 4.8, at 800°C the TiNbCr MPE alloy exhibited an approximate linear kinetics due to the time exponent close to 1. However, increasing the temperature, this exponent is between 0.5 and 1 characterizing, according to Welch et al. [33], the mixed-mode behavior. This fact suggests that the oxidation mechanism is changing with an increase in the temperature.

Table 4.8 - Reaction rate constants (k) and time exponents (n) for TiNbCr MPE alloy and Haynes 188 at 800, 900 and 1000°C.

Alloy	Temperature (°C)	n	R^2	$k\ (\frac{g}{cm^2 s^n})$
as-cast TiNbCr	800	1.07	0.95	$2.02x10^{-8}$
	900	0.83	0.93	$1.16x10^{-5}$
	1000	0.67	0.98	$2.35x10^{-6}$
HIPed TiNbCr	800	1.09	0.92	$4.78x10^{-8}$
	900	0.79	0.88	$1.11x10^{-6}$
	1000	0.62	0.99	$3.34x10^{-6}$
Haynes 188	800	0.88	0.84	$2.89x10^{-9}$
	900	0.46	0.99	$4.02x10^{-8}$
	1000	0.47	0.99	$6.47x10^{-8}$

Due to the similarity between as-cast and HIPed TiNbCr MPE surface morphology, only the as-cast surface images obtained by OM are shown in the Figure 4.18.

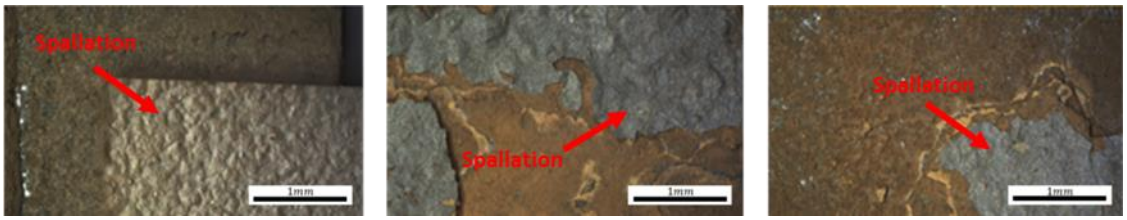

(a) (b) (c)

Figure 4.18 - Optical microscopy of as-cast TiNbCr MPE alloy samples after 100h test in air at (a) 800°C, (b) 900°C and (c) 1000°C.

Figure 4.18 highlights the presence of spallation areas in the as-cast TiNbCr MPE alloy following exposure to all tested temperatures, with more pronounced spallation observed in the sample tested at 800°C. This suggests that the protective mechanism at 800°C may be less effective compared to temperatures of 900 and 1000°C. This observation aligns with the higher mass

gain per area for the as-cast TiNbCr alloy at 800°C, as depicted in Figure 4.17 (a).

The topography sections images obtained SEM of all alloys after 100h testing at 800, 900 and 1000°C in air are shown in Figures 4.19 – 4.21 and the identification of oxides was made based on EDS analysis and supported by XRD, Figure 4.22. Due to the chemical similarity, just the XRD of condition as-cast is shown.

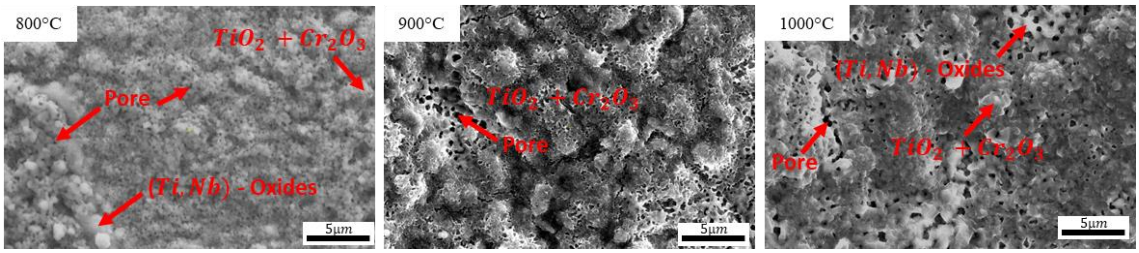

Figure 4.19 - Topography section by SEM of as-cast TiNbCr MPE alloy after 100h testing in air.

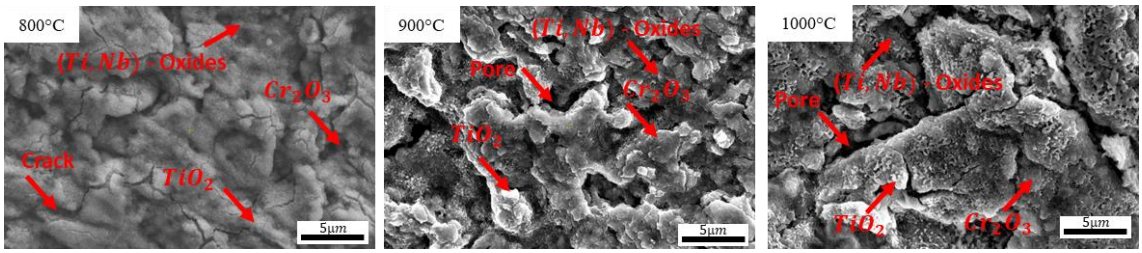

Figure 4.20 - Topography section by SEM of HIPed TiNbCr MPE alloy after 100h testing in air.

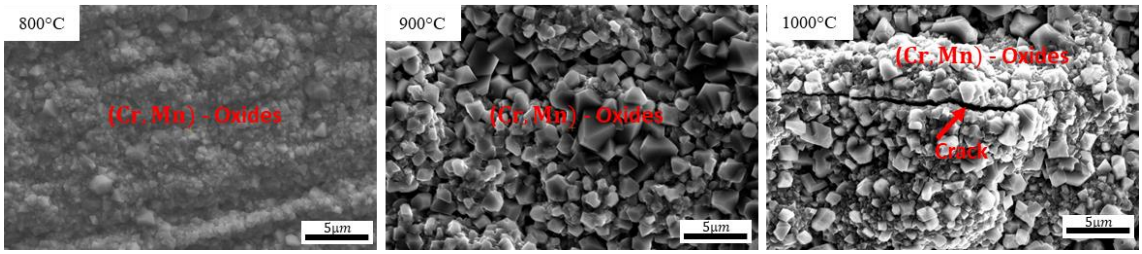

Figure 4.21 - Topography section by SEM of Haynes 188 after 100h testing in air.

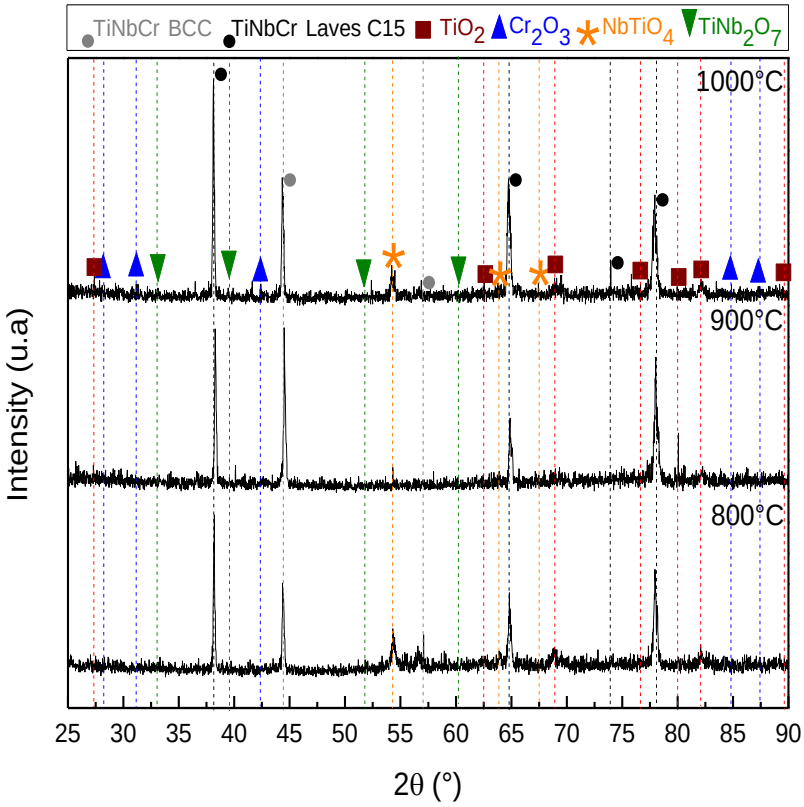

Figure 4.22 - XRD Spectra of as-cast TiNbCr MPE alloy after oxidation test in air during 100h.

Comparing the topography section of TiNbCr MPE alloy (Figures 4.19 and 4.20) with Haynes 188 (Figure 4.21), it is possible to highlight that the TiNbCr MPE alloy in both conditions forms oxides with bigger grain sizes than Haynes 188, suggesting faster growth.

Additionally, the oxide scales formed on TiNbCr MPE alloy surface exhibits higher porosity than those formed on the Haynes 188. The existence of porosity enables the entry of gas through the scale and could potentially compromise overall protection, as evidenced by the elevated weight gains depicted in Figure 4.17 (a). Moreover, escalating temperatures led to a rise in porosity levels.

Figure 4.22 highlights that increasing the temperature, the Cr_2O_3 formation is favorable, as noted in the cross-sections obtained by SEM and the oxides identification by EDS of all samples tested during 100h at 800, 900 and 1000°C in Figures 4.23 – 4.25.

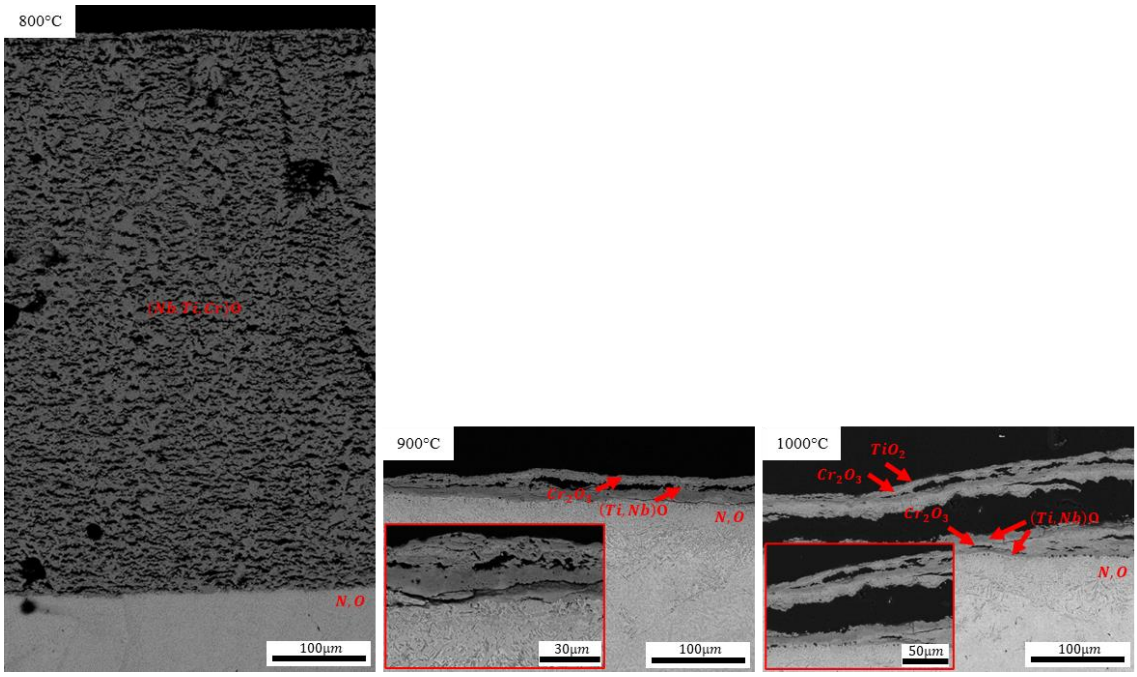

Figure 4.23 - Cross-section by SEM of as-cast TiNbCr MPE alloy after 100h testing in air.

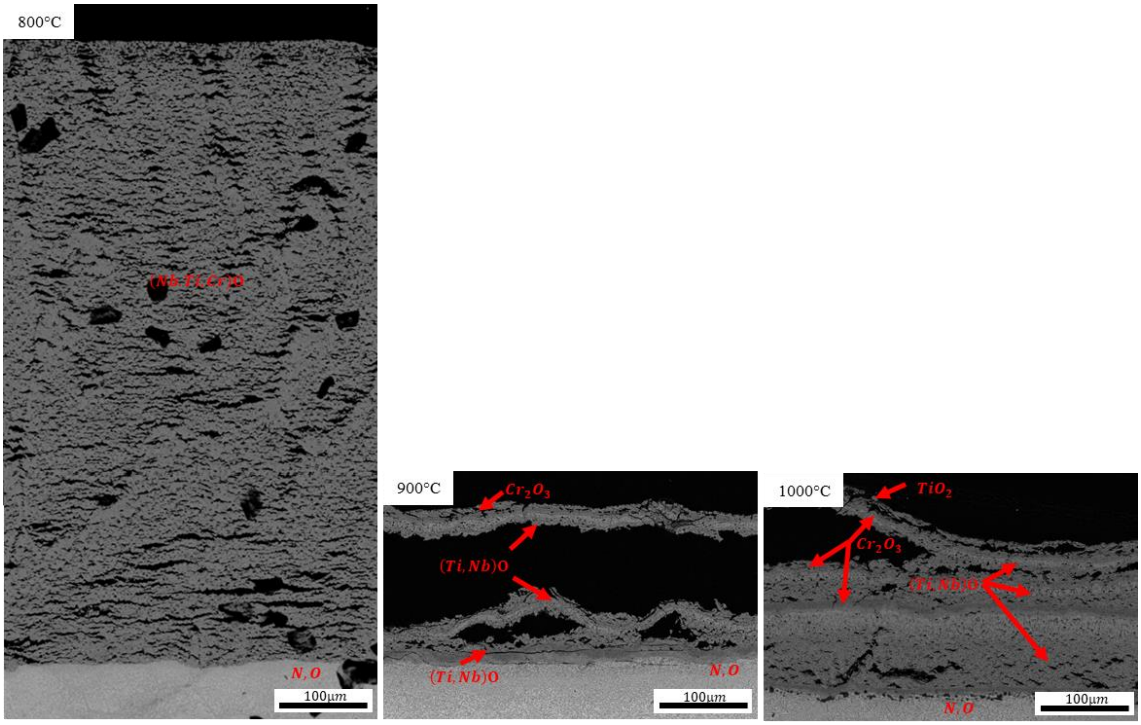

Figure 4.24 - Cross-section by SEM of HIPed TiNbCr MPE alloy after 100h testing in air.

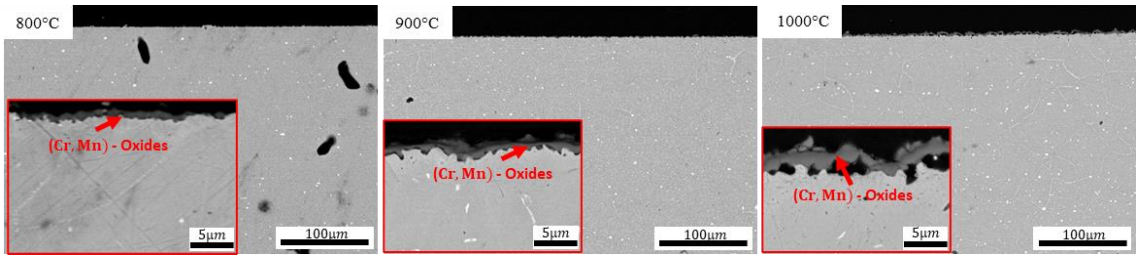

Figure 4.25 - Cross-section by SEM of Haynes 188 after 100h testing in air.

Figures 4.23 and 4.24 highlight that the TiNbCr MPE alloy develops a clear non-protective and non-adherent oxide scale across all temperatures, indicating linear kinetics despite of the processing method. The oxide layer exhibits a stratified porous morphology along with an internal reaction zone.

On the other hand, examination of Haynes 188 in Figure 4.25 reveals the formation of a thin and adherent oxide layer without any apparent internal reaction zone across all temperatures studied. This suggests a parabolic behavior, consistent even at 800°C, in line with the findings of Deodeshmukh and Herchenroeder and their colleagues [89, 90]. Although the time exponent in Table 4.8 indicates a mixed-mode behavior, this could be attributed to the limited resolution when using ln-ln plots to determine kinetic exponents.

The elements distribution through the scale/alloy after 20h hours testing at 800, 900 and 1000°C is show by Figures 4.26 – 4.28, respectively. This time testing was selected due to the increasement in time testing generates an increasement in the spallation amount, which would be impossible to characterize the elemental distribution.

Figures 4.26 – 4.28 highlight that the cross-sections of TiNbCr MPE alloy tested at 800°C is characterized by a scale composed of a mixture of Nb, Ti and Cr oxides with no defined layer, however, at 900 and 1000°C an external layer rich in Ti is formed followed by a rich Cr-oxide layer and it is intercalated with a layer rich in Ti and Nb, according to XRD, Figure 4.22, this structure should be composed of TiO_2, Cr_2O_3, and the complex oxides $NbTiO_4$ and $TiNb_2O_7$, respectively.

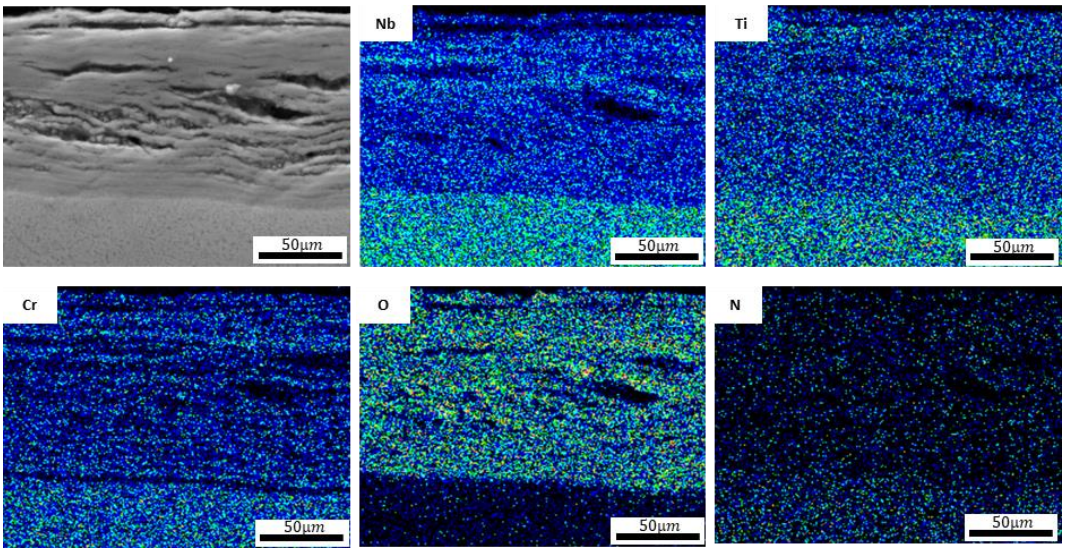

Figure 4.26 - EDS Mapping of cross-section of as-cast TiNbCr MPE alloy after 800°C isothermal test in air during 20h.

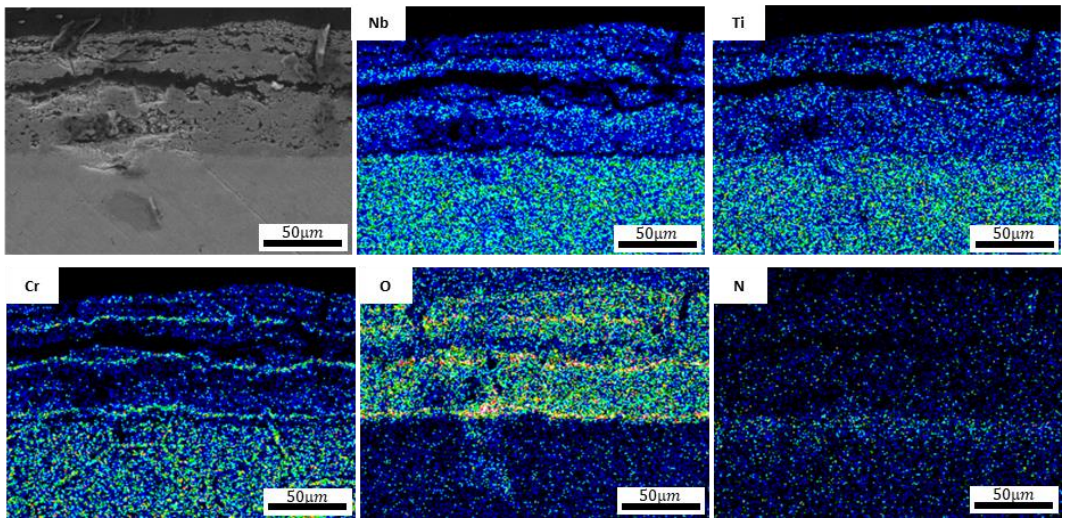

Figure 4.27 - EDS Mapping of cross-section of as-cast TiNbCr MPE alloy after 900°C isothermal test in air during 20h.

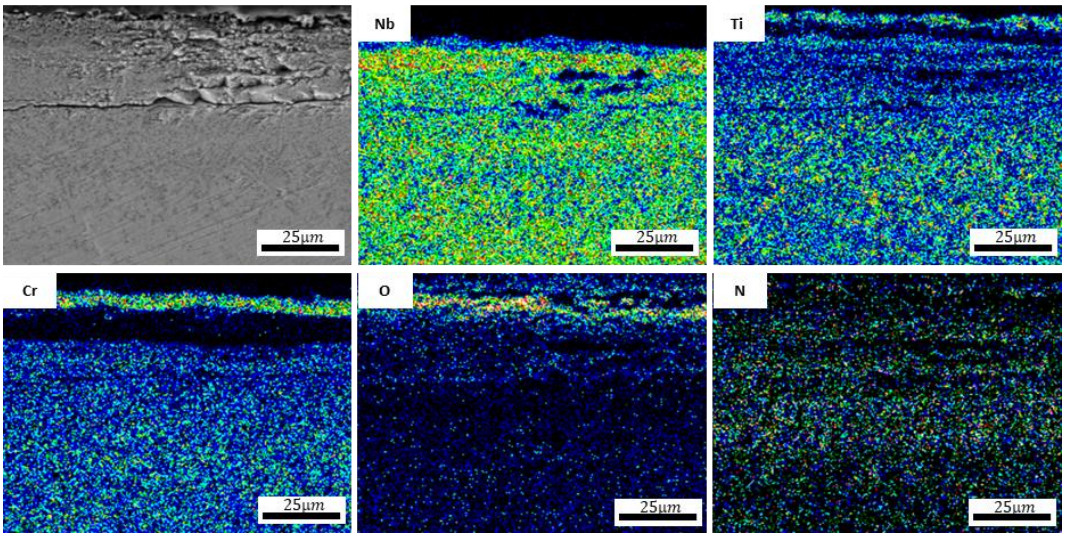

Figure 4.28 - EDS Mapping of cross-section of as-cast TiNbCr MPE alloy after 1000°C isothermal test in air during 20h.

Comparing the morphology and chemical composition of TiNbCr MPE alloy oxidized at different temperatures, Figures 4.26 – 4.28, it is suggested that oxidation occurs by different mechanism, as suggested by Table 4.8. At low temperature (800°C – stratified porous layer with no defined layer) and at high temperatures (900-1000°C – with some Cr_2O_3 layers formation).

During his studies with pure Nb crystals, Stringer [43], observed that the oxidation kinetics could be described by a linear function and the morphology shown in cross-section was composed of a stratified porous layer in the case of samples tested at temperatures equals or higher than 800°C by a supersaturation vacancy mechanism.

Throughout the oxidation process, a dense oxide scale forms and grows. However, as Nb cations diffuse outward, vacancies simultaneously diffuse inward within this scale, leading to the development of a vacancy supersaturation, particularly near the oxide/metal interface. This phenomenon arises due to challenges in efficiently transferring metal atoms or oxygen atoms across the interface. When this supersaturation reaches a critical threshold, vacancies begin to precipitate as voids, marking the removal of supersaturation. Consequently, the growth of the dense oxide recommences, and the cycle repeats itself [43].

As identified by XRD, Figure 4.22, the interaction between Nb and Ti generated the complex oxides formation, as observed by Jing et al. [44] and Gorr et al. [2] and in the case of anisothemal tests Table 4.7 - Key points of anisothermal tests for TiNbCr MPE alloy.

Additionally, Table 4.8 suggested that 800°C the TiNbCr MPE alloy exhibits a linear behavior and mixed behavior at 900 and 1000°C. However, the cross-section analysis suggested a linear dominance.

Pure Nb oxidation at 800°C is described by a linear kinetics with a rate equals to ~$9.36x10^{-6}$ g/cm^{2}s [91] and comparing this rate with the TiNbCr MPE alloy rate in both conditions, Table 4.8, it is noted that the alloy exhibits slower rate, suggesting that the formation of Nb and Ti complex oxides is more protective than pure Nb oxides, as reported by Gorr et al. [21] and the authors justified it as the Nb-Ti complex oxides exhibit smaller density of defects than pure Nb oxides.

As discussed in the section Oxidation Behavior: Early-stages, a decrease in the precipitate sizes may help to form a protective solute scale [88]. The condition as-cast presents Laves phase in smaller sizes distribution in the dendritic structure than the HIPed, so the Cr_2O_3 formation is promoted and consequently the smaller mass gain/area in the Figure 4.17 and slower kinetics, Table 4.8, are observed.

Figures 4.27 and 4.28 highlight that increasing temperature, the Cr_2O_3 layers in the external scale of TiNbCr MPE alloy is formed and it is covered by TiO_2 layer, as observed in anisothermal tests at 1100°C, Figure 4.16, and as mentioned before this configuration offer some protection [32, 52, 87].

Table 4.8 suggest that increasing temperature the kinetics trend to be parabolic and it may happen due to the Cr_2O_3 domination in the process, which exhibits parabolic kinetics characterized by a protective and adherent oxide scale [48, 52, 92, 93]. As reported a parabolic behavior of TiNbCr MPE alloy at high temperature by Butler et al. [32] when tested the alloy in HIPed condition at 1200°C in air up to 24h and also by Welch et al. [33] for alloys of the system TaTiCr.

Considering that the oxidation resistance of the TiNbCr MPE alloy relies on Cr oxidation, it is hypothesized that the presence of a thinner size distribution

of Laves phase in the as-cast alloy compared to the HIPed promotes the formation of Cr_2O_3 to a greater extent on the former. This, in turn, leads to slower oxidation kinetics, as depicted in the Table 4.8.

More detailed EDS compositional analyses are presented in Figures 4.29 and 4.30, and Tables 4.9 and 4.10. At 800°C, Figure 4.29, three distinct regions were delineated: A - external, B - intermediate, and C - interface between the scale and metal surface. Within these regions, three specific areas were selected, and their average compositions are detailed in Table 4.9. As depicted in Figure 4.29, the scale exhibits a heterogeneous composition, comprising a blend of Nb, Ti, and Cr oxides without distinct layers.

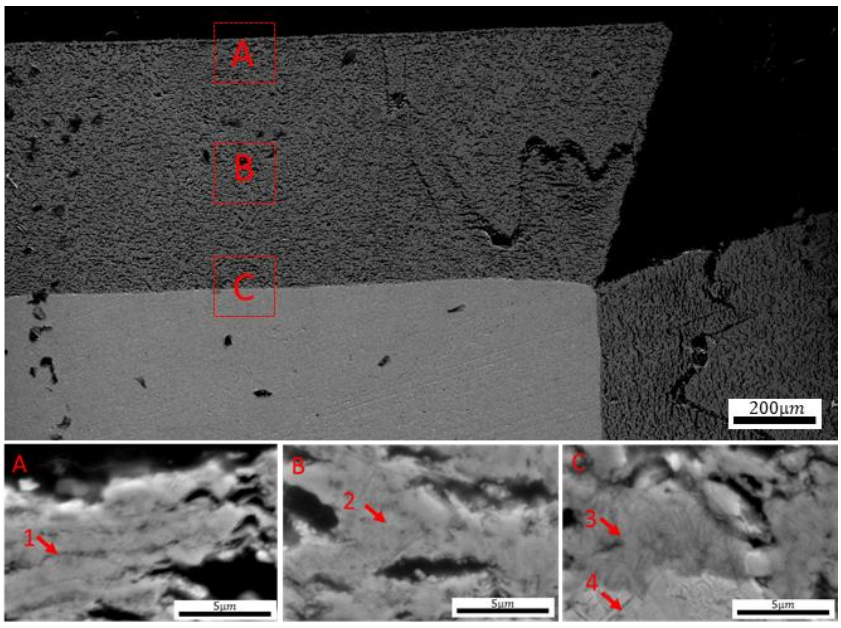

Figure 4.29 - SEM of cross-section of HIPed TiNbCr MPE alloy after 800°C isothermal test in air during 100h with EDS areas shown in numbers.

Table 4.9 - EDS analysis results for areas shown in Figure 4.29.

Composition at. %	Cr	Nb	Ti	N	O
1	9.3 ± 1.7	9.5 ± 1.7	11.5 ± 1.2	0.00 ± 0.00	69.7 ± 2.3
2	8.3 ± 3.8	10.5 ± 1.1	11.9 ± 1.6	0.00 ± 0.00	69.4 ± 0.8
3	8.8 ± 2.9	10.7 ± 2.3	10.0 ± 2.4	0.00 ± 0.00	70.5 ± 1.8
4	3.3 ± 2.8	23.9 ± 1.7	24.9 ± 1.4	25.8 ± 3.8	22.1 ± 9.7

Furthermore, the presence of an internal reaction zone is illustrated in Figure 4.30, for TiNbCr tested at 900°C. As highlighted in the Table 4.10, this region contains both nitrides and oxides. The Laves phase comprises oxides (indicated at point 2), while its boundary is predominantly N-rich (indicated at point 1). On the other hand, the BCC phase of the alloy exhibits enrichment in oxygen, nitrogen, Nb, and Ti (identified at point 3), along with some precipitates containing high concentrations of these elements (identified at point 4).

Butler et al. [32] described that TiNbCr MPE alloy processed by HIP and oxidized at 1200°C in air during 8h exhibited internal reaction zone composed of oxides and nitrates. According to their study, while the BCC matrix favorable the formation of Cr_3Nb_3N, TiO_2, small pockets of Nb_2O_3 and highly faceted TiN precipitates, Laves phase forms Cr_3Nb_3N, TiO_2 and Cr_2O_3.

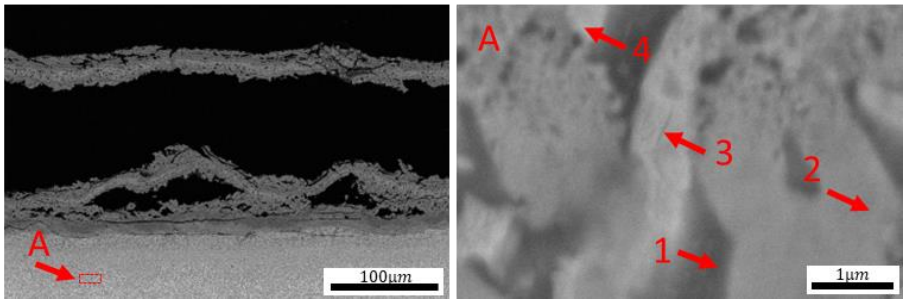

Figure 4.30 - SEM of cross-section of HIPed TiNbCr MPE alloy after 900°C isothermal test in air during 100h with EDS areas shown in numbers.

Table 4.10 - EDS analysis results for areas shown in Figure 4.30.

Composition at. %	Cr	Nb	Ti	N	O
1	38.2 ± 2.3	19.5 ± 2.0	18.2 ± 2.1	15.9 ± 1.0	8.3 ± 1.3
2	46.3 ± 2.9	15.7 ± 1.4	17.3 ± 1.9	3.0 ± 0.9	17.7 ± 1.3
3	12.7 ± 1.1	28.5 ± 2.0	20.8 ± 2.2	20.4 ± 2.1	17.6 ± 2.4
4	1.8 ± 0.9	20.9 ± 2.1	20.3 ± 1.8	42.2 ± 2.5	14.9 ± 1.2

Through EDS analysis, the infiltration of oxygen and nitrogen leading to the formation of the internal reaction zone (IRZ) was determined. All tested conditions resulted in the formation of an IRZ, and their kinetics are compared in

Figure 4.31. A rise in exposure temperature corresponded to an increase in IRZ depth, with samples exhibiting smaller IRZ depths. Furthermore, Figure 4.31 illustrates that the IRZ depth in the HIPed samples consistently exceeds that of the as-cast samples, indicating the adverse effects of the Laves-phase size, as discussed.

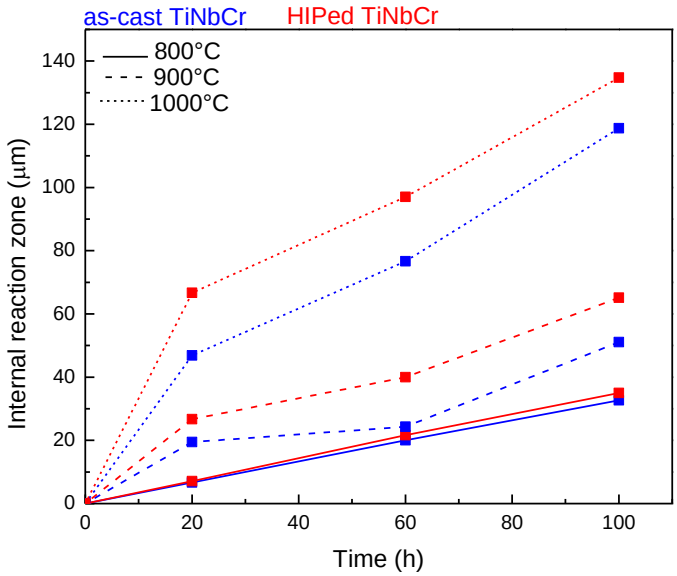

Figure 4.31 - Comparison based on Cross-Section SEM of Internal reaction zone extension.

Figure 4.32 shows the mass gain per area in function of the number of cycles for HIPed TiNbCr MPE alloy tested at 800 and 900°C. Analyzing Figure 4.32 (a), it is possible to observe that after 15 cycles at 800°C, the amount of spallation increases, a linear kinetics can be fitted until this point with a constant $k_l = 1.38x10^{-7}\ \frac{g}{cm^2 s}$.

Aimed to evaluate the spallation effect, at 900°C the spallation was collected, Figure 4.32 (b), a linear kinetics can also be fitted, with a constant equal to $7.7x10^{-8}\ \frac{g}{cm^2 s}$, in both temperatures fitting the R^2 was equals to 0.99.

The 900°C rate constant obtained from the cyclic tests is similar to the linear rate constant obtained from the 900°C isothermal test Table 4.8. This indicates that although the scale was fairly tenacious, it remained ineffective in providing protection due to its linear growth rate.

Additionally, it's crucial to emphasize that while the kinetics values ostensibly depict the behavior, aligning with other analyses, the occurrence of spallation in the TiNbCr MPE alloy post each test compromises the accuracy of the kinetics analysis. Consequently, the derived values may not be entirely precise.

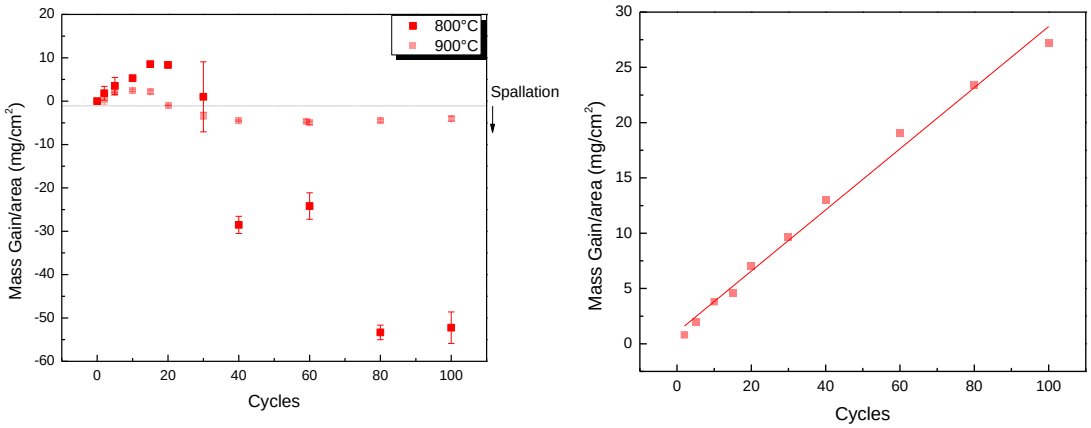

(a) (b)

Figure 4.32 - Mass gain normalized by initial surface area in function of number of cycles for HIPed TiNbCr MPE alloy tested at 800 and 900°C. (a) mass gain of sample with no collected spallation and (b) mass gain of samples plus collected spallation.

The representative topography and cross-section (SEM) of samples tested at 800 and 900°C by cyclic test after 100 cycles are shown in Figures 4.33 and 4.34, which are possible to note a similar behavior to samples tested isothermally a stratified porous layer formation and it is with non-defined layer at 800°C and Cr_2O_3 layer covered by TiO_2 and Nb-Ti complex oxides.

Additionally, comparing Figures 4.31 and 4.34, it is noted that in both temperatures 800 and 900°C the internal reaction zone thickness for samples tested isothermally and cyclic have close values, suggesting the non-protection scale formation, even increasing the spallation amount due to the cycles, as discussed previously.

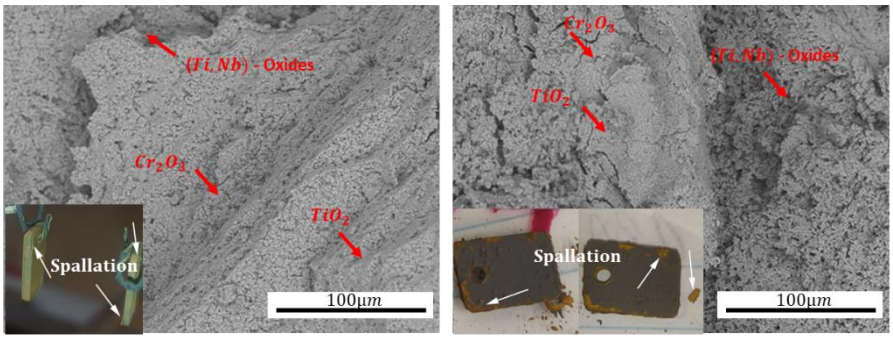

(a) (b)

Figure 4.33 - Topography section of HIPed TiNbCr MPE alloy samples test in air after 100 cycles at (a) 800°C and (b) 900°C.

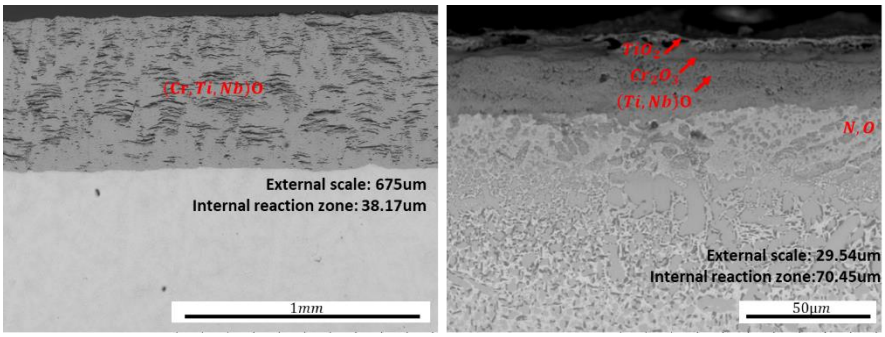

(a) (b)

Figure 4.34 - Cross-section of HIPed TiNbCr MPE alloy samples test in air after 100 cycles at (a) 800°C and (b) 900°C.

Table 4.11 - Key points of isothermal tests for TiNbCr MPE alloy. highlights the key points observed in isothermal testing condition as discussed in this section for TiNbCr MPE alloy in both conditions and Table 4.11 - Key points of isothermal tests for TiNbCr MPE alloy. for cyclic test. Comparing both condition of tests, it is notable the similarity between them, as identified oxides, mechanism, kinetics and internal reaction extension, supporting the observation of the non-protective scaling process.

Table 4.11 - Key points of isothermal tests for TiNbCr MPE alloy.

Testing condition	Air; 800, 900 and 1000°C; 20, 60 and 100h
Identified Oxides	TiO_2, Cr_2O_3, $NbTiO_4$, and $TiNb_2O_7$
Mechanism	Vacancy supersaturation development, which generated a stratified porous layer morphology
Kinetics	Linear
Time exponent and reaction rate constant (g/cm^2s^n)	as-cast: $800°C\ n = 1.07\ k = 2.02x10^{-8}$ $900°C\ n = 0.83\ k = 1.16x10^{-5}$ $1000°C\ n = 0.67\ k = 2.35x10^{-6}$ HIPed: $800°C\ n = 1.09\ k = 4.78x10^{-8}$ $900°C\ n = 0.83\ k = 1.11x10^{-6}$ $1000°C\ n = 0.67\ k = 3.34x10^{-6}$
Internal reaction zone extension after 100h-testing (µm)	as-cast: $800°C$ 31.61 $900°C$ 50.37 $1000°C$ 118.45 HIPed: $800°C$ 34.43 $900°C$ 64.98 $1000°C$ 134.19
Comparison with Haynes 188	TiNbCr MPE alloy forms a non-protective external scale with more defects, higher values of mass gain/area, and faster kinetics

Table 4.12 - Key points of cyclic tests for HIPed TiNbCr MPE alloy.

Testing condition	Air; 800 and 900°C 100 cycles of 1h each
Identified Oxides	TiO_2, Cr_2O_3, $NbTiO_4$, and $TiNb_2O_7$
Mechanism	Vacancy supersaturation development, which generated a stratified porous layer morphology
Kinetics	Linear
Time exponent and reaction rate constant (g/cm^2s^n) (100 cycles)	HIPed: $900°C\ n{\sim}1\ k = 7.7x10^{-8}$
Internal reaction zone extension after 100 cycles (µm)	HIPed: $800°C$ 38.17 $900°C$ 70.45

4.4 Oxidation Behavior: tests in Oxygen

Aimed to isolate the oxygen effect in the degradation behavior, oxidation tests were performed at TGA during 100h in a gas mixture composed of Ar+21%

vol. O_2 at 700, 800, 900 and 1000°C, and the mass gain per area is shown in Figure 4.35 (a) and to evaluate the passivation time the derivate in function of time was applied, as shown in Figure 4.35 (b) and (c), where is highlighted the longest time of passivation after 8h for TiNbCr MPE alloy.

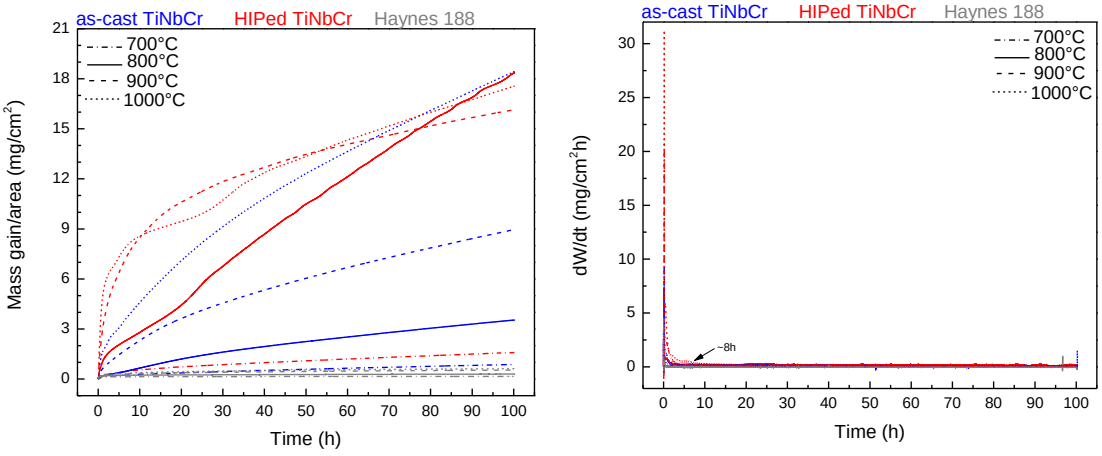

(a) (b)

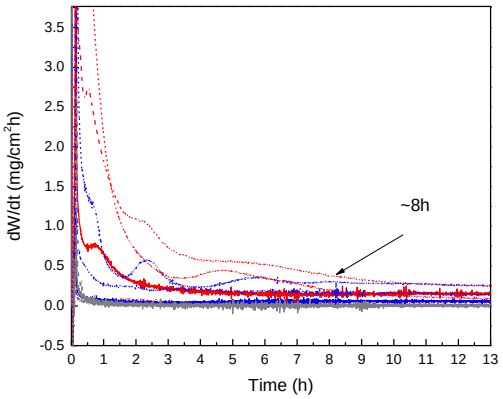

(c)

Figure 4.35 - TGA tests during 100h results: (a) mass gain/area in function of time and (b) derivate of the mass gain per area in function of time (c) detailed area of the derivate of the mass gain per area in function of time plot.

Applying the same fitting that isothermal tests in air, Equation 9, and calculating the parameters n and k from 8 to 100h, the results are shown in Table 4.13. Similar results between oxidation in air and oxygen were obtained for Haynes 188, Tables 4.8 and 4.13. The TiNbCr MPE alloy exhibited the same trend to parabolic kinetics at high temperatures, 900-1000°C, however at 700°C

a parabolic trend is observed in the Table 4.13, as observed by Stringer [43] for Nb crystals oxidation at low temperature, lower than 750°C.

This fact is in agreement with the hypothesis formulated and discussed for samples tested in air when the scaling mechanism was compared to the pure Nb oxidation, which generate a stratified porous layer due to the supersaturation vacancy mechanism.

Comparing Tables 4.8 and 4.13, it is noted that the addition of N in the environment increases the kinetics of the reaction, highlighting how more detrimental is the environment with N than that one with just oxygen [94].

Table 4.13 - Reaction rate constants (k) and time exponents (n) for TiNbCr MPE alloy and Haynes 188 at 700, 800, 900 and 1000°C.

Alloy	Temperature (°C)	n	R^2	$k\ (\frac{g}{cm^2 s^n})$
as-cast TiNbCr	700	0.51	0.99	$1.11x10^{-7}$
	800	1.08	0.99	$3.93x10^{-9}$
	900	0.70	0.99	$8.89x10^{-8}$
	1000	0.59	0.99	$1.14x10^{-7}$
HIPed TiNbCr	700	0.46	0.99	$1.01x10^{-7}$
	800	1.18	0.99	$3.18x10^{-9}$
	900	0.71	0.97	$2.44x10^{-10}$
	1000	0.63	0.99	$3.27x10^{-10}$
Haynes 188	700	0.77	0.98	$2.92x10^{-13}$
	800	0.81	0.99	$5.84x10^{-10}$
	900	0.47	0.99	$2.24x10^{-8}$
	1000	0.56	0.98	$8.97x10^{-12}$

The topography section of each alloy tested during 100h in oxygen is shown in Figures 4.36 – 4.38, where it is possible highlight the same observations that in oxidation in air: the oxides grains formed in the TiNbCr MPE alloy surface have bigger sizes than in the Haynes 188, suggesting faster kinetics, as discussed in the section of Oxidation Behavior: tests in air – isothermal and cyclic.

Additionally, it is noted in the case of TiNbCr MPE alloy, the layer composed of TiO_2 and Cr_2O_3 spall of the layer composed of the mixture of Nb and Ti oxides, as in the tested conducted in air.

The XRD of the TiNbCr MPE alloy is shown in the Figure 4.39. Due to the similarity between the as-cast and HIPed condition, only the first one is highlighted.

Comparing Figures 4.22 and 4.39 it is reported that the same oxides species were identified in testes conducted in air and oxygen, respectively. This observation is supported by Butler et al. [32] when they studied the oxidation behavior of HIPed TiNbCr MPE alloy in air at 1200°C up to 24h.

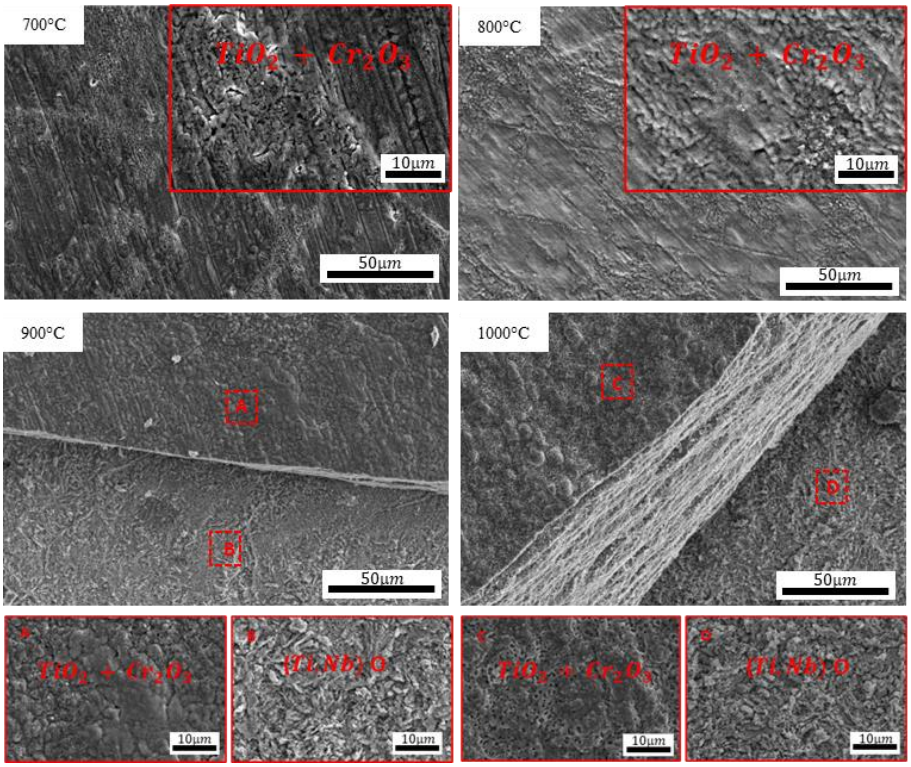

Figure 4.36 - Topography section by SEM of as-cast TiNbCr MPE alloy after 100h testing in oxygen.

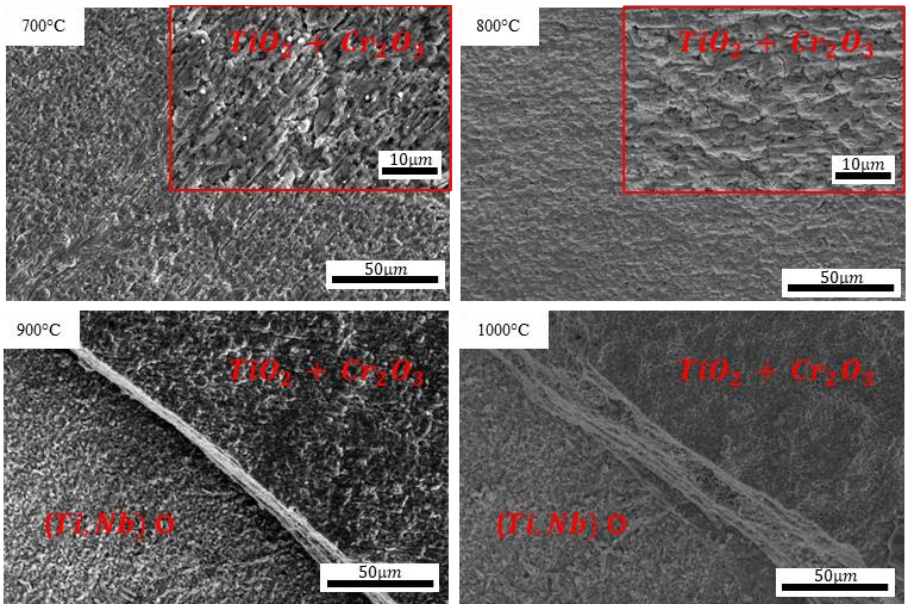

Figure 4.37 - Topography section by SEM of HIPed TiNbCr MPE alloy after 100h testing in oxygen.

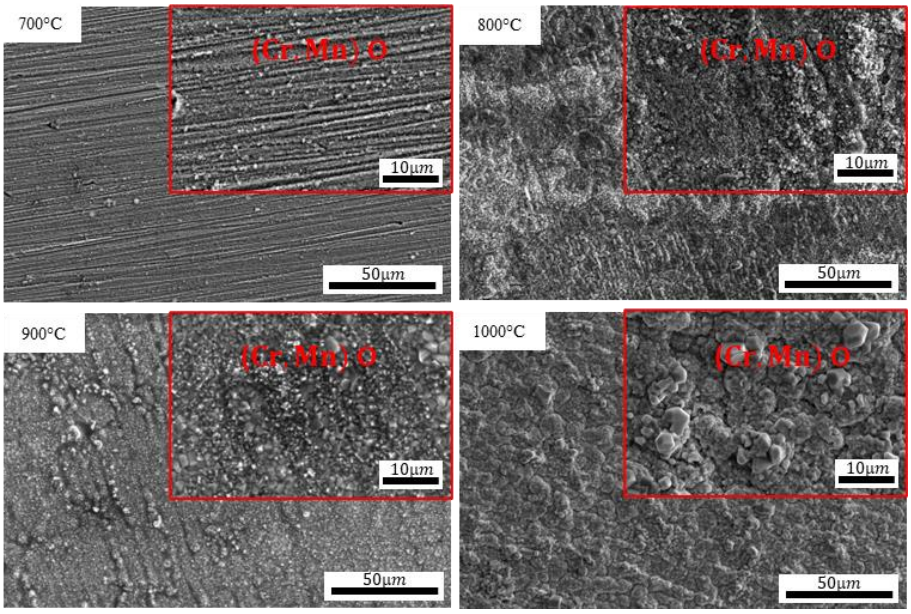

Figure 4.38 - Topography section by SEM of Haynes 188 after 100h testing in oxygen.

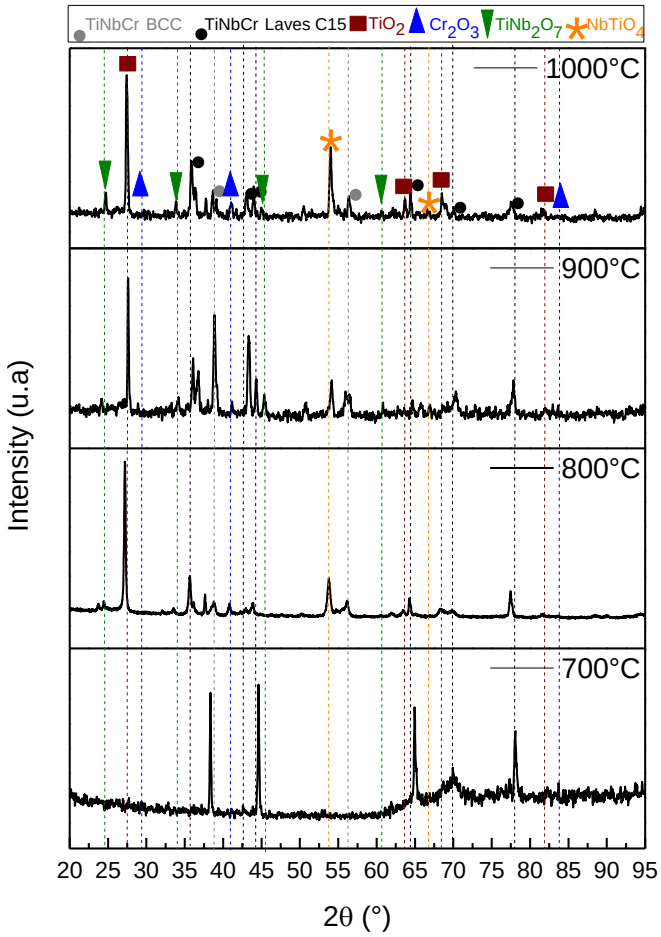

Figure 4.39 - XRD Spectra of as-cast TiNbCr MPE alloy after oxidation test in oxygen during 100h.

Figures 4.40 - 4.42 show the cross-section of as-cast and HIPed TiNbCr MPE alloy and Haynes 188 after 100h-testing in oxygen, and an EDS analysis of the internal reaction zone is shown in the Table 4.14.

Analyzing Figures 4.40 and 4.41 it is possible to note that at low temperatures two internal reaction zones occur, the first one is composed of thinner oxides rich in Ti and Nb in the BCC matrix and the second is characterized by the intensification of the oxides in the Laves phase, rich in Ti and Cr, as mentioned in the sections Oxidation Behavior: Early-stages and Oxidation Behavior: tests in air – isothermal and cyclic.

Based on results shown in the section Oxidation Behavior: Early-stages where the TiNbCr MPE alloy takes more time to achieve the supersaturation and

about the two-phase alloy oxidation behavior mentioned in the same section, Figures 4.40 and 4.41, highlight the same trend. Which means that due to the complexity of Laves phase, elements diffuse easier from the BCC matrix, generating thinner precipitates.

However, increasing the temperature, the oxidation kinetics increases, and as BCC elements diffuse faster, just the second zone is observed, as observed by Butler et al. [32] and Gorr et al. [2].

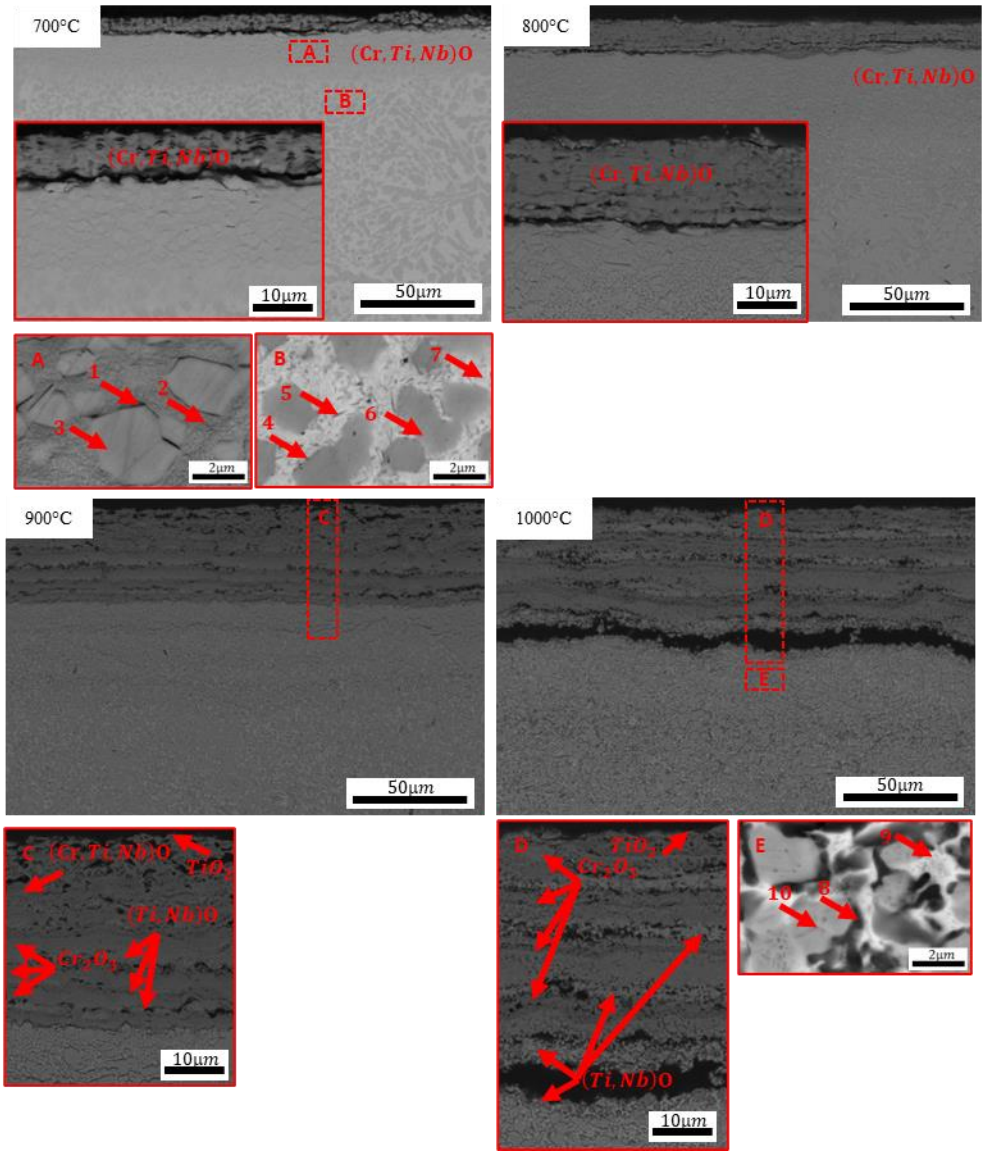

Figure 4.40 - Cross-section by SEM of as-cast TiNbCr MPE alloy after 100h testing in oxygen.

Table 4.14 - EDS analysis results for areas shown in Figure 4.40.

Composition at.%	Cr	Nb	Ti	O
1	14.6 ± 0.9	21.2 ± 1.6	25.4 ± 1.2	38.8 ± 2.2
2	21.2 ± 1.4	29.8 ± 2.1	28.8 ± 1.8	20.2 ± 1.1
3	48.1 ± 3.0	23.2 ± 1.9	20.5 ± 2.1	8.2 ± 0.7
4	20.5 ± 1.9	32.9 ± 3.0	33.3 ± 2.2	13.2 ± 0.9
5	9.5 ± 1.1	36.1 ± 3.1	40.2 ± 2.6	14.1 ± 1.2
6	57.4 ± 3.3	20.2 ± 1.9	17.5 ± 1.4	4.8 ± 0.7
7	15.6 ± 1.1	34.7 ± 3.2	38.0 ± 3.1	11.6 ± 1.1
8	17.8 ± 1.8	34.9 ± 3.0	35.1 ± 2.1	12.2 ± 1.3
9	7.0 ± 1.1	37.4 ± 3.3	42.2 ± 3.1	13.4 ± 1.4
10	51.4 ± 3.3	17.3 ± 1.5	20.3 ± 1.3	10.9 ± 1.3

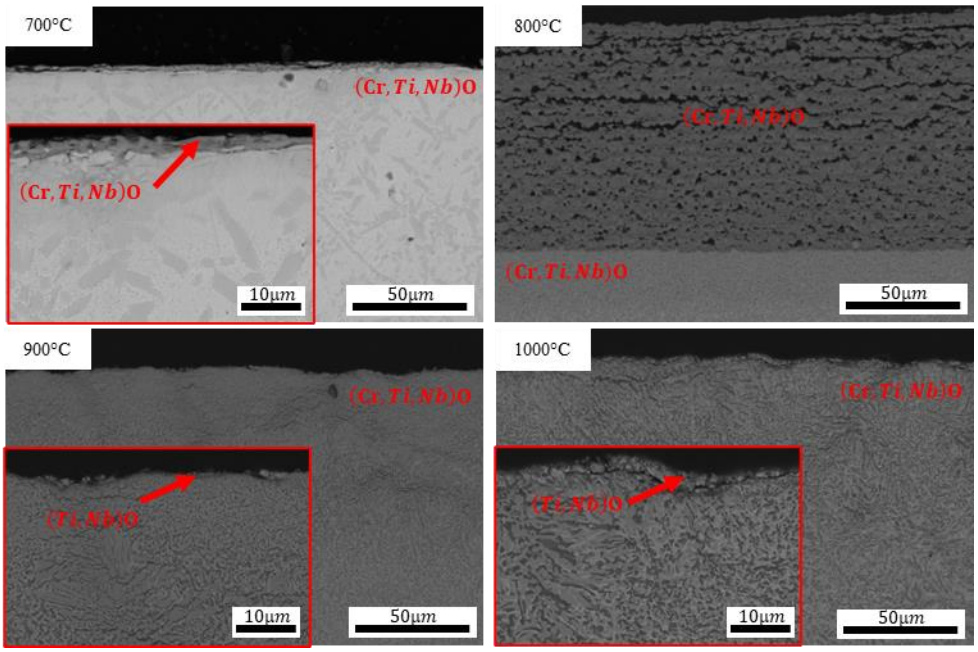

Figure 4.41 - Cross-section by SEM of HIPed TiNbCr MPE alloy after 100h testing in oxygen.

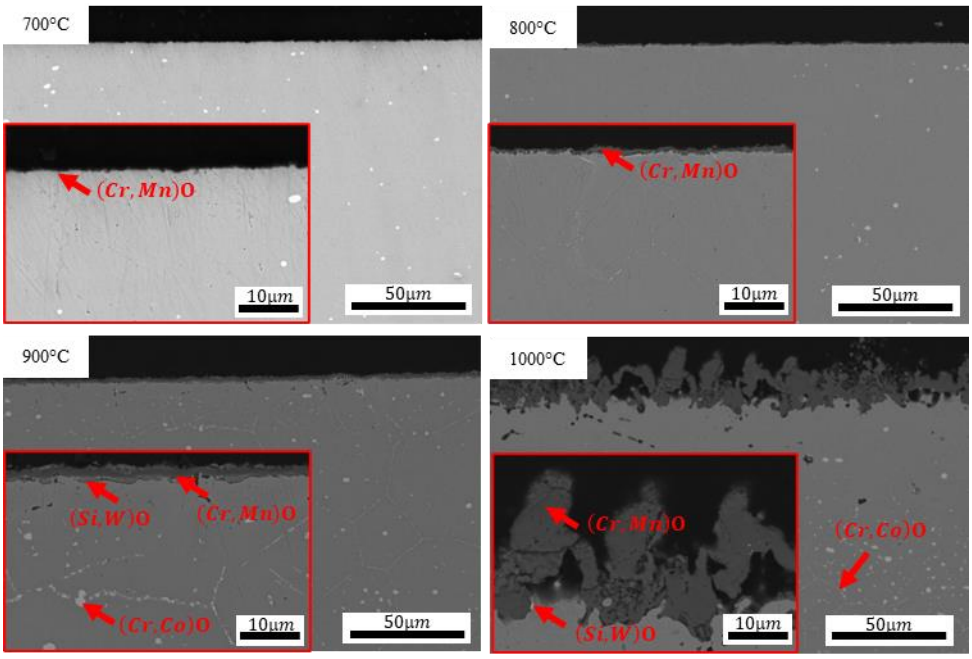

Figure 4.42 - Cross-section by SEM of Haynes 188 after 100h testing in oxygen.

Figures 4.43 – 4.46 show the chemical distribution of the elements after 100h testing in oxygen. Again, due to the similarity between as-cast and HIPed TiNbCr MPE alloy, only the as-cast condition is highlighted.

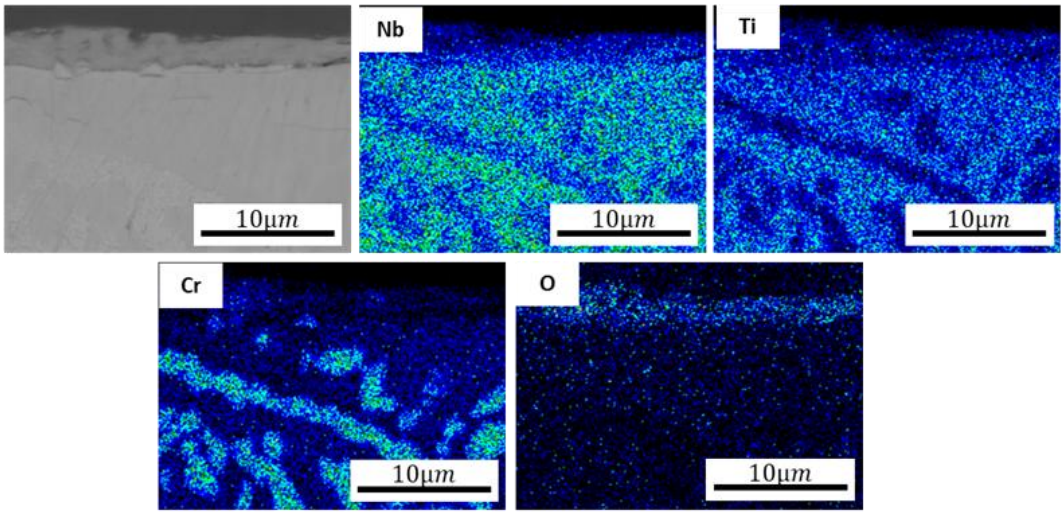

Figure 4.43 - EDS Mapping of cross-section of as-cast TiNbCr MPE alloy after 700°C isothermal test in oxygen during 100h.

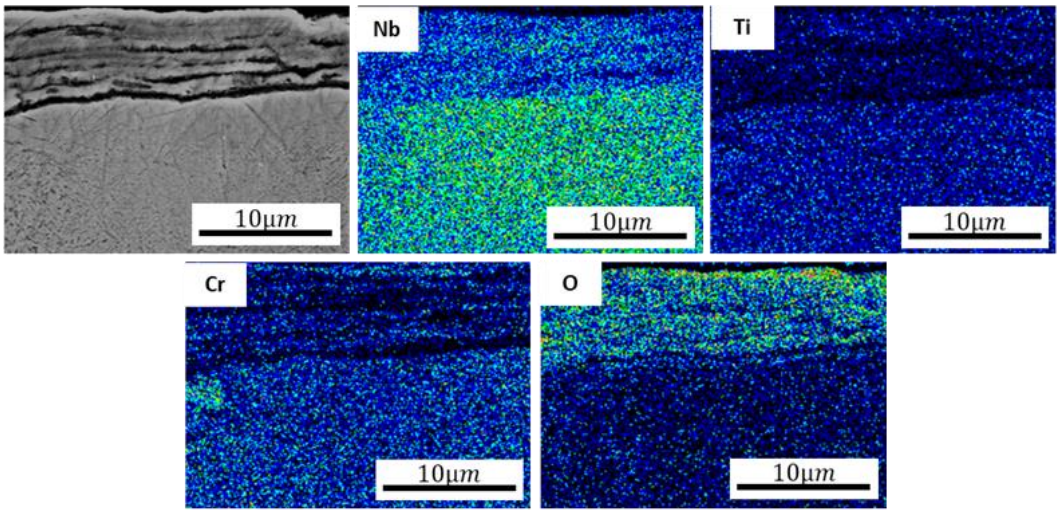

Figure 4.44 - EDS Mapping of cross-section of as-cast TiNbCr MPE alloy after 800°C isothermal test in oxygen during 100h.

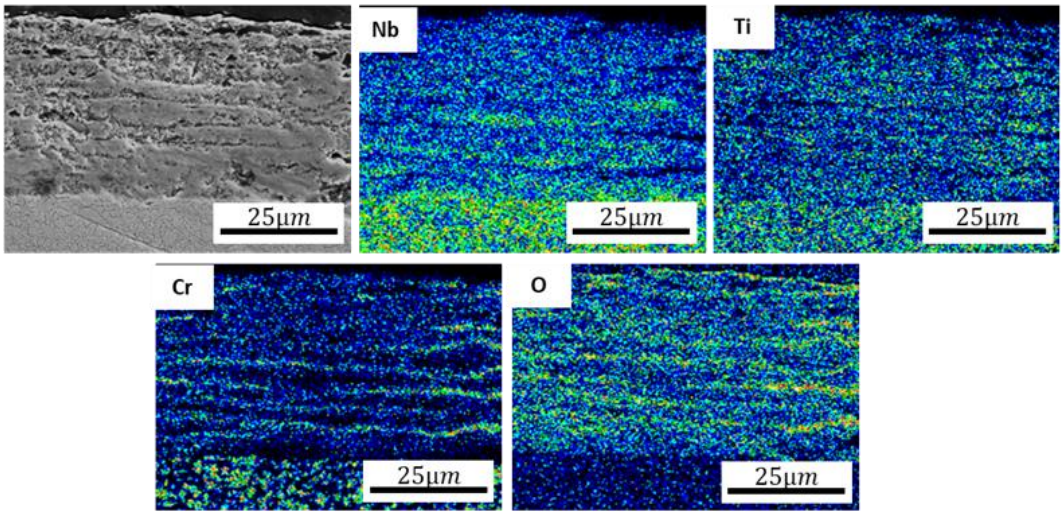

Figure 4.45 - EDS Mapping of cross-section of as-cast TiNbCr MPE alloy after 900°C isothermal test in oxygen during 100h.

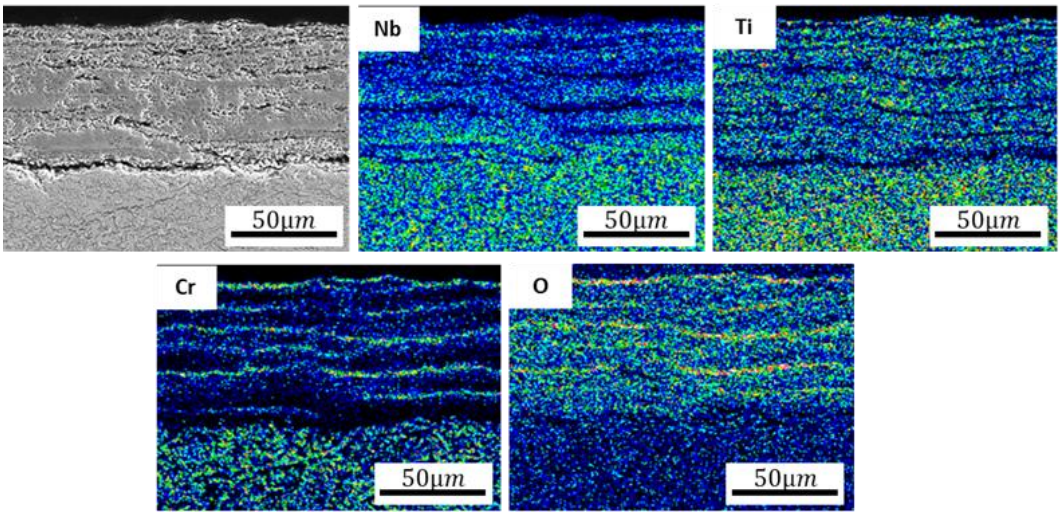

Figure 4.46 - EDS Mapping of cross-section of as-cast TiNbCr MPE alloy after 1000°C isothermal test in oxygen during 100h.

Between 800 and 1000°C, the same morphology of the oxide scale observed in samples tested in air is emphasized: a stratified porous layer formation; at 800°C a scale composed of a mixture of oxides rich in Nb, Ti and Cr with no defined layer formation and at 900 Cr-rich oxides starts to form but non-continuous and at 1000°C it starts to be continuous.

As mentioned before, in the section Oxidation Behavior: tests in air – isothermal and cyclic, it is suggested that the behavior at low temperature is dominate by Nb oxidation and the mechanism proposed by Stringer is observed [43].

Looking to Figure 4.43, it is possible to note that at 700°C the oxide scale is not stratified like other temperatures, instead of it, a dense layer is formed, supporting the mechanism proposed by Stringer [43] in the case of pure Nb oxidation.

During the oxidation process, a dense oxide layer is formed at low temperatures, which is more protective and a decrease in kinetic rate is observed and suggested by the time exponent in the Table 4.13. However, the diffusion outward of the elements and the vacancy inward diffusion, generates a supersaturation and voids, and this cyclic process, with the increasing in the temperature, a stratified porous layer is formed, which increases the kinetic rate [43].

Additionally, the slower kinetics observed for condition as-cast is explained by the behavior of two-phase alloy oxidation studied by Gesmundo and Gleeson [36] and discussed before.

However, as highlighted in the section Oxidation Behavior: tests in air – isothermal and cyclic, at 900°C the Cr-rich oxide, which according to XRD, Figure 4.39, should be Cr_2O_3 starts to compete due to the formation of layers rich in this oxide.

Due to the cross-section of tested TiNbCr MPE alloy in both conditions Figures 4.40 and 4.41 characterize a non-protective oxide scale formation due to the high density of defects, non-adherence and internal oxidation zone, a linear behavior is suggested [31, 60].

Comparing the extension of the internal reaction zone of samples tested in air, Figure 4.47, it is observed that the addition of N in the environment reduce the internal reaction zone.

Table 4.15 highlights the key points observed in isothermal testing condition in oxygen as discussed in this section for TiNbCr MPE alloy in both conditions.

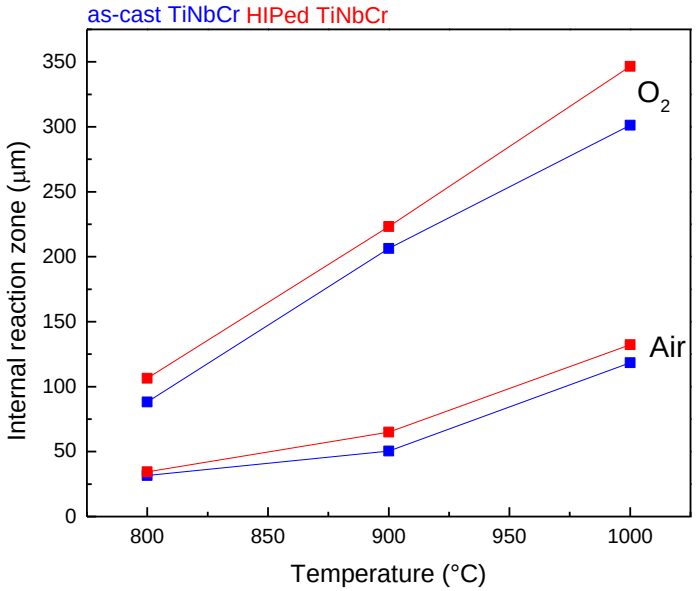

Figure 4.47 - Comparison based on Cross-Section SEM of Internal reaction zone extension.

Table 4.15 - Key points of isothermal tests for TiNbCr MPE alloy.

Testing condition	Ar+21% O_2; 700, 800, 900 and 1000°C; 100h
Identified Oxides	TiO_2, Cr_2O_3, $NbTiO_4$, and $TiNb_2O_7$
Mechanism	Vacancy supersaturation development, which generated a stratified porous layer morphology
Kinetics	Linear
Time exponent and reaction rate constant (g/cm^2s^n)	as-cast: $700°C\ n = 0.51\ k = 1.11x10^{-7}$ $800°C\ n = 1.08\ k = 3.93x10^{-9}$ $900°C\ n = 0.70\ k = 8.89x10^{-8}$ $1000°C\ n = 0.59\ k = 1.14x10^{-7}$ HIPed: $700°C\ n = 0.46\ k = 1.01x10^{-7}$ $800°C\ n = 1.18\ k = 3.18x10^{-9}$ $900°C\ n = 0.71\ k = 2.44x10^{-10}$ $1000°C\ n = 0.63\ k = 3.27x10^{-10}$
Comparison with Haynes 188	TiNbCr MPE alloy forms a non-protective external scale with more defects, higher values of mass gain/area, and faster kinetics

Comparing Tables 4.11 and 4.15, it is notable the similarity between them, as identified oxides and mechanism. However, tests conducted in air presented faster kinetics and higher time exponent, suggesting how more detrimental is this environment. In contrast, samples tested in oxygen presented higher values for the extension of the internal reaction zone, Figure 4.47, suggesting that internal reactions are dominant in this environment and the surface takes more time to achieve the supersaturation to form the external scale.

4.5 Sulfidation & Oxidation behavior

Figure 4.48 shows the mass gain per area in function of time of TiNbCr MPE alloy and Haynes 188 tested under sulfidation & oxidation up to 100h at 600, 800, 900, 1000 and 1100°C, where it is possible to highlight that Haynes 188 presents significant spallation under all testing conditions.

It is important to highlight that the total mass gain considered in these graphs represents the combination effects of oxidation, sulfidation, and spallation, as will be discussed on subsequently.

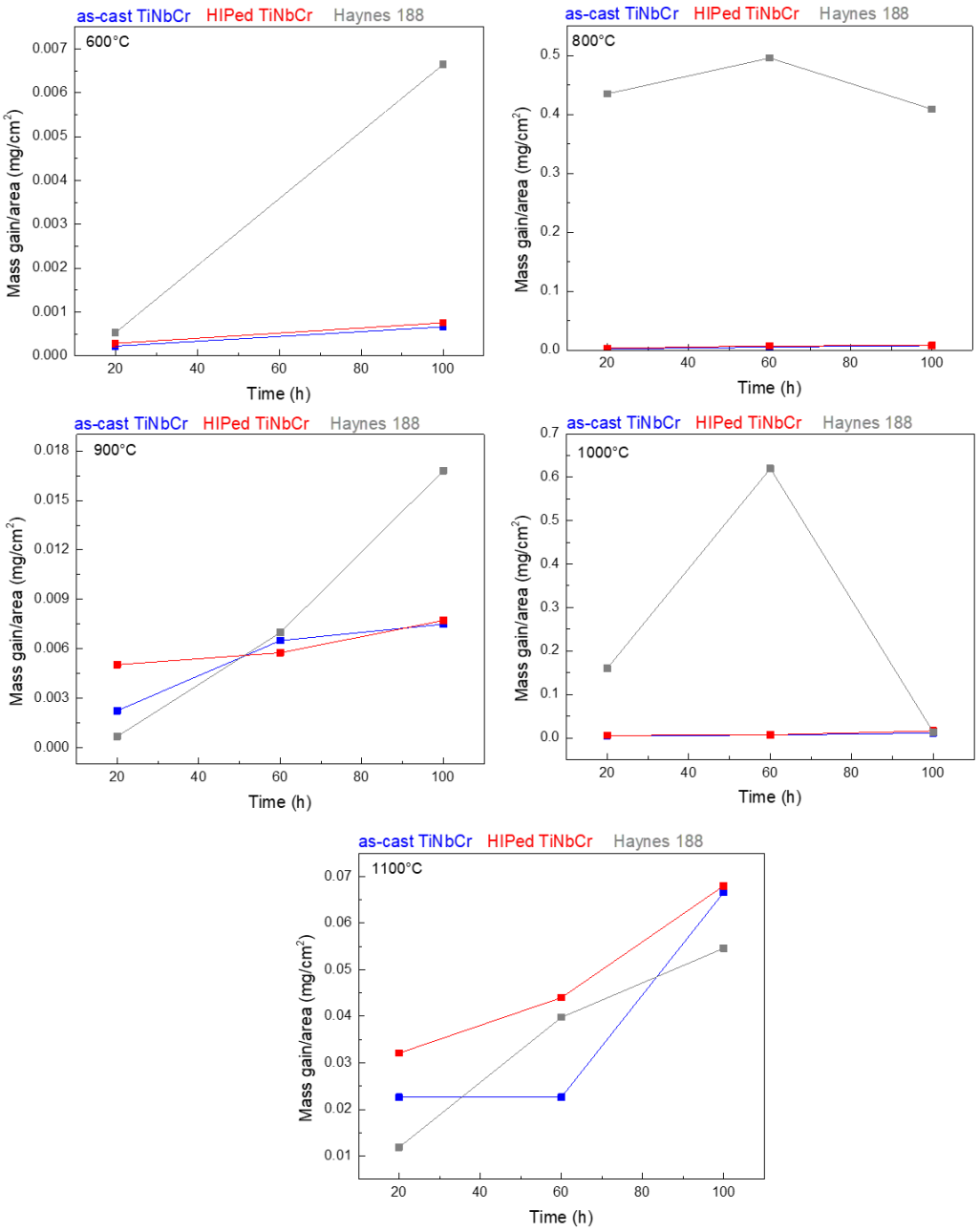

Figure 4.48 - Mass gain/area in function of the time of samples tested in sulfidation & oxidation.

As applied in the oxidation tests, the general growth rate law was used to analyze the kinetics data according to Equation 9. The results are shown in the Table 4.16 for the TiNbCr MPE alloy. Due to the spallation generated in the Haynes 188, this analysis was impossible.

Analyzing the time exponent in the Table 4.16 it is highlighted that the behavior is approximately parabolic, specially at lower temperatures. However, increasing the temperature up to 1100°C the scaling behavior tends to a mixed-mode, as described by Welch et al. [33] and discussed previously.

Table 4.16 - Reaction rate constants (k) and time exponents (n) for TiNbCr MPE alloy at 600, 800, 900, 1000 and 1100°C.

Alloy	Temperature (°C)	n	R^2	$k\ (\frac{g}{cm^2 s^n})$
as-cast TiNbCr	600	0.58	0.99	$4.21x10^{-11}$
	800	0.53	0.99	$8.72x10^{-9}$
	900	0.58	0.99	$5.92x10^{-9}$
	1000	0.61	0.99	$4.91x10^{-9}$
	1100	0.68	0.97	$2.70x10^{-7}$
HIPed TiNbCr	600	0.55	0.99	$6.73x10^{-11}$
	800	0.53	0.99	$8.66x10^{-9}$
	900	0.52	0.99	$6.31x10^{-9}$
	1000	0.60	0.99	$6.65x10^{-9}$
	1100	0.69	0.99	$1.51x10^{-7}$

The topography section of each alloy tested during 100h in sulfidation & oxidation test at 600, 800, 900, 1000 and 1100°C is show in Figures 4.49 – 4.51, with the identification of the products formed by EDS analysis and XRD, Table 4.17 and Figure 4.52. Due to the chemical similarity, just the XRD of condition HIPed is shown.

Topography sections highlight that Haynes 188 in sulfidation & oxidation tests and TiNbCr MPE alloy in both conditions exhibited Cr sulfide and oxide, however the smaller grain size of topography morphology suggests slower kinetics for the MPE alloy.

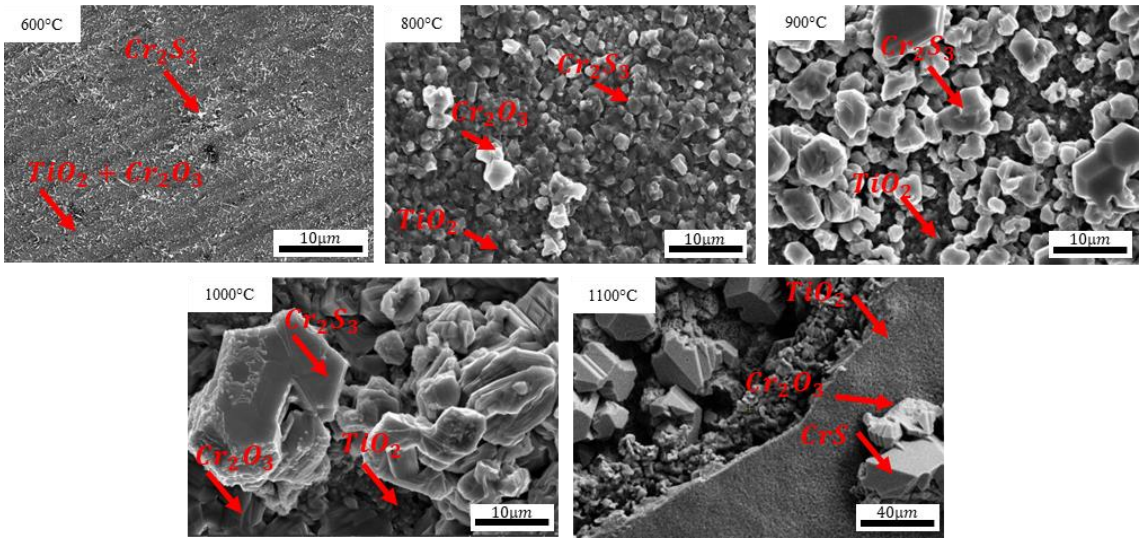

Figure 4.49 - Topography section by SEM of as-cast TiNbCr MPE alloy after 100h sulfidation & oxidation test.

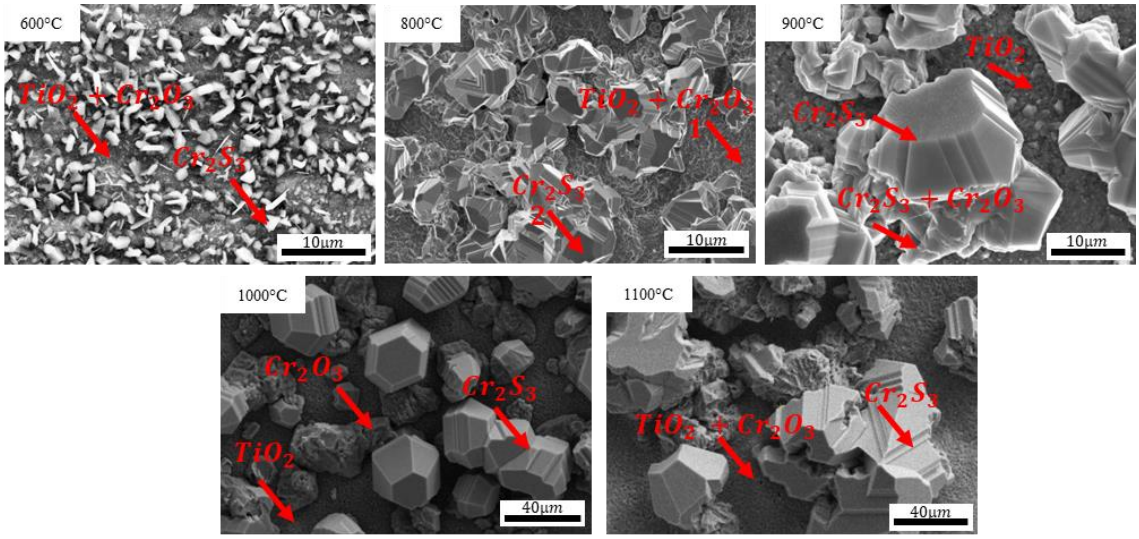

Figure 4.50 - Topography section by SEM of HIPed TiNbCr MPE alloy after 100h sulfidation & oxidation test.

Table 4.17 - EDS analysis results for areas shown in Figure 4.50.

Composition at.%	Cr	Nb	Ti	O	S
1	9.2 ± 1.2	0.9 ± 0.1	7.5 ± 1.1	80.4 ± 3.6	1.7 ± 0.8
2	28.2 ± 2.5	0.1 ± 0.1	0.7 ± 0.1	18.5 ± 1.8	51.6 ± 2.1

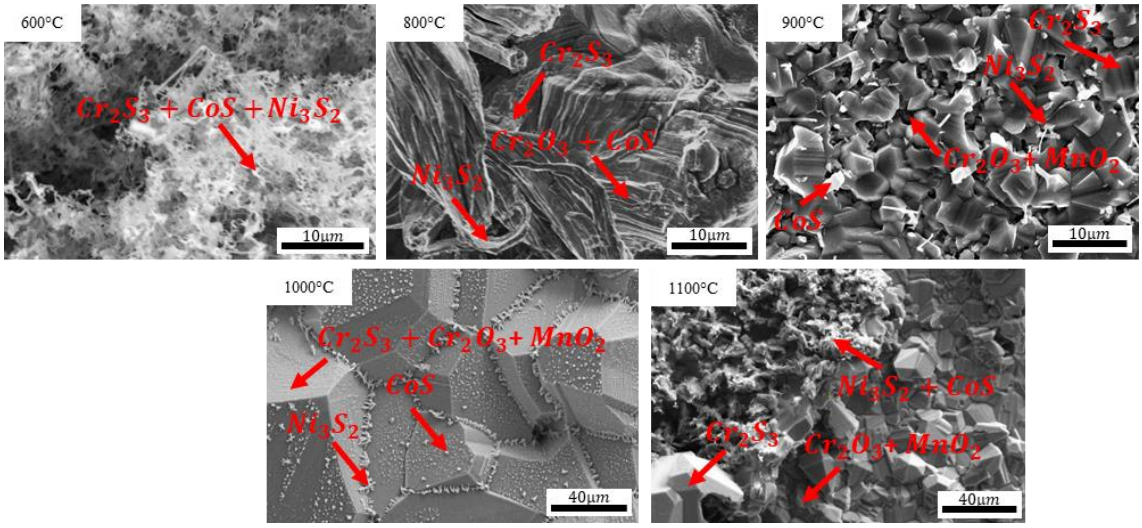

Figure 4.51 - Topography section by SEM of Haynes 188 after 100h sulfidation & oxidation test.

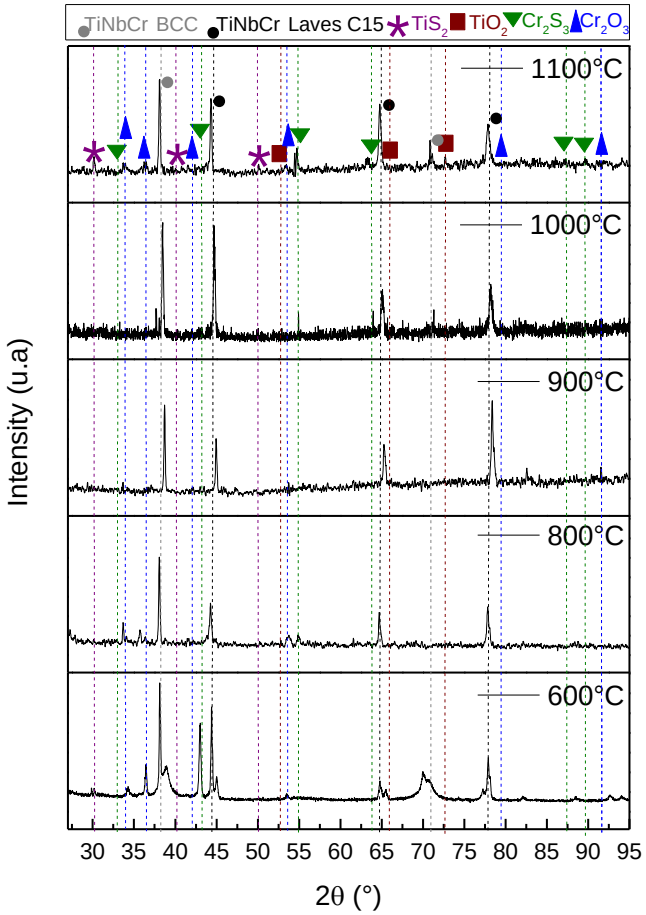

Figure 4.52 - XRD Spectra of HIPed TiNbCr MPE alloy after sulfidation & oxidation test during 100h.

The cross-section of each alloy tested in sulfidation & oxidation condition at 600, 800, 900, 1000 and 1100°C during 100h is shown in Figures 4.53 – 4.55, with the identification of species based on EDS analysis and exemplified by Table 4.18.

Haynes 188 is highlighted in the literature as having a satisfactory behavior in environments containing sulfur, with slower kinetics than other superalloys as Hastelloy X, Inconel 1671, Incoloy 800, for example [5, 73, 74]. During your studies, Douglass and colleagues [73] noted that the Haynes 188 was the only alloy that exhibits a quite linear/almost parabolic behavior in sulfidation environments.

However, Haynes 188 tested under sulfidizing environments forms Ni and Co sulfides which represents a disadvantage in its application at high temperatures, due to the eutectic reaction of $Ni+Ni_3S_2$ at 645°C and the melting point of Ni_3S_2 at 788°C, and the eutectic reaction of Co+CoS at 880°C [5]. As consequence, molten sulfides are formed and it increases the sulfide attack and can cause catastrophic sulfidation attack because they destroy the dense scale so easily [6, 73], as detected in this study for samples tested in sulfidation & oxidation tests performed at temperature ranging 900-1100°C.

Additionally to the liquid product formation, the cross-section analysis, Figure 4.55, highlight that the sulfidation & oxidation behavior of Haynes 188 is characterized by an external scale with porous and generally cracked which offers no protection in the environment with H_2S, allowing the gas to diffuse through it and keeps it in contact with the metal surface, resulting in an extensive zone of internal reaction, with the formation of internal reaction layer at 600-900°C and reaction in the grain and phase boundaries at 600-1100°C bigger than TiNbCr MPE alloy in both tested conditions.

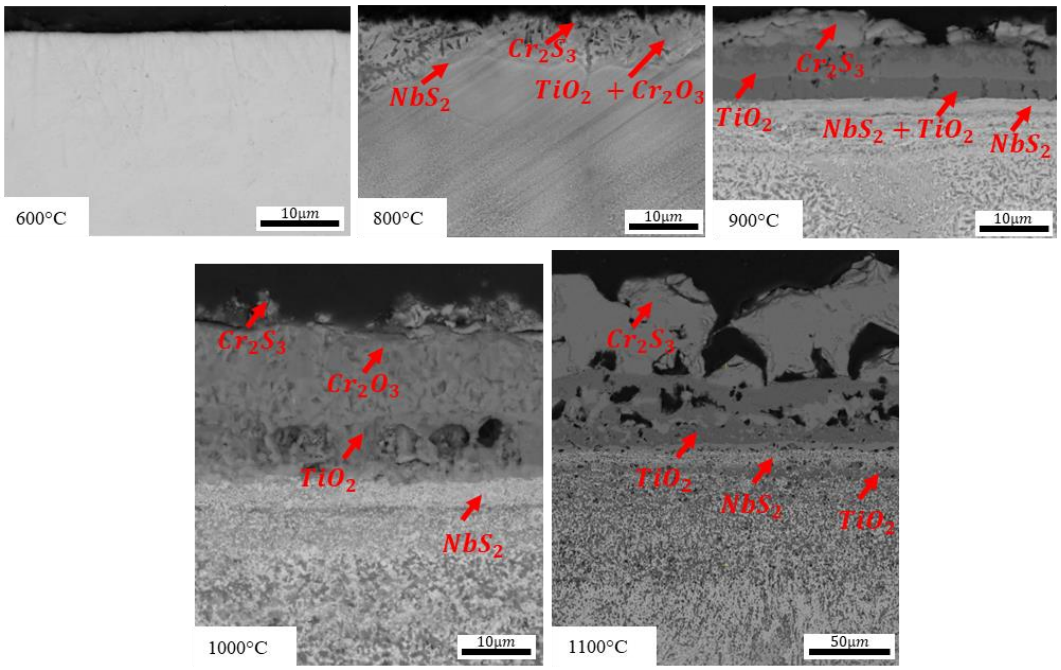

Figure 4.53 - Cross-section by SEM of as-cast TiNbCr MPE alloy after 100h sulfidation & oxidation test.

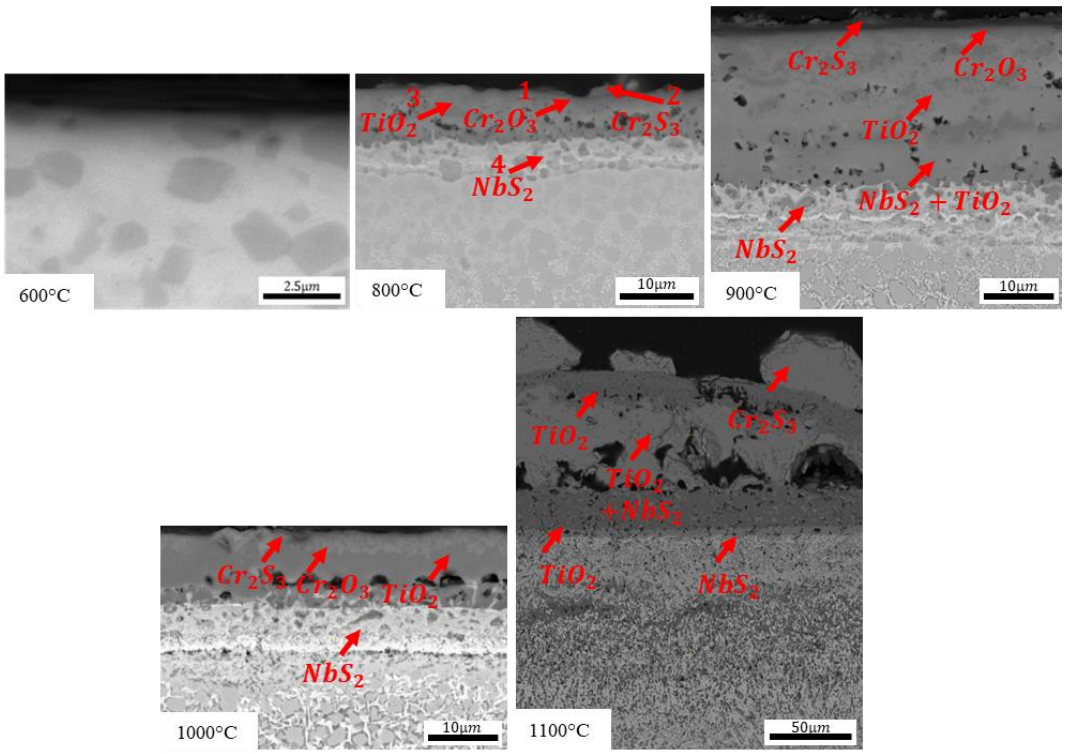

Figure 4.54 - Cross-section by SEM of HIPed TiNbCr MPE alloy after 100h sulfidation & oxidation test.

Table 4.18 - EDS analysis results for areas shown in Figure 4.54.

Composition at.%	Cr	Nb	Ti	O	S
1	20.0 ± 1.4	0.5 ± 0.1	1.0 ± 0.8	7.5 ± 1.1	71.1 ± 3.0
2	21.8 ± 1.9	0.4 ± 0.1	2.4 ± 0.6	57.8 ± 2.6	17.6 ± 1.3
3	3.0 ± 0.9	6.0 ± 0.9	13.2 ± 1.3	77.2 ± 3.2	0.7 ± 0.1
4	1.1 ± 0.3	23.6 ± 2.6	8.5 ± 1.3	15.9 ± 1.4	28.5 ± 2.1

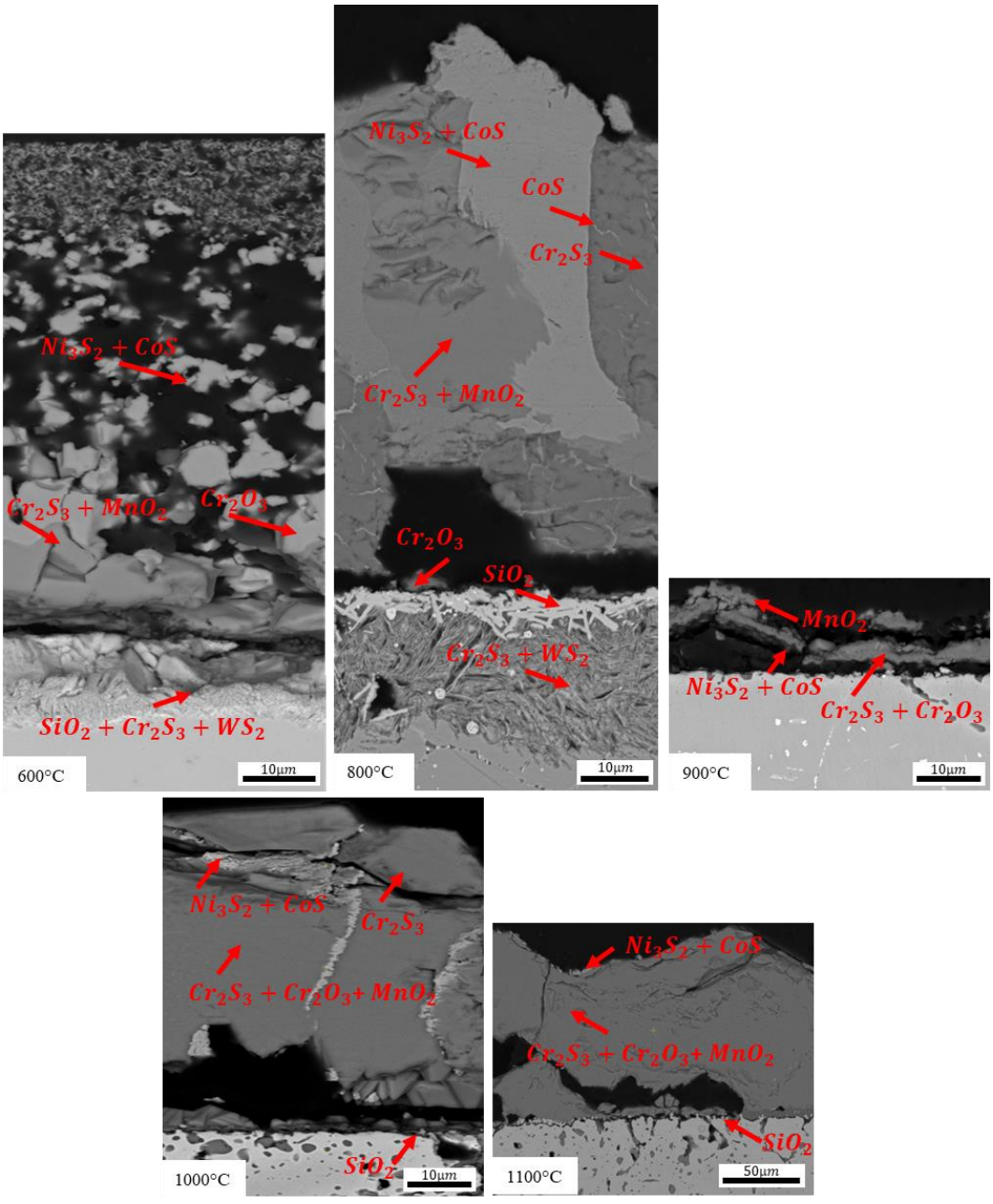

Figure 4.55 - Cross-section by SEM of Haynes 188 after 100h sulfidation & oxidation test.

The EDS mapping of TiNbCr MPE alloy, Figures 4.56 – 4.60, highlighted the elements distribution through the cross-section of samples tested after 100h of sulfidation & oxidation tests at 800, 900, 1000 and 1100°C, respectively. Due to the similarity between the conditions as-cast and HIPed, only the HIPed condition is highlighted.

It is possible to note that, the external scale is mainly composed of TiO_2. This specie is characterized by a fast formation of a non-protective scale due to the number of defects, described by a linear kinetics [2, 44]. Consequently, the gas continues diffusing through the scale, keeping contact with the alloy and being consumed by the scale growth and the dissociation into the alloy, which is highlighted by internal NbS_2 layer formation.

As shown in the cross-section of TiNbCr MPE alloy tested by sulfidation & oxidation tests, no internal oxidation is highlighted, just internal sulfidation, which suggests that the oxygen was consumed by the TiO_2 scale and the diffusion inward of sulfur anions possibilities the sulfidation of Nb.

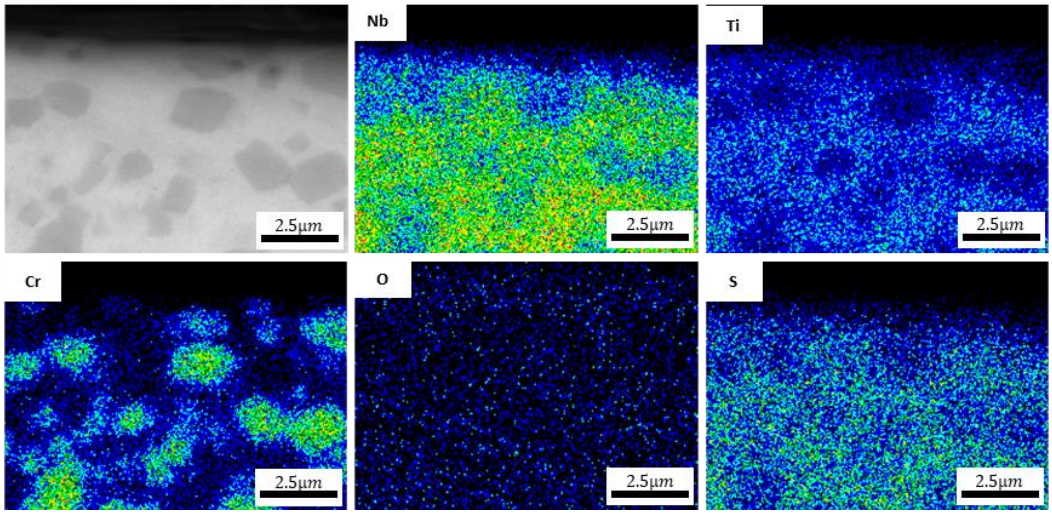

Figure 4.56 - EDS Mapping of cross-section of HIPed TiNbCr MPE alloy after 100h sulfidation & oxidation test at 600°C.

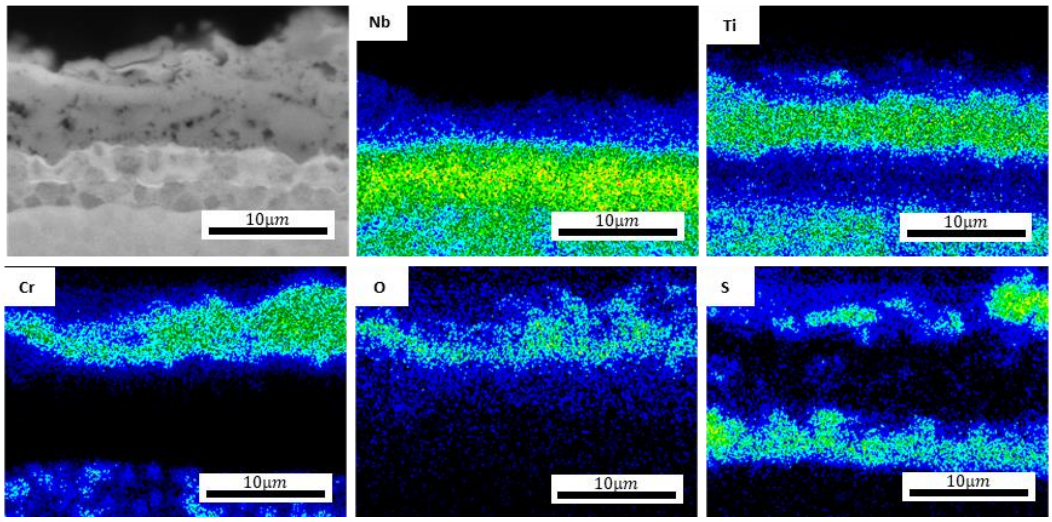

Figure 4.57 - EDS Mapping of cross-section of HIPed TiNbCr MPE alloy after 100h sulfidation & oxidation test at 800°C.

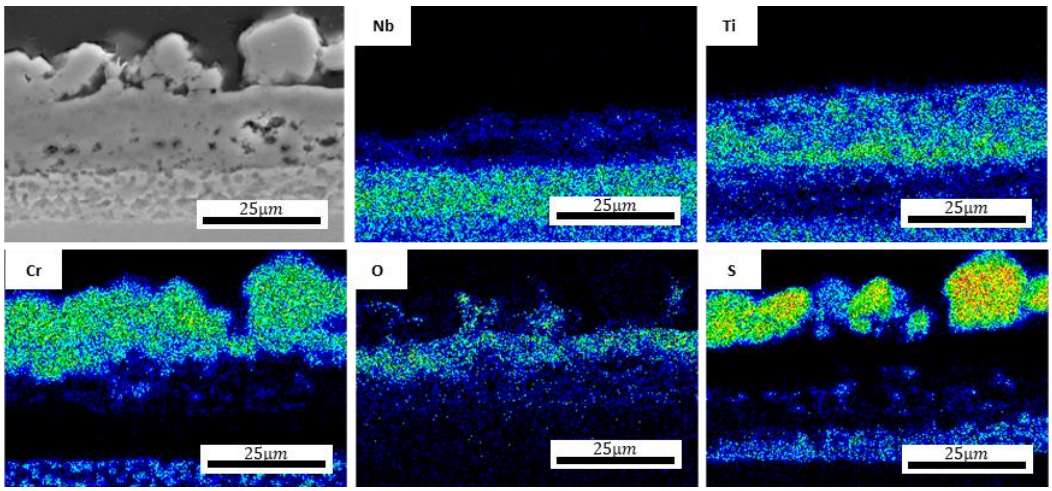

Figure 4.58 - EDS Mapping of cross-section of HIPed TiNbCr MPE alloy after 100h sulfidation & oxidation test at 900°C.

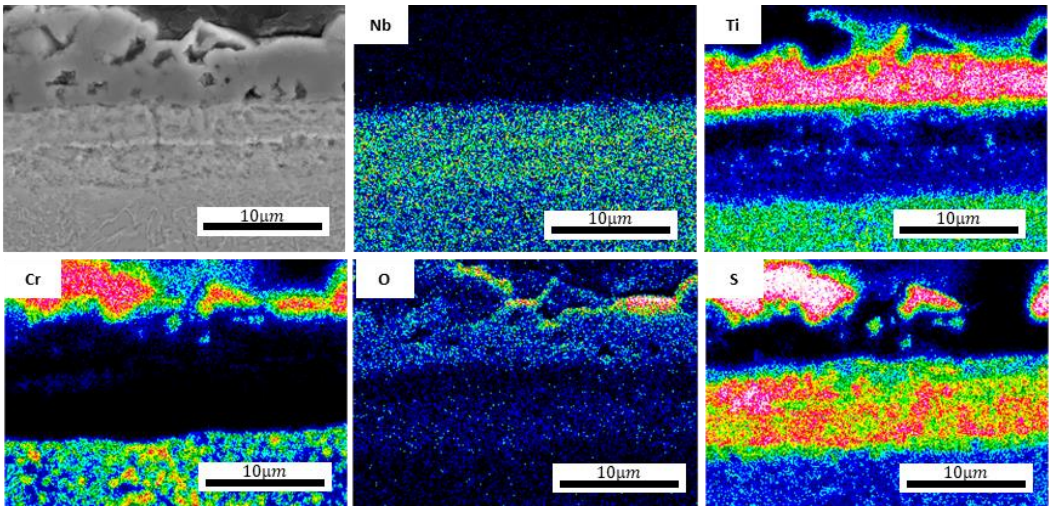

Figure 4.59 - EDS Mapping of cross-section of HIPed TiNbCr MPE alloy after 100h sulfidation & oxidation test at 1000°C.

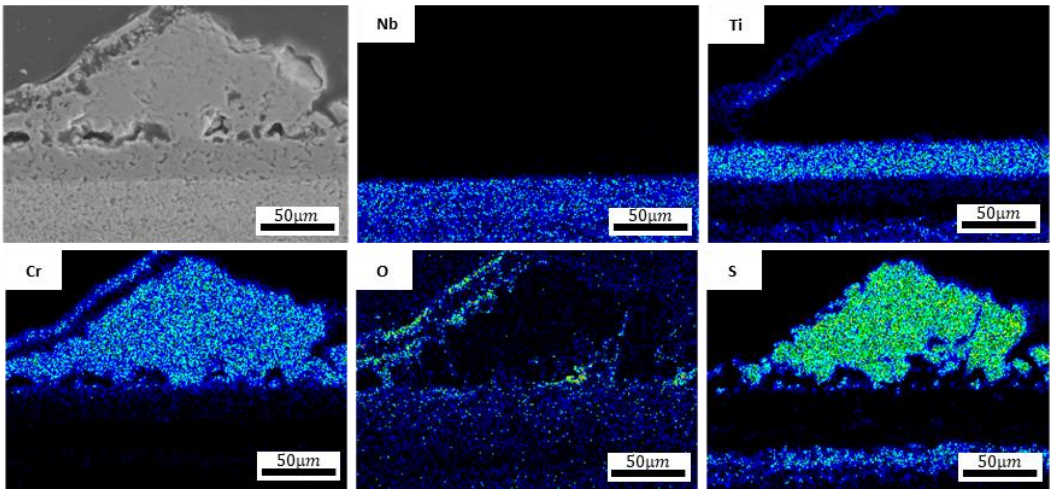

Figure 4.60 - EDS Mapping of cross-section of HIPed TiNbCr MPE alloy after 100h sulfidation & oxidation test at 1100°C.

As highlighted by Strafford and Datta [66] and Gleeson [59], while Cr and Ti sulfides/oxides are formed by outward cations diffusion, Nb is one exception in sulfidizing environments due to the slower kinetics than its oxides. NbS_2 has a rate comparable to Cr_2O_3, and according to Figure 3.3, it is not expected to be formed in the surface, so the formation of external layer composed of Ti and Cr products reduces the partial pressure of oxygen enough to form NbS_2, as noted in the cross-section Figures 4.53 and 4.54.

As mentioned in the Literature review section, Chyrkin [53] reported, for oxidation, an uphill-diffusion of Nb towards the scale/alloy interface due to the Cr-Nb positivity chemical interaction.

Similarly, to Chyrkin [53] studies, it is suggested that TiNbCr MPE alloy in sulfidation & oxidation tests, exhibited the Cr products formation due to the outward Cr diffusion because of the high chemical activity of Cr. This movement generated a local depletion of Cr which increases the Nb activity, forming Nb sulfide.

As the gas continues diffusing through the scale with no barrier it achieves the alloy, rich in Nb, the Nb sulfide layer formation is promoted and consequently, offer protection against sulfur diffusion, as shown in Figures 4.53 and 4.54 where it is possible to highlight the internal reaction zone at 600 and 800°C occurs due to the inner layer formation and no attack in grain and phase boundaries.

However, the protection offered by NbS_2 is decreased with an increasing of temperature as suggested by Figures 4.53 and 4.54, where it is noted the presence of attack in grain and phase boundaries, and it is more intense at 1100°C when the kinetic rate is the highest, and the time exponent is further that the parabolic value (0.5), Table 4.16.

Table 4.16 shows a time exponent, for the MPE alloy, between 0.5 and 1, suggesting that the behavior is a mixed mode, which involves diffusion and interface-control. However, after analyzing the topography and cross-section, it is suggested a domination by the parabolic behavior due to the protection offered.

Figures 4.53 and 4.54 suggest that the TiNbCr MPE alloy has different regimes according to the temperature. The first one is protective (600°C), almost no internal reaction zone is notable; the second is semi-protective (800-1000°C) kinetics is quietly higher than at 600°C and an external scale is formed adherent to the surface and an internal reaction zone is observe; and, the last at 1100°C with extensive attack, fast kinetics, as supported by the cross-sections, Figures 4.53 and 4.54. The protection offered by NbS_2 is semi-protective due to higher kinetics rate values than NbS_2, which may happen due to the structure of NbS_2 crystals [65].

As mentioned in the Literature review section, Gleeson and colleagues [58] reported that MoS_2 is protective in pure Mo sulfidation, however semi-protective in Co-Mo alloys, similar to observed to TiNbCr MPE alloy. According to the researchers, it can be explained by the Van der Walls gap between the MoS_2 crystals, where it is possible to Co intercalate.

Like MoS_2, NbS_2 has a hexagonal crystal structure, characterized by the sequence …SNbS SNbS SNbS…, which the S-Nb-S layers are bonded covalently, or sandwiches held by weak Van der Waals forces [57, 95-97]. Consequently, between NbS_2 sandwich Cr and Ti that are diffusing outward to form the external scale can be intercalated into this space, the Van der Waals gap.

As suggested by Gleeson et al. [58] for Co-Mo alloys, the continuous layer of NbS_2 formed on the TiNbCr MPE alloy did not act as an effective barrier to the outward diffusion of Ti and Cr. The NbS_2 layer provided short-circuit paths for Ti^{4+} and Cr^{3+} ions [97].

On the other hand, the growth rate of NbS_2 on pure Nb is extremely low, comparable to Cr oxidation, probably owing to the slow diffusional transport of Nb and S through the covalently bonded planes in NbS_2 [57, 95-97].

Moreover, linking the results obtained in this study with Butler and colleagues study made in air at 1200°C [32] and the oxidation results discussed previously, it is noted that the oxidative environment is more detrimental to the TiNbCr MPE alloy than sulfidizing environment due to the formation of a defected scale which exhibits linear kinetics. This observation highlights the exception of Nb and how it can protect the alloy [59].

Comparing the kinetics of as-cast TiNbCr MPE alloy with the HIPed, Table 4.16, it is suggested that Cr do not offer much protection against this environment because the kinetics is similar at all temperature and the main difference between than is Laves phase fraction and size, and Laves phase is rich in Cr as discussed before.

Due to the extensive spallation of Haynes 188, the comparison of this alloy and the TiNbCr MPE alloy is shown in Figure 4.61 in terms of the internal reaction extension zone for samples tested during 100h. It is highlighted how more

detrimental is the behavior of Haynes 188 compared to TiNbCr MPE alloy and how the liquid product formations increase the attack, as increasing temperature the internal reaction zone also increases its extension in Haynes 188, especially at temperatures higher than 645°C (first liquid formation – eutectic reaction). At 600°C the internal reaction extension zone in the TiNbCr MPE alloy was less than 1µm, so it is not detected in the graphic in the Figure 4.61, as shown in Figures 4.53 and 4.54.

Additionally, Figure 4.62 illustrates a comparative analysis of the internal reaction zone extension among isothermal tests conducted in air, oxygen, and under sulfidation & oxidation atmospheres. Notably, oxygen emerges as the most detrimental condition for the TiNbCr MPE alloy. When comparing tests conducted in air and under sulfidation & oxidation, it is evident that while the former exhibits a smaller extension, the latter indicates both the formation of an inner protective layer and the extent of the attack.

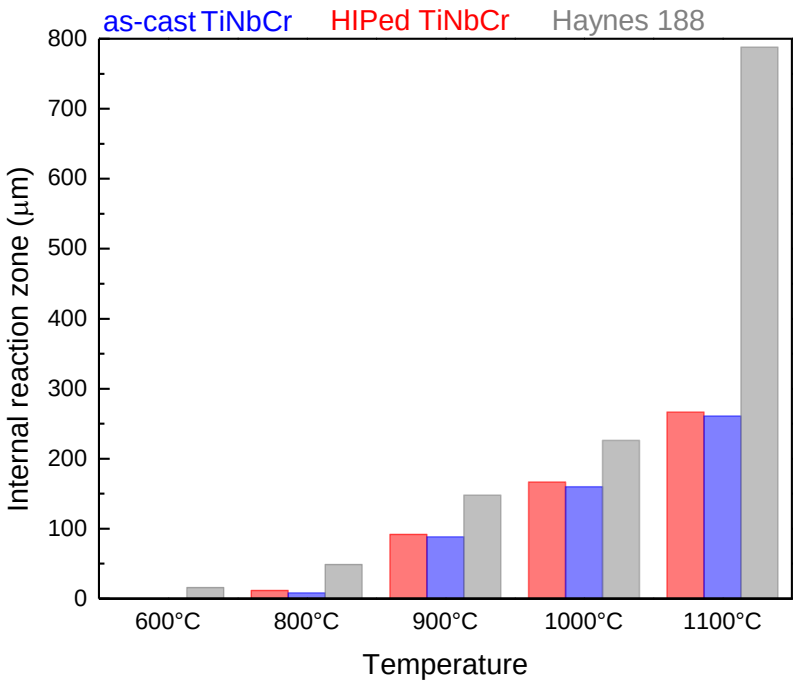

Figure 4.61 - Internal reaction extension of as-cast and HIPed TiNbCr MPE alloy in comparison of Haynes 188 after 100h of sulfidation & oxidation tests.

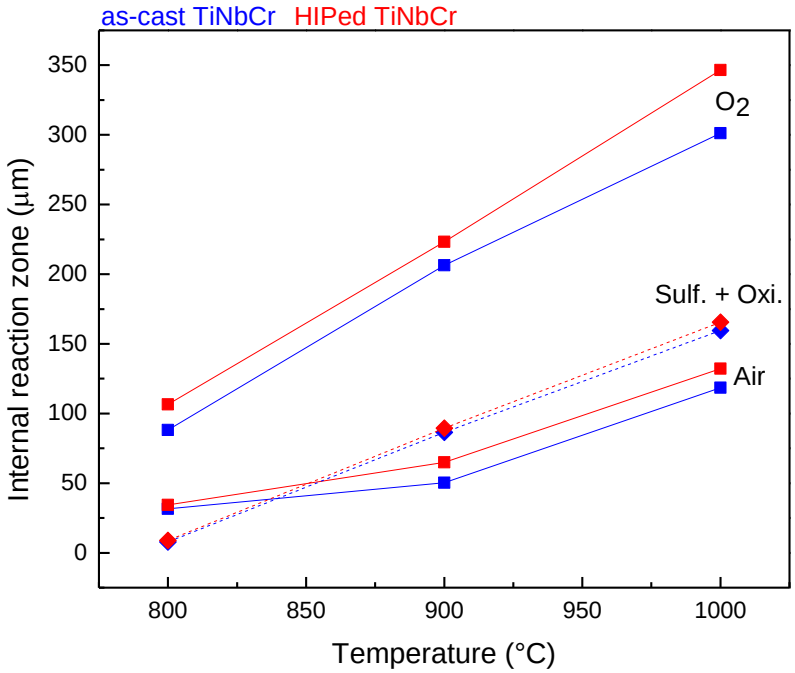

Figure 4.62 - Comparison based on Cross-Section SEM of Internal reaction zone extension after 100h-testing.

Table 4.19 highlights the key points observed in sulfidation & oxidation tests as discussed in this section for TiNbCr MPE alloy in both conditions. Comparing Tables 4.19, 4.15 and 4.11, a significant inversion in behavior between the TiNbCr MPE alloy and Haynes 188 becomes apparent. While Haynes 188 exhibits satisfactory, protective, and parabolic behavior in oxidation tests, the opposite trend emerges in sulfidation & oxidation tests, characterized by linear kinetics. Conversely, the TiNbCr MPE alloy displays non-satisfactory, non-protective, and linear behavior in oxidation tests, while in sulfidation & oxidation, the trend reverses with parabolic kinetics.

Table 4.19 - Key points of sulfidation & oxidation tests for TiNbCr MPE alloy.

Testing condition	$\log(P_{S2}) = -3$ and $\log(P_{O2}) = -6$; 600, 800, 900, 1000 and 1100°C; 20, 60, and 100h
Identified products	TiO_2, TiS_2, Cr_2O_3, Cr_2S_3, and NbS_2
Mechanism	Semi-protective inner layer rich in NbS_2 is formed by uphill Nb ion diffusion
Kinetics	Parabolic
Time exponent and reaction rate constant (g/cm^2s^n)	as-cast: $600°C\ n = 0.58\ k = 4.21x10^{-11}$ $800°C\ n = 0.53\ k = 8.72x10^{-9}$ $900°C\ n = 0.58\ k = 5.92x10^{-9}$ $1000°C\ n = 0.61\ k = 4.91x10^{-9}$ $1100°C\ n = 0.68\ k = 2.70x10^{-7}$ HIPed: $600°C\ n = 0.55\ k = 6.73x10^{-11}$ $800°C\ n = 0.53\ k = 8.66x10^{-9}$ $900°C\ n = 0.52\ k = 6.31x10^{-9}$ $1000°C\ n = 0.60\ k = 6.65x10^{-9}$ $1100°C\ n = 0.69\ k = 1.51x10^{-7}$
Comparison with Haynes 188	TiNbCr MPE alloy forms a semi-protective inner layer scale, Haynes 188 is not protective, has pore spallation, and forms liquid products which increases the internal reaction zone extension

4.6 Sulfidation behavior

Figure 4.63 shows the results of TiNbCr MPE alloy and Haynes 188 tested under sulfidation condition at 800°C up to 100h in terms of mass gain/ area (a) where it is possible to evidence the spallation of Haynes 188 and due to it, in terms of internal reaction extension (b).

Fitting the data from Figure 4.63 (a) for TiNbCr MPE alloy in both conditions according to Equation 9, it is noted that the alloy keeps the approximately parabolic behavior even reducing the partial pressure of oxygen and the kinetics is slower than samples tested in sulfidation & oxidation test at 800°C, Table 4.19, as highlighted by Table 4.20.

It is important to emphasize that the total mass gain considered in these graphs represents the combination effects of sulfidation, and spallation, as will be discussed on subsequently and in the case of Haynes 188 oxidation as well.

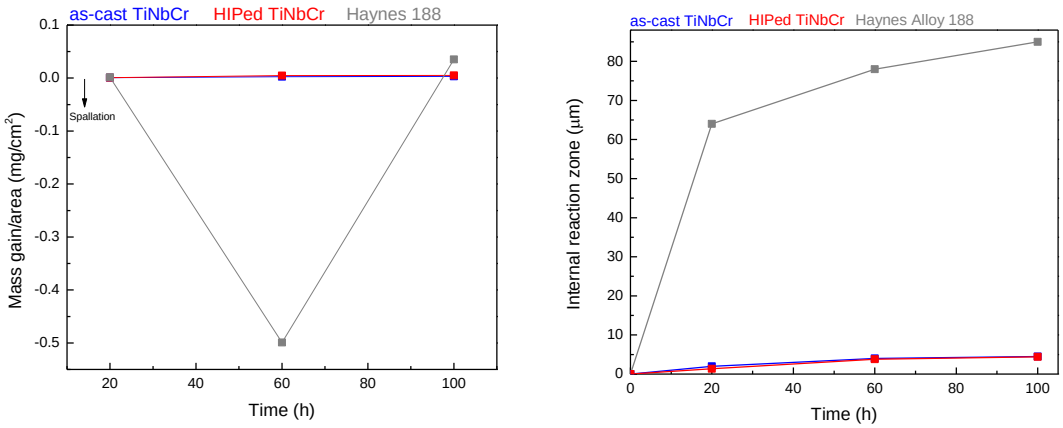

(a) (b)

Figure 4.63 - Comparison between as-cast and HIPed TiNbCr MPE alloy and Haynes 188 under sulfidation tests performed at 800°C up to 100h. (a) mass gain per area in function of time testing and (b) internal reaction extension in function of the time.

Table 4.20 - Reaction rate constants (k) and time exponents (n) for TiNbCr MPE alloy sulfidized at 800°C.

Alloy	n	R^2	$k\ (\frac{g}{cm^2 s^n})$
as-cast TiNbCr	0.48	0.99	$2.26\ x\ 10^{-9}$
HIPed TiNbCr	0.49	0.99	$5.79\ x\ 10^{-9}$

The topography section of the alloys sulfidized at 800°C up to 100h is shown in Figures 4.64 – 4.66 with the identification of formed species based on EDS analysis and supported by XRD, Figure 4.67. Due to the similarity between the conditions as-cast and HIPed, only the XRD of the HIPed TiNbCr MPE alloy is shown.

Comparing Figures 4.64 and 4.65 with the Figure 4.66, it is possible to highlight that TiNbCr MPE alloy in both conditions exhibit bigger Cr_2S_3 grains than TiS_2 suggestion faster kinetics. Haynes 188 also presents Cr_2S_3, however there are Ni_3S_2 and CoS precepted as flower shapes above and between the Cr_2S_3

grains, due to the molten products discussed previously in the section Sulfidation & Oxidation behavior.

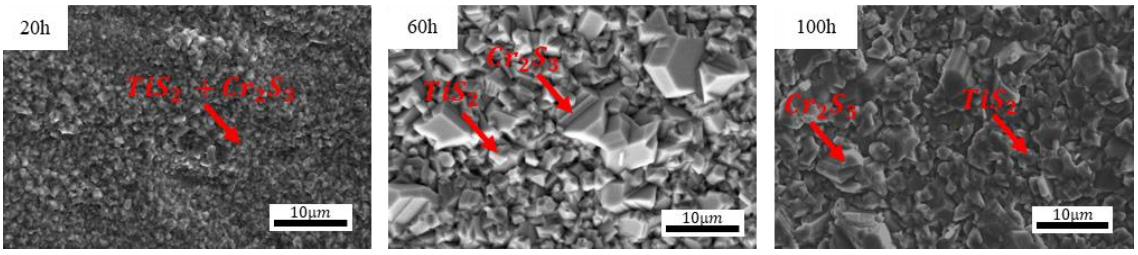

Figure 4.64 - Evolution of topography section of as-cast TiNbCr MPE alloy with the time during sulfidation test at 800°C.

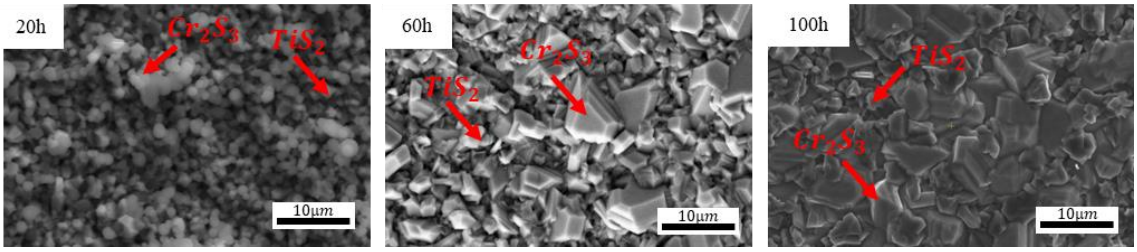

Figure 4.65 - Evolution of topography section of HIPed TiNbCr MPE alloy with the time during sulfidation test at 800°C.

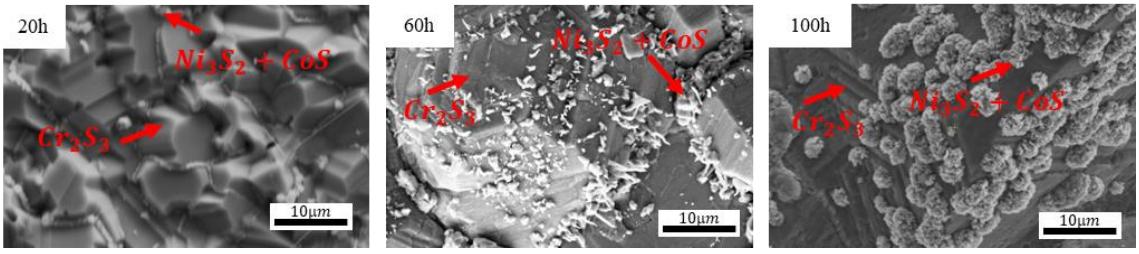

Figure 4.66 - Evolution of topography section of Haynes 188 with the time during sulfidation test at 800°C.

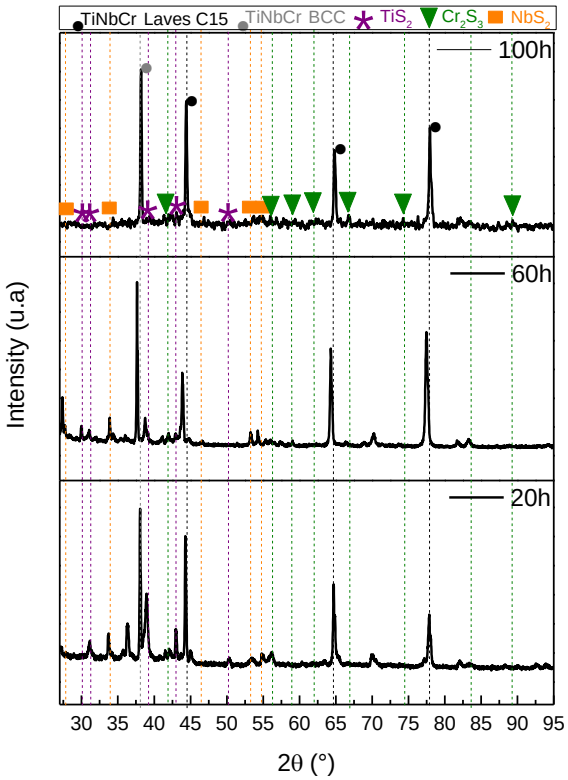

Figure 4.67 - XRD Spectra of HIPed TiNbCr MPE alloy after sulfidation tests at 800°C during 20, 60 and 100h.

The cross-section of tested TiNbCr MPE alloy in both conditions and Haynes 188 samples at 800°C under sulfidizing environment is shown in Figures 4.68 – 4.71, where it is possible to highlight no oxides formation in the case of TiNbCr MPE alloy in both condition, as predicted by stability Figure 3.3, however, in the case of Haynes 188, SiO_2 is still formed, Figure 4.70.

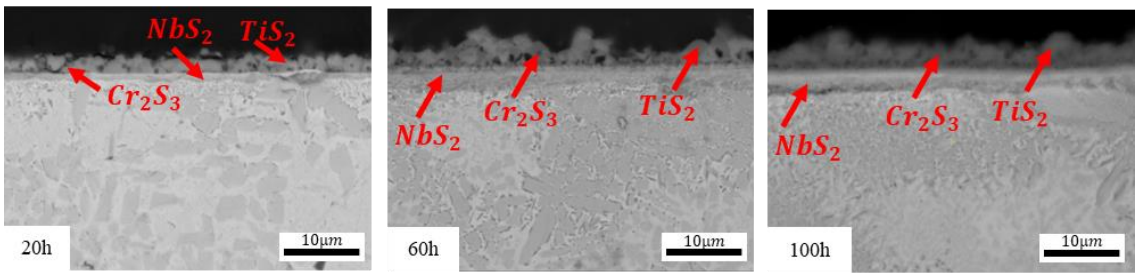

Figure 4.68 - Evolution of cross-section of as-cast TiNbCr MPE alloy with the time during sulfidation test at 800°C.

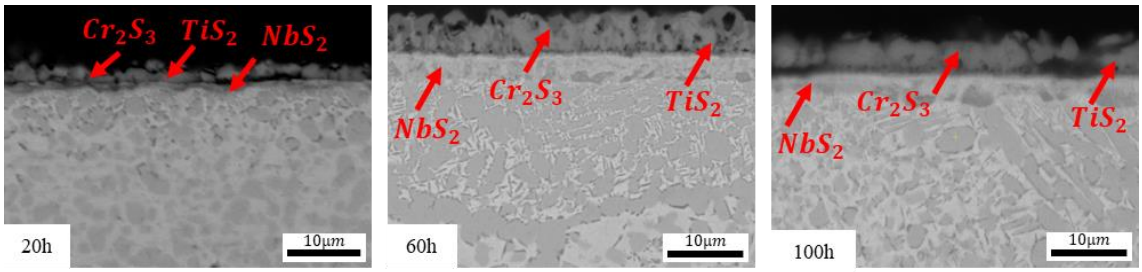

Figure 4.69 - Evolution of cross-section of HIPed TiNbCr MPE alloy with the time during sulfidation test at 800°C.

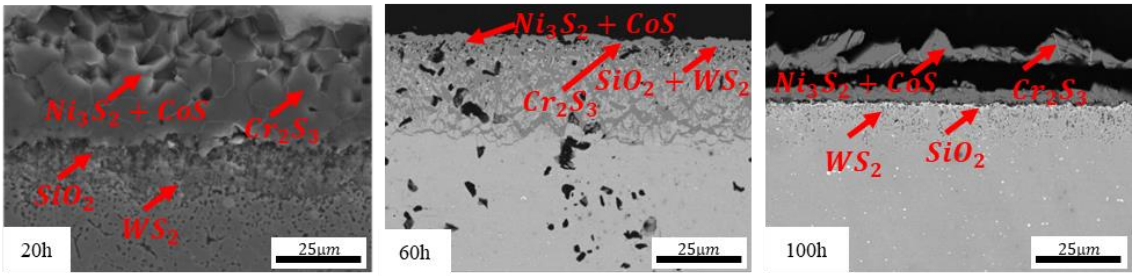

Figure 4.70 - Evolution of cross-section of Haynes 188 with the time during sulfidation test at 800°C.

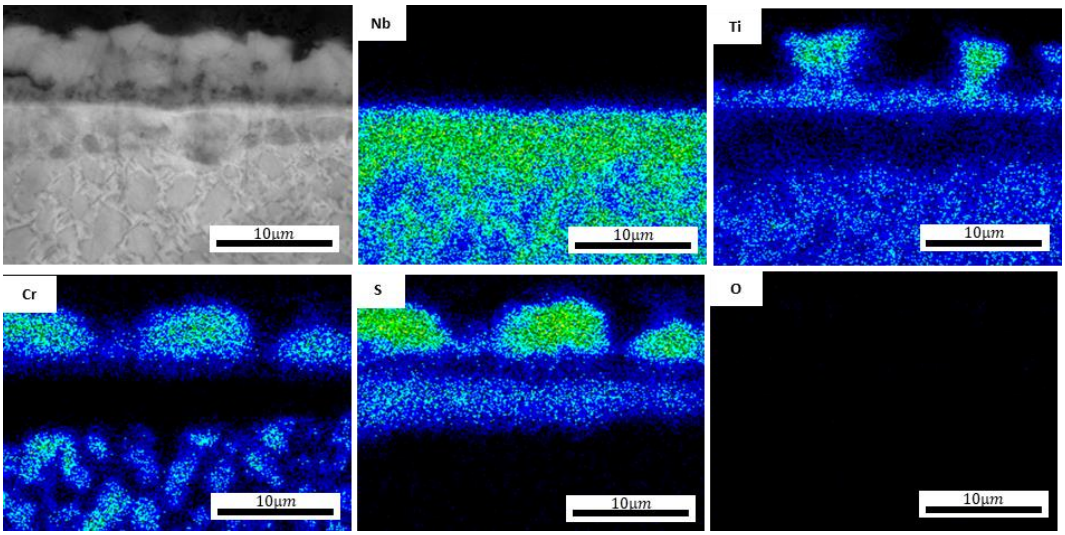

Figure 4.71 - EDS Mapping of cross-section of HIPed TiNbCr MPE alloy after 100h sulfidation test at 800°C.

TiNbCr MPE alloy in both conditions exhibited an external sulfide scale composed of TiS_2 with Cr_2S_3 nodules formed due to the outward cation diffusion and an internal sulfide layer composed of NbS_2 formed due to inward anion

diffusion, as sulfidation & oxidation tests. Additionally, increasing time, the external layer became denser, suggested by Figures 4.64, 4.65, 4.68 and 4.69, because of the grain growth, specially TiS_2, as identified by EDS analysis.

Comparing the kinetics of oxidation tests at 800°C with sulfidation tests at the same temperature, Tables 4.11, 4.15, 4.19, and 4.20, it is noted that the kinetics is slower reducing the partial pressure of oxygen.

As discussed before, typically, metals exhibit higher kinetics in sulfidation than oxidation, however, refractory metals like Nb, Mo, W and Ta are exceptions, Nb for example has a rate comparable to Cr oxidation, in studies conducted in pure Nb [6, 57].

However, as reported in sulfidation & oxidation tests, the kinetics of TiNbCr MPE alloy is higher than pure Nb, suggested by the diffusion of ions of Ti and Cr and, consequently, they intercalate he Van der Waals gap of NbS_2 [61, 97].

Nevertheless, comparing sulfidation & oxidation tests with sulfidation tests, both at 800°C, it is highlighted that the kinetics is reduced with a decrease in the partial pressure of oxygen, this observation suggest a protective hole of Ti sulfide layer, because it is formed in sulfidation tests and it is not formed in sulfidation & oxidation test Figures 4.53, 4.54, 4.68 and 4.69.

Chen and Douglass [98] evaluated the influence of ternary element (Ti, Al, Mn, Cr and V) in the Ni-Mo alloys in sulfidation tests at 600, 700 and 800°C with a partial pressure of sulfur equals to 0.01 atm.

The researchers reported that all tested alloys exhibited the semi-protective MoS_2 layer formation because of the Van der Waals gap, however a reduction in the kinetics of the binary alloy. Comparing the alloy with Ti addition (Ni-30Mo-12.5Ti) with the alloy with Cr addition (Ni-28Mo-13.5Cr), they observed a parabolic behavior, however, the Cr addition was more beneficial due to the discrete external layer formation and Ti addition exhibited a non-continuous layer, which suggested than the influence of phases because this alloy was the most complex in terms of microstructure (three-phase alloy) [98].

According to Gorr et al. [2] the hole of Ti in sulfidation tests is not conclusive due to its high oxygen solubility, which become harder this study. While some studies report that the Ti addition is able to reduce the sulfidation

kinetics, for example Ti addition in Ni-Mo alloy [98] and a parabolic behavior in the case of Ti-6Al-4V [72], others highlight that Ti addition increases the sulfur diffusion in case of TiO_2 formation [57].

As discussed before, the main difference between as-cast TiNbCr MPE alloy with HIPed is the Laves phase fraction and the size of its precipitates. Due to Laves phase is a Cr-rich phase, Table 4.20 data suggests almost no influence of Cr in sulfidation behavior because the kinetics rates are similar, as observed in sulfidation & oxidation test Table 4.19.

As mentioned before, the kinetics of sulfidation & oxidation tests is higher than in sulfidation tests, suggesting that the oxides formed in the first condition do not protect the alloy against the environment and also the TiO_2 increases the diffusion of sulfur as reported by Mrowec [57].

Additionally, Figure 4.72 illustrates a comparative analysis of the internal reaction zone extension among isothermal tests conducted in air, oxygen, under sulfidation & oxidation and sulfidation atmospheres. Notably, as discussed previously, the presence of oxygen in the atmosphere emerges as the most detrimental condition for the TiNbCr MPE alloy.

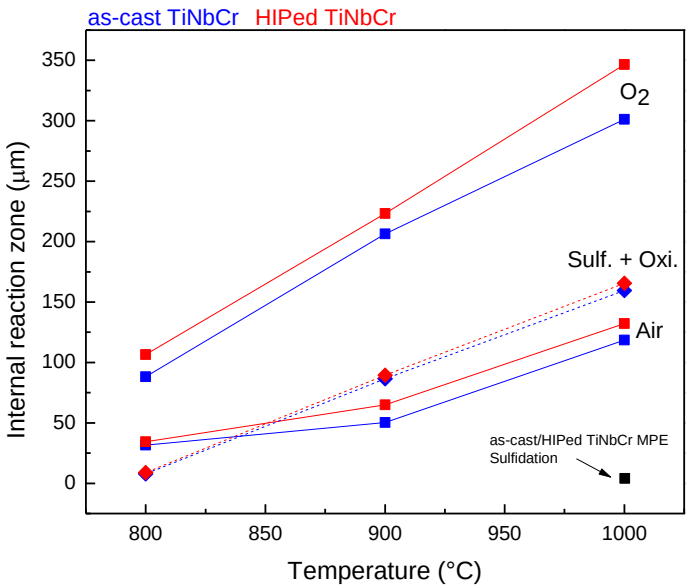

Figure 4.72 - Comparison based on Cross-Section SEM of Internal reaction zone extension after 100h-testing.

Table 4.21 highlights the key points observed in sulfidation tests as discussed in this section for TiNbCr MPE alloy in both conditions.

Comparing Tables 4.21, 4.19, 4.15 and 4.11, the significant inversion in behavior between the TiNbCr MPE alloy and Haynes 188 highlighted in the sulfidation & oxidation tests is valued, and different from sulfidation & oxidation tests only sulfides are formed.

Table 4.21 - Key points of sulfidation tests for TiNbCr MPE alloy.

Testing condition	$\log(P_{S2}) = -3$ and $\log(P_{O2}) = -26$; 800°C; 20, 60 and 100h
Identified products	TiS_2, Cr_2S_3, and NbS_2
Mechanism	Semi-protective inner layer rich in NbS_2 is formed by uphill Nb ion diffusion
Kinetics	Parabolic
Time exponent and reaction rate constant (g/cm^2s^n)	as-cast: $800°C\ n = 0.48\ k = 2.26x10^{-9}$ HIPed: $800°C\ n = 0.49\ k = 5.79x10^{-9}$
Comparison with Haynes 188	TiNbCr MPE alloy forms a semi-protective inner layer scale, Haynes 188 is not protective, has pore spallation, and forms liquid products which increases the internal reaction zone extension

5 CONCLUSIONS

5.1 TiNbCr MPE alloy

The development of TiNbCr MPE alloy is reported in this thesis, where it is noted that the alloy is composed of a BCC matrix with Laves phase C15, and the Laves phase fraction trend to be reduced with an increase in the temperature. Consequently, a decrease in microhardness and hardness were observed.

The TiNbCr in condition as-cast is characterized by a dendrite structure, composed of Nb, Ti- rich BCC dendrites with fine (Nb, Ti)Cr_2 Laves precipitates along grain boundaries.

Additionally, phase transformations are highlighted, especially the HCP phase which do not occur in both studied alloy conditions, but it is characterized after the dilatometry test due to the slow cooling rate which was enough to its kinetics precipitation, and it occurs in the phase BCC/Laves boundaries.

5.2 TiNbCr MPE alloy: oxidation behavior

The oxidation behavior of TiNbCr MPE alloy was evaluated by anisothermal, isothermal and cyclic tests in air and isothermal tests in oxygen and compared to Haynes 188.

The early-stages of oxidation is characterized by a longer time to achieve the supersaturation in the surface and form an oxide scale than Haynes 188, however when it is formed it is not protective.

A linear kinetics can describe the behavior of TiNbCr MPE alloy during the oxidation process at all temperatures, however at high temperatures (1000°C) a parabolic trend is suggested due to the Cr_2O_3 formation.

The kinetics is influenced by the temperature and microstructure. While at low temperature Nb dominate the process forming a stratified porous layer by the vacancy supersaturation mechanism, at high temperatures (900-1000°C) the Cr_2O_3 starts to compete, which reduces the time exponent.

Due to the microstructure differences, at lower temperatures the condition as-cast exhibited better behavior because the Laves phase is thinner, however, increasing the temperature, the regime is dominated by Cr_2O_3, due to the smaller

Laves phase fraction, more Cr is available in the BCC matrix which favorable the Cr diffusion to the surface and form Cr_2O_3.

All tested conditions are characterized by internal reaction zone because the scale is not protective, which means that the gas continues diffusing through the scale and it ingress into the alloy, oxygen and nitrogen (tests in air) can react with the alloying elements and forming internal reacting products.

5.3 TiNbCr MPE alloy: sulfidation behavior

Reducing the partial pressure of oxygen, TiNbCr MPE alloy in both conditions samples were tested under sulfidizing & oxidizing and sulfidizing environment and compare to Haynes 188.

The MPE alloy exhibited a parabolic behavior with a behavior also characterized by Nb. This refractory element is reported by having lower sulfidation kinetic than its oxidation.

An inner layer rich in NbS_2 is formed in all tested conditions and it is favorable by the positivity chemical interaction with Cr. However, comparing with pure Nb sulfidation, the protection offered by the NbS_2 layer is semi-protective due to the Van der Waals gap in it structure which allows the Cr and Ti cations to intercalate in this structure. And at high temperature, 1100°C, a decrease in the protection is noted by the extensive internal reaction zone.

Decreasing the partial pressure of oxygen until the sulfidation tests, a decrease in the kinetics is highlighted and it is suggested by the formation of a sulfide layer rich in Ti.

TiNbCr MPE alloy, exhibited better behavior than Haynes 188 in all tested condition. Haynes 188 had a liquid product formation due to eutectic reactions and sulfide melting point which increased the attack.

6 FUTURE WORKS SUGGESTED

Based on this study, some future works can be suggested:

a) Addition of different elements in the TiNbCr alloy:
    a. Si between 0.5-1% in the alloy, to become easier the formation of Cr_2O_3 and it is expected a reduction in the oxidation kinetics.
    b. Addition of Ta to favorite the oxide complex oxide with Cr which according to recent studies exhibits protection and parabolic behavior in oxidation tests.
    c. Addition of Al to try reducing the oxidation kinetics by the Al_2O_3 formation.
b) Evaluate the hot-corrosion of TiNbCr MPE alloy type I and type II with molten salt and S addition, due to the remarkable sulfidation behavior.
c) Evaluate the sulfidation & oxidation behavior of TiNbCr MPE alloy with an increasement in the oxygen, with SO_2 gas.

7 REFERENCES

[1] BHADESHIA, H. "Leacture for Centre of Excelence in Phase Transformation and Product Characterisation," July 2021. [Online].

[2] GORR, B. et al. "Current Status of Research on the Oxidation Behavior of Refractory High Entropy Alloys," *Advanced Engineering Materials,* vol. 23, 2021.

[3] SENKOV, O. N. et al. "Development and exploration of refractory high entropy alloys - a review," *Journal of Materials Research,* 2018.

[4] GORR, B. et al. "High-Temperature Oxidation Behavior of Refractory High-Entropy Alloys: Effect of Alloy Composition," *Oxidation Of Metals,* 2017.

[5] SMOLIK, G. and LINN, J. E. "Behavior of Pressurized Tubes of Candidate Alloys in a Simulated Low-Btu Environment," Journal of Materials for energy systems, 1986.

[6] MROWEC, S. "The Problem of Sulfur in High-Temperature Corrosion," *Oxidation of Metals,* 1994.

[7] CANTOR, B. et al. "Microstructural development in equiatomic multicomponent alloys," *Materials Science Engineering A,* 2004.

[8] YEH, J. W. et al. "Formation of simple Crystal structures in Cu-Co-Ni-Cr-Al-Fe-Ti-V alloys with multiprincipal metallic elements," Metallurgical and Materials, 2004.

[9] MIRACLE, D. B. and SENKOV, O.N. "A critical review of high entropy alloys and related concepts," Acta Materialia, 2017.

[10] SENKOV, O. N. et al. "Accelerated exploration of multi-principal element alloys with solid solution phases," Nature Communications, 2015.

[11] GAO, M. C. et al. "High-entropy alloys fundamentals and applications," Springer, 2016.

[12] COURY, F. G. et al. "High Throughput Discovery and Design of Strong Multicomponent Metallic Solid Solutions," Scientific Reports, 2018.

[13] COURY, F. G. et al. "Multi-principal element alloys from the CrCoNi family: outlook and perspectives," Journal of Materials Research and Technology, 2021.

[14] YEH, J. W. et al. "High-Entropy Alloys – A New Era of Exploitation," Materials Science Forum, 2007.

[15] TRAMBLY, L. G. et al. "Electronic structure of complex Hume-Rothery phases and quasicrystals in transition metal aluminides," Prog Mater Sci, 2005.

[16] LI, Z. et al. "Metastablehigh-entropy dual-phase alloys overcome the strengtheductility trade-off," Nature, 2016.

[17] BIRBILIS, N. et al. "A perspective on corrosion of multi-principal element alloys," Materials Degradation, 2021.

[18] GLUDOVATZ, B. et al. "Exceptional damage-tolerance of a medium-entropy alloy CrCoNi at cryogenic temperatures," Nat Commun, 2016.

[19] BUTLER, T. M. et al. "Microstructures and Mechanical properties of CrNb, CrNbTi, and CrNbTaTi concentrated refractory alloys," Intermetallics, 2021.

[20] SENKOV, O. N. et al. "Microstructure and Properties of Aluminum-Containing Refractory High-Entropy Alloys," *Jom,* 2014.

[21] GORR, B. et al. "High temperature oxidation behavior of an equimolar refractory metal-based alloy 20Nb 20Mo 20Cr 20Ti 20Al with and without Si addition.," *Journal Of Alloys And Compounds,* 2016.

[22] ERDOGAN, A. et al. "Effect of Al and Ti on High-Temperature Oxidation Behavior of CoCrFeNi-Based High Entropy Alloys," *Jom,* 2019.

[23] YE, B. et al. "High-Temperature oxidation behavior of (Hf0.2Zr0.2Ta0.2Nb0.2Ti0.2)C High Entropy ceramic in air," *Joural of the American Ceramic Society,* 2019.

[24] WEN, L. H. et al. "Effect of aging temperature on microstructure and properties of AlCoCrCuFeNi high-entropy alloy," *Intermetallics,* 2009.

[25] BUTLER, T. M. et al. "High temperature oxidation behaviors of equimolar NbTiZrV and NbTiZrCr refractory complex concentrated alloys (RCCAs)," *Journal Of Alloys And Compounds,* 2017.

[26] CAO, Y. K. et al. "Effects of Al and Mo on high temperature oxidation behavior of refractory high entropy alloys," *Transactions Of Nonferrous Metals Society Of China,* 2019.

[27] CHENG, Z. et al. "Improvement of high temperature oxidation resistance of micro arc oxidation coated AlTiNbMo0.5Ta0.5Zr high entropy alloy," *Materials Letters,* 2020.

[28] LI, L. C. et al. "Enhanced oxidation resistance of MoTaTiCrAl high entropy alloys by removal of Al," *Science China Materials,* 2020.

[29] GENG, J. et al. "Oxidation of Nb–Si–Cr–Al in situ composites with Mo, Ti and Hf additions," *Materials Science And Engineering: A,* 2006.

[30] SHEIKH, S. "Accelerated oxidation in ductile refractory high-entropy alloys," *Intermetallics,* 2018.

[31] YOUNG, D. J. et al. "High Temperature Oxidation and Corrosion of Metals", Sl: Elsevier, 2008.

[32] BUTLER, T. M. et al. "Oxidation Behaviors of CrNb, CrNbTi and CrNbTaTi concentrated refractory alloys," *Intermetallics,* 2022.

[33] WELCH, N. J. et al. "High-temperature oxidation behavior of TaTiCr, Ta4Ti3Cr, Ta2TiCr, and Ta4TiCr3 concentrated refractory alloys," *Journal of Alloys and Compounds,* 2023.

[34] GLEESON, B. "Thermodynamics and Theory of External and Internal Oxidation of Alloys," *Shreir's Corrosion,* 2010.

[35] GEMELLI, E. "Corrosão de Materiais Metálicos e sua Caracterização", Rio de Janeiro: LTC, 2001.

[36] GESMUNDO, F and GLEESON, B. "Oxidation of Multicomponent Two-Phase Alloys," *Oxidation of Metals,* 1995.

[37] SMEGGIL, J. G. "An Examination of the Mechanisms Involved in the Oxidation of the Aligned Eutectic Alloy Ni3AI-Ni3Nb," *Oxidation of Metals,* 1975.

[38] MALLIA, L. V. and YOUNG, D. J. "Sulfidation Behavior of Austeno-Ferritic Steels," *Oxidation of Metals,* 1984.

[39] BARRETT, C. A. and LOWELL, C. E. "Resistance ot Ni-Cr-Al Alloys to Cyclic Oxidation at 1100 and 1200°C," *Oxidation of Metals,* 1977.

[40] CARRASCO, J. L. G. et al. "The Role of Microstructure on Oxidation of Ni-Cr-AI Base Alloys at 1023 and 1123 K in Air," *Oxidation of Metals,* 1990.

[41] ESPEVIK, S. et al. "Oxidation of Ternary Co-Cr-W Alloys," *Oxidation of Metals,* 1983.

[42] BELEN, N. et al. "Effects of aluminum on the oxidation of 25Cr-35Ni cast steels," *Oxidation of Metals,* 1984.

[43] STRINGER, J. "The Oxidation of Niobium Single Crystals," *Acta Materialia,* 1969.

[44] JIANG, H. et al. "Effect of Nb on the high temperature oxidation of Ti-(0-50 at.%)Al," Scripta Materialia, 2002.

[45] KOFSTAD, P. et al. "Investigation on the Oxidation Mechanism of Titanium," *Acta Chemica Scandinavica,* 1958.

[46] DAI, J. et al. "High temperature oxidation behavior and research status of modifications on improving high temperature oxidation resistance of titanium alloys and titanium aluminides: A review," *Journal of Alloys and Compounds,* 2016..

[47] DORCHEH, A. S. et al. "Factors affecting isothermal oxidation of pure chromium in air," *Corrosion Science,* 2018.

[48] LILLERUD, K. P. and KOFSTAD, P. "On High Temperature Oxidation of Chromium. I. Oxidation of Annealed, Thermally Etched Chromium at 800°-1100°C," *J. Electrochem. Soc.: Solid-State Science and Technology,* 1980.

[49] BUSCAIL, H. et al. "X-Ray Diffraction to study the Oxidation Mechanism of Chromium at Elevated Temperatures," *Materials Science Forum,* 2004.

[50] MITCHELL, D. F. "Analysis of oxygen isotope interfaces using negative molecular ion SIMS," *Journal of Vacuum Science & Technology A: Vacuum, Surfaces, and Films,* 1983..

[51] CAPLAN, D. and SPROULE, G. "Effect of oxide grain structure on the high-temperature oxidation of Cr," *Oxidation of Metals,* 1975.

[52] ECER, G. M. and MEIER, G. H. "The effect of Cr2O3 volatilization on the oxidation kinetics of a Ni Cr alloy," *Scripta Metallurgica,* 1973.

[53] CHYRKIN, A. "Oxidation-induced phase transformations and lifetime limits of chromia-forming nickel-base alloy 625." Germany, 2011.

[54] MALAFAIA, A. M. S. et al. "Isothermal oxidation of Inconel 625 superalloy at 800 and 1000 °C: Microstructure and oxide layer characterization," *Materials Characterization,* 2020.

[55] NOPE, D. L. G. et al. "Role of Elemental Segregation on the Oxidation Behavior of Additively Manufactured Alloy 625," *Journal of The Minerals, Metals & Materials Society,* 2022.

[56] DARKEN, L. S. "Diffusion of carbon in austenite with a discontinuity in composition," *Transactions of the American Institute of Mining and Metallurgical Engineers,* 1949.

[57] MROWEC, S. "Mechanism of high-temperature sulphide corrosion of metals and alloys," *Werkstoffe und Korrosion,* 1980.

[58] GLEESON, B. et al. "A Comprehensive Investigation of the Sulfidation," *Oxidation of Metals,* 1990.

[59] GLEESON, B. "Alloy Degradation Under Oxidizing–Sulfidizing Conditions," *Materials Research,* 2004.

[60] LAI, G. Y. "High-Temperature Corrosion and Materials Applications", ASM international, 2007.

[61] BIRKS, N. et al. "High-Temperature Oxidation of Metals", Cambridge, 2006.

[62] CHEN, M. F. et al. "High-Temperature Sulfidation Behavior," *Oxidation of Metals,* 1989.

[63] CLENDENEN, R. L. and DRICKAMER, H. G. "Lattice parameters of nine oxides and sulfides as a function of pressure," *The Journal of Chemical Physics,* 1966.

[64] SKELTON, J. M. et al. "Chemical and Lattice Stability of the Tin Sulfides," *The Journal of Physical Chemistry C,* 2017.

[65] MROWEC, S. and PRZYBYLSKI, K. "Transport Properties of Sulfide Scales and Sulfidation," *Oxidation of Metals,* 1985.

[66] STRAFFORD, K. N. and DATTA, P. K. "Design of sulphidation resistant alloys," *Materials Science and Technology,* 1989.

[67] GLEESON, B. et al. "Effect of Nb on the High-Temperature," *Oxidation of Metals,* 1988.

[68] WHITTLE, D. P. et al. "Effect of chromium content on the sulphidation behaviour of Co-Cr alloys in H2/H2S mixtures (Ps2 = 15 torr)," *Corrosion Science,* 1973.

[69] BIEGUM, T. et al. "High-temperature sulfide corrosion of cobalt-chromium alloys," *Oxidation of Metals,* 1978.

[70] DAVIN, A. et al. "Influence of alloying elements on the hot-corrosion resistance of Co-Cr alloys," *Werkstoffe und Korrosion,* 1971.

[71] GLEESON, B. et al. "The sulfidation behavior of Co-Mo alloys containing various ternary additions," *Oxidation of Metals,* 1990.

[72] RAIKAR, S. et al. "Sulfidation kinetics of titanium and Ti-6Al-4V with elemental sulfur," *Corrosion Engineering, Science and Technology,* 2023.

[73] DOUGLASS, D. L. et al. "The Corrosion of Some Superalloys in Contact with Coal Chars in Coal Gasifier Atmospheres," *Oxidation of Metals,* 1981.

[74] ELLIOT, P. "A practical guide to high-temperature," *Materials & Design,* 1991.

[75] GENTIL, V. "Corrosão", LTC, 2003.

[76] SCHELLERT, S. et al. "Oxidation mechanism of refractory high entropy alloys Ta-Mo-Cr-Ti-Al with varying Ta content," *Corrosion Science,* 2021.

[77] ADAMIAN, R. and ALMENDRA, A. E. "Físico-Química: uma aplicação aos materiais", Rio de Janeiro: COPPE/UFRJ, 2002.

[78] RAO, C. and PISHARODY, K. "Transition Metal Sulfides," *Progress in Solid-State Chemistry,* 1976.

[79] HAYNES 188, " Nominal Composition.," [Online]. Available: https://www.haynesintl.com/en/datasheet/haynes-188-alloy/#nominal-composition. [Accessed 18 April 2023].

[80] HAZZLEDINE, P. M. and PIROUZ, P. "Synchroshear transformation in Laves phases," *Scripta Met. Mater,* 1993.

[81] CHISHOLM, M. F. et al. "Dislocation in complex materials," *Science,* 2005.

[82] KIM, W. J. et al. "Structure characterization of Laves-phase MgZn2 precipitated in Mg-Zn-Y alloy," *Met. Mater. Int.,* 2010.

[83] STEIN, F. and LEINEWEBER, L. A. "Laves phases: a review of their functional and structural application and an improved fundamental understanding of stability and properties," *J. Mater. Sci.,* 2021.

[84] ZHU, J. H. et al. "A thermodynamic interpretation of the size-ratio limits for Laves phase formation," *Metall. Mater. Trans,* 1999.

[85] BACKMAN, L. and OPILA, E. "Thermodynamic assessment of the group IV, V and VI oxides for the design of oxidation resistant multi-principal component materials," *Journal of the European Ceramic Society,* 2019.

[86] WYATT, B. C. et al. "Ultra-high temperature ceramics," *Nature reviews materials,* 2023.

[87] DSHSHAN, E. L. et al. "The oxidation of cobalt-chromium-carbon alloys," *Cobalt,* 1974.

[88] WANG, G. et al. "An Extension of Wagner's Analysis of Competing Scale Formation," *Oxidation of Metals,* 1991

[89] DEODESHMUKH, V. P. et al. "Early-stage oxidation behavior of Co-rich high-temperature alloys," *Materials and Corrosion,* 2013.

[90] HERCHENROEDER, R. B. "Haynes Alloy No. "188 Aging Characteristics."," *International Symposium on Structural Stability in Superalloys,* 1968.

[91] CLENNY, J. T. and ROSA, C. J. "Oxidation Kinetics of Niobium in the Temperature Range of 873 to 1083 K," *Metallurgical Transactions A,* 1980.

[92] GRAHAM, H. C. and DAVIS, H. H. "Oxidation/Vaporization Kinetics of Cr2O3," *Journal of the American Ceramic Society,* 1971.

[93] KOFSTAD, P. and LILLERUD, K. P. "On High Temperature Oxidation of Chromium. II. Propertie of Cr2O3 and the Oxidation Mechanism of Chromium," *J. Electrochem. Soc.: Solid-State Science and Technology,* 1980.

[94] ROYER, L. et al. "On the Oxidation and Nitridation of Chromium at 1300°C," *Oxidation of Metals,* 2010.

[95] MROWEC, S. "The Problem of Sulfur in High-Temperature Corrosion," *Oxidation of Metals,* vol. 44, 1995.

[96] MITSUI, H. et al. "The sulfidation and oxidation behavior of sputter-deposited amorphous Al-Nb-Si alloys at high temperatures," *Corrosion Science,* vol. 39, 1997.

[97] FRIEND, R. H. and YOFFE, A. D. "Electronic properties of intercalation complexes of the transition metal dichalcogenides," *Advances in Physics,* 1987.

[98] CHEN, M. F. and DOUGLASS, D. L. "Effect of Some Ternary Additions on the Sulfidation of Ni-Mo Alloys," *Oxidation of Metals,* 1990.